Effects of Mg^{2+}, Ni^{2+} and Ca^{2+} on ATP binding kinetics of nicotinate nucleotide adenylyltransferase from *Klebsiella pneumoniae* and *Enterococcus faecium:* insights from empirical and computational studies

by

Ruan van Deventer

(1623683)

MSc thesis

Submitted in fulfilment of the requirements for the degree

Mater of Science in Biochemistry & Cell Biology

in

Molecular and Cell Biology

to the Faculty of Science, University of the Witwatersrand, Johannesburg, South Africa

Supervisor: Dr Ikechukwu A. Achilonu

2023

Declaration

I, Ruan van Deventer, am a student registered for the degree of Master of Science in Biochemistry and Cell biology in the academic year of 2023.

I hereby declare the following:

- I am aware that plagiarism (the use of someone else's work without their permission and/or without acknowledging the original source) is wrong.
- I confirm that the thesis submitted for assessment for the above degree is my own unaided work except where explicitly indicated otherwise and acknowledged.
- I have followed the required conventions in referencing the thoughts and ideas of others.
- I understand that the University of the Witwatersrand may take disciplinary action against me if there is a belief that this is not my own unaided work or that I have failed to acknowledge the source of the ideas or words in my writing.

Signature Ruan van Deventer day of 12 July 2023

Publication

Part of the results presented in this thesis have been published:

Jeje, O., Maake, R., van Deventer, R., Esau, V., Iwuchukwu, E.A., Meyer, V., Khoza, T., Achilonu, I., 2022. Effect of Divalent Metal Ion on the Structure, Stability and Function of Klebsiella pneumoniae Nicotinate-Nucleotide Adenylyltransferase: Empirical and Computational Studies. Int. J. Mol. Sci. 23, 116. https://doi.org/10.3390/ijms23010116. These results have been used with permission.

Abstract

NNAT is an attractive target for drug development due to its crucial role in NAD+ synthesis. However, its characterisation in ESKAPE species, such as *Klebsiella pneumoniae* and *Enterococcus faecium*, remains limited. This study aimed to elucidate the binding mechanism of ATP, a pivotal substrate, to these NNAT species, focusing on the role of divalent metal ion cofactors. *Kp*NNAT and *Ef*NNAT enzymes were overexpressed and purified, yielding approximately 2 mg/ml for both. Various techniques were employed to investigate their properties, including far-UV CD, extrinsic ANS fluorescence, stopped-flow kinetic analyses, and MD simulations. The results revealed that *Kp*NNAT could bind ATP independently of divalent metal ions, but catalytic activity required the presence of Mg^{2+}. The kinetic analysis showed k_a values of 5.99 $\mu M^{-1}.sec^{-1}$ without divalent metal ions and 5.72 $\mu M^{-1}.sec^{-1}$ in the presence of Mg^{2+}. The "pseudo"-specific activity values were 0.005 µmol/min/mg without divalent metal ions and 0.374 µmol/min/mg in the presence of Mg^{2+}. Conversely, recombinant *Ef*NNAT exhibited limited ATP association, and the reasons for this remain unclear. Overall, this study shed light on the structural dynamics and functional kinetics of ATP association in both NNAT species. The findings contribute to our understanding of this druggable target and provide insights into the inactivity of *Ef*NNAT, which warrants further investigation.

Acknowledgements

I would like to thank

My advisor Dr Ikechukwu A. Achilonu, for his guidance, patience, and encouragement throughout my post-graduate journey. Thank you for all the fantastic opportunities you have provided.

Dr Claire Friel, from the University of Nottingham, for providing me with training on stopped-flow and, in so doing, allowing me to train other members of the Protein Structure and Function Unit (PSFRU).

Professor Yasien Sayed and Dr Sylvia Fanucchi for their advice throughout the several presentations and encounters within the PSFFRU.

Reabetswe Maake, Olamide Jeje and Veruschka Essau, for your constant discussions, advice, and training throughout multiple points of this MSc.

Thanks to Taryn Adams, Aasiya Lakhi and my other friends within the PSFRU for your encouragement and advice throughout my entire post-graduate career.

The National Research Foundation of South Africa for providing the necessary funding.

The Post-graduate Merit Award for providing the necessary funding.

Table of Contents

List of abbreviations

AMR	Antimicrobial resistance
ADH	Alcohol dehydrogenase
AMP	Adenosine monophosphate
ANS	8-anilino-1-naphthalenesulfonic acid
ATP	Adenosine triphosphate
CD	Circular dichroism
ESKAPE	*Enterococcus faecium, Staphylococcus aureus, Klebsiella pneumonia, Acinetobacter baumannii, Pseudomonas aeruginosa,* and Enterobacter species
HAI	Hospital-acquired infections
hNNAT	Human nicotinate nucleotide adenylyltransferase
IFD	Induced-fit docking
IMAC	Immobilised metal ion affinity chromatography
IPTG	isopropyl β-d-1-thiogalactopyranoside
Mant	2'-(or-3')-*O*-(*N*-methylanthraniloyl)
MD simulations	Molecular dynamic simulations
NAD	Nicotinamide adeninedinucleotide
NaMN	Nicotinic acid mononucleotide
NAMPT	nicotinamide phosphoribosyltransferase
NMN	Nicotinamide mononucleotide
NNAT	Nicotinate nucleotide adenylyltransferase
NRMSD	Normalised Root-mean square deviation
ORF	Open reading frame
PBP	Penicillin binding protein
PBS	Phosphate buffered saline
RMSD	Root-mean square deviation
RMSF	Root-mean square fluctuation
SDS-PAGE	Sodium dodecyl-sulphate polyacrylamide gel electrophoresis
SSE	Secondary structural elements
SSI	Surgical site infection
UTI	Urinary tract infection

YT	Yeast extract tryptone

List of figures

List of tables

1. Chapter one
Introduction

1.1 Problem statement

Antimicrobial resistance (AMR) refers to the ability of bacteria to grow and spread in the presence of antimicrobial therapeutics, often displaying resistance to multiple antimicrobial classes (Magiorakos et al., 2012). The prevalence of AMR has increased due to the emergence and propagation of diverse resistance genes, which can be attributed to both appropriate and inappropriate use of antimicrobial therapeutic strategies (Sommer et al., 2017). This trend is especially alarming in hospital-acquired infections (HAI), as the prevalence of AMR pathogens in such infections is increasing. This rise in prevalence has led to more severe infections, increasing healthcare costs, morbidity, mortality, and hospital stay duration in developed and developing countries (Khan et al., 2017). Regrettably, the current therapeutic pipeline requires new antimicrobial agents, further complicating this situation (Sommer et al., 2017). Currently, most antibiotic treatments target common cellular structures and pathways, such as cell wall synthesis, the cell cycle, and protein and DNA synthesis. Unfortunately, these strategies have proven ineffective alone, with limited benefit observed from combining them (De Angelis et al., 2018; Han et al., 2006). Therefore, to address these conditions, research must investigate alternative therapeutic methods. This section will discuss the growing problem of AMR pathogens and explore a potential novel drug target.

HAIs, alternatively nosocomial infections, occur during a patient's stay in a healthcare facility. Invasive medical devices, such as catheters, ventilators, and prolonged contact with contaminated surfaces and individuals, often cause these infections (Khan et al., 2017). HAIs have increased in recent years and can result in prolonged hospital stays, long-term disabilities, socio-economic disturbances, and increased mortality rates (Khan et al., 2017; Podschun and Ullmann, 1998).

Multiple sources classify HAIs based on the route of infection, such as bloodstream infections, urinary tract infections (UTI), surgical site infections (SSI), and nosocomial pneumonia (Khan et al., 2017; Hunter, 2012; Owens and Stoessel, 2008). According to the World Health Organization (WHO), approximately 15% of hospitalised patients worldwide suffer from HAIs, with a neonatal death rate of around 75% in Sub-Saharan Africa (Khan et al., 2017;

Podschun and Ullmann, 1998). The increasing prevalence of AMR pathogens within HAIs has led the WHO to prioritise *Enterococcus faecium*, *Staphylococcus aureus*, *Klebsiella pneumonia*, *Acinetobacter baumannii*, *Pseudomonas aeruginosa*, and *Enterobacter species* (ESKAPE) as significant threats to human health (De Oliveira et al., 2020).

The classification of the ESKAPE pathogens aims to guide research to overcome the sudden need for more effective antimicrobial treatment strategies, as they account for most AMR-related HAIs. The resistance mechanisms are often complicated, with ESKAPE pathogens showing resistance to β-lactams, β-lactamase inhibitor combinations, lipopeptides, macrolides, oxazolidinones, fluoroquinolones, tetracyclines, and other classes of antimicrobials (De Oliveira et al., 2020). Among the ESKAPE pathogens, *K. pneumoniae* and *E. faecium* have become significant threats, with *K. pneumoniae* strains demonstrating resistance to more than 50% of third-generation cephalosporins and carbapenems and *E. faecium* being the leading cause of enterococcal infections, with the increasing prevalence of vancomycin-resistant strains being quite worrisome (De Oliveira et al., 2020; Nirwati et al., 2019; Arias and Murray, 2012; Podschun and Ullmann, 1998).

K. pneumoniae is a Gram-negative bacterium that commonly resides within mammal mucosa. It commonly causes hospital-acquired pneumonia, ventilator-associated pneumonia, UTI, SSI, septicemia, and bacteremia (Nirwati et al., 2019). *E. faecium*, on the other hand, is a Gram-positive, anaerobic bacterium and is one of the leading causes of HAIs, accounting for approximately 12% of HAIs in the ICU. *E. faecium* accounts for approximately 20% of enterococcal infections and is a common cause of UTIs, bacteremia, cellulitis, and infective endocarditis. *E. faecium* infections are particularly problematic owing to the increased incidence of vancomycin-resistant strains, which are associated with an increased mortality rate (Arias and Murray, 2012; Hidron et al., 2008).

The increasing prevalence of antibiotic-resistant infections demands a concerted effort to research and develop new treatments, such as the promising target of nicotinate nucleotide adenylyltransferase (NNAT). NNAT has emerged as a potential target for novel antimicrobial therapies, as it plays a crucial role in synthesising NAD^+, an essential coenzyme for cell survival. However, before clinical implementation can occur, more research is needed to understand the mechanism of action of this enzyme. By gaining a deeper understanding of

NNAT, we may be able to develop new and effective antimicrobial therapies to combat the growing threat of AMR.

1.2 Rationale and justification

It is paramount to investigate novel therapeutic strategies to address the pressing need for new antimicrobial agents and combat the rise of AMR ESKAPE pathogens (De Oliveira et al., 2020). The drug development workflow, divided into nonclinical and clinical research phases, plays a crucial role in this endeavour (McLean, 2015). Nonclinical research focuses on characterising the structure and binding mechanics of the druggable target and testing a range of drugs against it. The clinical phase investigates the determined drug's safety, dosage, and efficacy (McLean, 2015). It is important to note that the successful progression through this workflow heavily relies on a thorough understanding of the druggable target. Thus, developing a comprehensive understanding of the druggable target is essential for the successful development of new antimicrobial agents. Figure 1.1 illustrates the workflow of drug development.

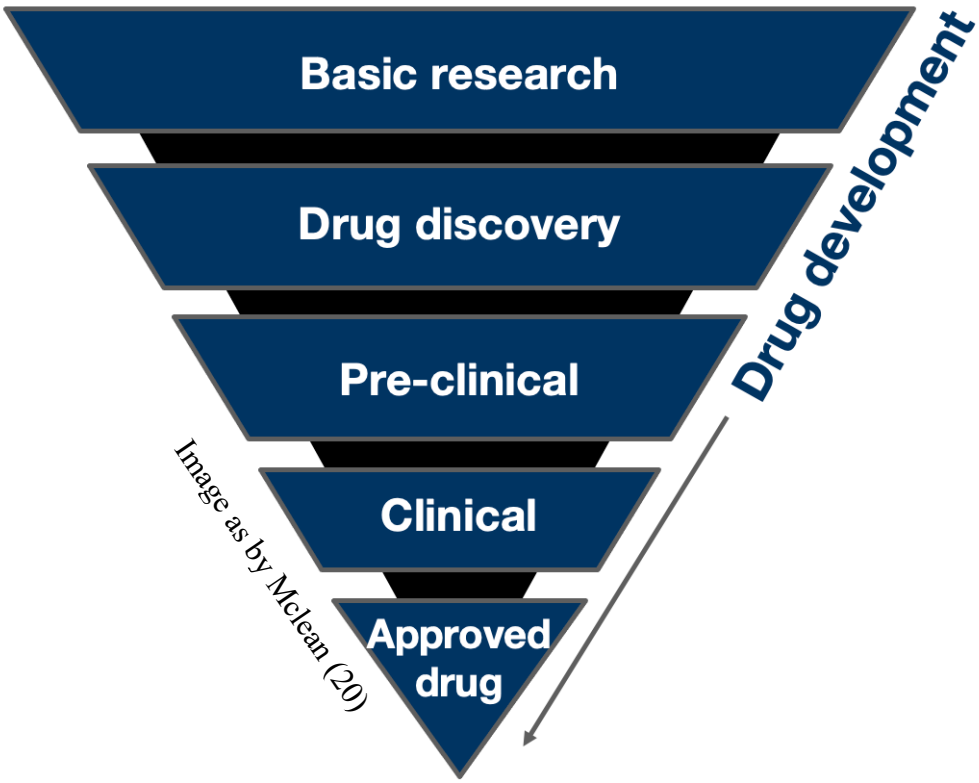

Figure 1.1 Drug development workflow. The reverse pyramid illustrates that each subsequent step is dependent on the former. The entire drug development workflow requires a thorough understanding of the potential drug target.

As illustrated in Figure 1.1, the drug development process depends on the basic research of the potential druggable target, emphasising the importance of a thorough understanding. NNAT species have been a topic of interest, as NNAT has been a potential druggable target for quite some time (Magni et al., 2004). The apparent variation in the pyridine nucleotide selectivity enables the isolation of a single NNAT species for therapeutically relevant targeting (Lau et al., 2009; Magni et al., 2004). This potential targeting has offered the ability to target an additional metabolic source within bacterial cells, which offers an alternative therapeutic approach compared to the existing strategies. In this regard, NNATs within the ESKAPE species are primarily uncharacterised and, despite their clinical potential, need more clinically relevant information available. Among these, *K. pneumoniae* NNAT (*Kp*NNAT) and *E. faecium* NNAT (*Ef*NNAT) are promising targets. These bacterial species are the leading issues within the ESKAPE classification, making research a potential boon. With this, the exact mechanisms of the reactions implemented by these NNAT species need to be clearly understood. Limited evidence exists regarding substrate selectivity, and we have a limited understanding of its dependence on divalent cations. As a note to the former, this lab has demonstrated that recombinant *Ef*NNAT is inactive, a potential consequence of alternative substrate selectivity or due to a preference for the alternate NAD^+ salvage pathway known as the PncA-PncB pathway. However, the exact reason for its inactivity is unclear, and due to its clinical importance, it is essential to understand the cause of this inactivity.

Given the clinical relevance of these NNAT species, it becomes essential to emphasise that any clinical implementation requires a thorough understanding of the systems in place, which will enable an improved scope of the biophysical and biochemical characteristics and mechanisms utilised by these NNAT species. Research is required, focusing on these NNAT species' structural dynamics and functional kinetics. Studying the substrate binding kinetics and structural dynamics of these NNAT species can serve as a foundation for downstream drug investigations, including discovering inhibitors and exploring functional modifications. This research can contribute to developing more effective and targeted drug therapies by providing insights into the complex structural changes required for substrate selectivity. This study aims to investigate the binding event relating to the association of adenosine triphosphate (ATP) to these NNAT species, more specifically, questioning the divalent metal ion co-factors' involvement. For this study, Mg^{2+}, Ca^{2+}, and Ni^{2+} were chosen to remain consistent with previously published literature (Daya et al., 2022; Jeje et al., 2022). To elaborate, Mg^{2+} and

Ca^{2+} are physiologically relevant divalent metal ions which are commonly involved within ATP association.

1.3. Aims and objectives

1.3.1 Aims

To study the influence of Mg^{2+}, Ca^{2+}, and Ni^{2+} on the association and disassociation rate constants of ATP which will define the impact of divalent metal ions on ATP binding kinetics.

1.3.2 Objectives

1.3.2.1 Overexpress *Kp*NNAT and *Ef*NNAT through recombinant protein expression in *Escherichia coli.*

1.3.2.2 Purify *Kp*NNAT and *Ef*NNAT through immobilised metal ion affinity chromatography (IMAC).

1.3.2.3 Confirm enzyme activity within *Kp*NNAT and *Ef*NNAT through a coupled-enzyme reaction.

1.3.2.4 Determine the composition of secondary structural elements (SSE) using far-UV circular dichroism (CD) spectroscopy.

1.3.2.5 Define the tertiary binding environment in relation to ATP using extrinsic 8-anilino-1-naphthalenesulfonic acid (ANS) fluorescence.

1.3.2.6 Determine the association rate constant and disassociation rate constant of Mant-ATP to *Kp*NNAT and *Ef*NNAT in the presence and absence of the divalent metal ions through stopped-flow kinetic analysis.

1.3.2.7 Generate structural models of *Kp*NNAT and *Ef*NNAT using Rosetta Fold.

1.3.2.8 Identify the structural elements involved within ATP binding in the presence and absence of the metal ions through *in silico* docking and molecular dynamic (MD) simulations.

1.4. Novelty

This study aims to introduce new strategies for the local research community and NNAT investigations. While the study has a significant computational component, empirical studies will be the largest contributor. Specifically, we will implement stopped-flow to characterise the kinetic parameters of these NNAT species. The primary focus is understanding ATP's binding event and its interaction with several metal ions. To achieve this, we will use stopped-flow to determine ATP's association and disassociation rate constants in both NNAT species.

Notably, to the best extent of our knowledge, this is the first instance of implementing stopped-flow related to these NNAT species. This approach will be combined with structural data to elaborate on the kinetic events. We will use a combination of far-UV CD and extrinsic ANS to define the structural dynamics of the ATP binding event. The results of this structural data have already been included in a publication (Jeje et al., 2022).

The above approach uses kinetic and structural evidence to characterise the ATP binding event. In the case of *Kp*NNAT, understanding one of the essential association events within the enzyme seems like a logical approach to identify potential therapeutic targets. However, for *Ef*NNAT, these analyses may uncover concerns regarding its inactivity. Unfortunately, the negative results regarding *Ef*NNAT's inactivity were not published, although the structure of the enzyme was characterised using similar techniques as mentioned earlier. These findings, as presented in later chapters, largely align with the current understanding of general NNAT enzymes. Given this structural agreement, it was hypothesised that the inactivity might be attributed to substrate preference. However, further investigation is required, specifically focusing on the functional kinetics and dynamics of ATP, to determine which substrate the inactivity could be attributed to without relying on expensive substrates.

Additionally, we will use MD simulations to improve our understanding of the binding event's structural dynamics and provide a more detailed explanation for the kinetic observations. In fact, Jeje *et al*. (2022) previously used MD simulations to study both NNAT species and provided a basic structural overview of the ATP binding event in the presence and absence of solvent-based/non-complexed divalent metal ions. While informative, this study has two primary limitations. Firstly, the models used are homology models, and secondly, they do not include complexed metal ions. These limitations limit our perspective on their direct binding influence, as there is no direct interaction between ATP and a metal ion. However, as per theoretical knowledge, ATP must be complexed with a metal ion to be an active biological compound (Yamanaka et al., 2016). Our study aims to build on the work of Jeje *et al.* (2022) by introducing the relevant divalent metal ions in the structure modelling stage, allowing us to observe their direct influence on the binding event. We will extend our simulations as per well-established practices. As to account for possible structural changes, simulations including divalent metal ions require longer times. Although no crystal structure is currently available for these NNAT species, recent advancements have enabled the public use of structural prediction algorithms such as AlphaFold2 and Rosetta Fold. Given the technique's novelty and

proven track record, we will use Rosetta Fold to predict the structure of both NNAT species and subvert the inaccuracies introduced by homology modelling.

1.5. Scope of the study

This study will combine a series of computational observations with empirically derived structural and kinetic data to provide a clearer picture of the ATP binding event. Both data types will supplement each other, with the computational simulations modelling the initial binding conformation and monitoring the structural fluctuations. This approach will define the primary interactions, including their strength and potential stabilising agents, assess the favorability of the interaction, and the structural chemistry involved in the ATP binding event in the presence and absence of relevant metal ions in a simulated environment. The computational data will complement the structural data obtained from far-UV CD and extrinsic ANS fluorescence, justifying why specific kinetic observations are plausible and enabling an understanding of the binding event's chemistry and whether the two concepts correlate. This combination of empirical and computational data addresses the biophysical and biochemical characteristics and mechanisms both NNAT species use to enable ATP binding, mainly how the divalent metal ions are involved in stabilising or facilitating the ATP binding event.

1.6. Structure of the dissertation

The thesis will comprise 7 chapters, each focusing on empirical and computational research. Chapter 1 will primarily focus on introducing the research concept, explaining its importance, and defining the problem statement. Chapter 2 will provide a theoretical background on HAIs, NNAT function and structure, and theoretical background to the techniques employed to facilitate the research. Chapter 3 will primarily focus on empirical investigations, demonstrating that *Kp*NNAT and *Ef*NNAT can be recombinantly overexpressed within *E. coli* cells and purified to homogeneity within a single Ni^{2+}-IMAC step as presented by Jeje *et al*., (2022). Subsequently, Chapter 4 will focus on the biophysical characterisation of the NNAT species through far-UV CD and extrinsic ANS fluorescence. These techniques help define the correct fold and relate the structural dynamics of ATP binding to the existing literature. Chapter 5 will discuss the kinetic data presented by stopped-flow, elaborating how it correlates with the structural dynamics observed in Chapters 4 and 6. Chapter 6 will primarily focus on computational modelling and MD simulations, validating the structural dynamics described in Chapter 4 and further relating this information to the various ATP binding modes and how this

influences ATP binding kinetics discussed in Chapter 6. The final chapter will provide an overarching discussion placing all the relevant information in context and offering the closing remarks. The references for the entirety of the thesis will follow the last chapter.

2. Chapter two
Literature review

2.1. Introduction

Given the urgency of therapeutical research, as previously suggested, novel therapeutic strategies need to be incurred and researched. However, these are only plausible after thoroughly understanding the potential druggable targets' structural dynamics and functional kinetics. Only then can enzyme modification and inhibition be considered. Thereby, NNAT has been subject to such research for quite some time, given its central role in NAD+ synthesis (Magni et al., 2004). Briefly, existing precursors can salvage NAD^+ or synthesise it *de novo*. Where NNAT is the link, both *de novo* synthesis and precursor salvage generate NNAT substrates, namely nicotinate mononucleotide (NMN) or nicotinic-acid mononucleotide (NaMN). NNAT utilises these substrates to produce NAD^+. NAD^+ is a commonly used energetic molecule involved in essential metabolic pathways, DNA repair and protein ADP-ribosylation, all being basic mechanisms required for cell survival (Magni et al., 2004; Begley et al., 2001; Ziegler and Oei, 2001; Petit and Ehrlich, 2000; Ziegler, 2000). Therefore, considering the apparent importance of NAD^+, its synthesis serves as a distinct and appealing druggable target, which is evident in the extensive characterisation of various NNAT species. This research, however, does not extend to the ESKAPE group, which is an unutilised resource. Given the information mentioned above, this chapter shall discuss the current issue of *K. pneumoniae* and *E. faecium* and the currently available information on *K. pneumoniae* NNAT (*Kp*NNAT) and *E. faecium* NNAT (*Ef*NNAT). This discussion will provide the necessary theoretical background to support the kinetic and structural characterisation of these NNAT species, as discussed in the subsequent chapters.

2.1.1. National statistics and resistance mechanisms within *K. pneumoniae and E. faecium*

In both instances, *K. pneumoniae* and *E. faecium* are recurring issues within the South African healthcare system. Both experience high infection rates, leading to frequent outbreaks and persistent issues (Zar et al., 2022; Alemayehu and Hailemariam, 2020; Essel et al., 2020). These strains hold significance as they commonly acquire resistance through the propagation of resistance-incurring genes within a population, which occurs due to the misuse of antibiotic treatments (Alemayehu and Hailemariam, 2020). Despite introducing new treatment combinations, medical professionals have not effectively combated the ever-increasing AMR

rise in *K. pneumoniae* and *E. faecium* (Jeje et al., 2022). Within both *K. pneumoniae* and *E. faecium*, multiple resistant strains are present; however, for *K. pneumoniae,* the β-lactam- and carbapenem-resistant strains and *E. faecium,* the vancomycin-resistant strains are the most problematic within South Africa (Zar et al., 2022; Alemayehu and Hailemariam, 2020; Essel et al., 2020). Briefly, as of 2018, reports indicate that *K. pneumoniae* exhibited a bloodstream infection incidence of 32% within neonates in Gauteng, along with a lower respiratory tract infection incidence of 15.5% as of 2021 (Zar et al., 2022; Essel et al., 2020). Among these, approximately 50 % account for strains resistant to carbapenems, cephalosporins and β-lactams (Jeje et al., 2022; De Oliveira et al., 2020). These conditions are exacerbated by the high incidence of HIV within the population, as it leads to an increased susceptibility to bacterial infections, thereby effectively increasing the incidence of AMR-based infections (Zar et al., 2022). Similarly, *E. faecium* is the most significant contributor to enterococcal infections, accounting for ~26.6 % of these infections within the African population (Alemayehu and Hailemariam, 2020; Arias and Murray, 2012), reflecting an alarmingly higher incidence of ~74.8 % within South African populations as of 2020 (Alemayehu and Hailemariam, 2020). This issue, unfortunately, is ongoing as an infection incidence of ~12 % has been reported since 2006 (Hidron et al., 2008). Vancomycin-resistant enterococcal (VRE) strains account for most of these reported cases. Though the rise in incidence in both cases can be attributed to the misuse of antibiotic treatments, as stated previously, this recurring issue is far more complex than this suggestion. The resistance mechanisms result from numerous combined factors, presenting a broad range of resistance to several antibiotic treatments and combinations.

In general, antibiotic resistance results from one or more resistance mechanisms contributing to a complex web that creates a resistant phenotype. Generally, resistance can be obtained by 1) the inactivation of the drug, preventing the action of the active component, 2) reducing the affinity of the binding site for the drug, thereby reducing the efficiency of drug binding, and 3) the downregulation of drug penetration that results from porin dysregulation and biofilm production (De Oliveira et al., 2020). *K. pneumoniae* and *E. faecium* use these strategies to generate and maintain AMR strains.

K. pneumoniae, for instance, utilises a combination of these resistance mechanism to reduce the efficiency and efficacy of most antibiotic classes, though more specifically carbapenems, cephalosporins and β-lactams. This resistance mechanism results from the overexpression of β-lactamases, narrow-spectrum Temoneira (TEM) type β-lactamases, extended-spectrum

lactamases and carbapenemases. Each hydrolyses the appropriate antibiotic, owing to its inactivation (McArthur et al., 2013; Gniadkowski, 2008). The modified penicillin-binding protein (PBP) known as PBP2a further extends this effect by reducing the binding affinity for β-lactams (Arias and Murray, 2012). Where this reduced affinity is enhanced by porin regulation, such as the modified LamB porin, for example, which has reduced affinity for β-lactams, limiting its transport through the cell wall and cell membrane, ultimately preventing its accumulation (Davin-Regli et al., 2019; Masi et al., 2019), all those mentioned above culminate in the ability of *K. pneumoniae* to produce biofilms an extra-cellular structure that enhances all the previous effects as well as enhancing horizontal-gene transfer allowing these resistance-incurring genes to be propagated throughout the population (Secor et al., 2018; Hall and Mah, 2017; Secor et al., 2015; Schembri et al., 2003). All these factors ultimately contribute to the resistance of β-lactams, β-lactamase inhibitor combinations, lipopeptides, macrolides, oxazolidinones, fluoroquinolones, and tetracyclines (De Oliveira et al., 2020). In a similar manner to the aforementioned, *E. faecium* exhibits several comparable attributes that contribute to resistance. These attributes encompass PBP5, a modified penicillin-binding protein that imparts high resistance to most ampicillin treatments, and aminoglycoside-modifying enzymes (AME) that decrease the binding affinity of aminoglycosides, thus contributing to vancomycin resistance (Arias and Murray, 2012; Zapun et al., 2008; Shaw et al., 1993). In this regard, ten resistance genes, namely *van*A-N, convey vancomycin resistance. These genes are predominantly acquired as it propagates through a population, encoding a reduced sensitivity within the cell wall, limiting the vancomycin binding (Foka et al., 2018).

There are a series of complex resistance mechanisms within both *K. pneumoniae* and *E. faecium,* each owing to the strains' resistance to a vast spectrum of antibiotic treatments. These resistance mechanisms have been observed in seriously alarming statistics throughout the African populations, with evidence suggesting that many currently available antibiotic treatments target highly defended cellular components. Thereby, alternative therapeutic strategies must be considered and researched. Due to its significance in cellular survival, researchers have extensively investigated the production of NAD^+ to identify potential targets for drug development.

2.1.2. NAD^+/NADH, its synthesis and why it is important

NAD^+ is a pivotal substrate and co-enzyme involved in several biochemical pathways critical for survival at a cellular level. Its importance can be alluded to by simply examining its complex mode of action, acting as a significant hydride acceptor for many redox reactions, with the overarching role to shuttle electrons between its reduced and oxidised state, thereby allowing it to function as a significant contributor to the energetic metabolism of the cell (Covarrubias et al., 2021). These reactions work within several capacities in the citric acid cycle, glycolysis, and fatty acid beta-oxidation. Though pivotal in the redox reactions of a cell, NAD^+/ NADH is involved in several non-redox reactions acting within DNA excision base repair, ADP-ribosylation as well as being a substrate to sirtuins and CD38/157 ectoenzymes (Magni et al., 2004; Begley et al., 2001; Ziegler and Oei, 2001; Petit and Ehrlich, 2000; Ziegler, 2000). Given its complex role within the cell, Figure 2.1 provides a simple illustration that may illuminate the action of NAD^+/ NADH within its large volume of tasks.

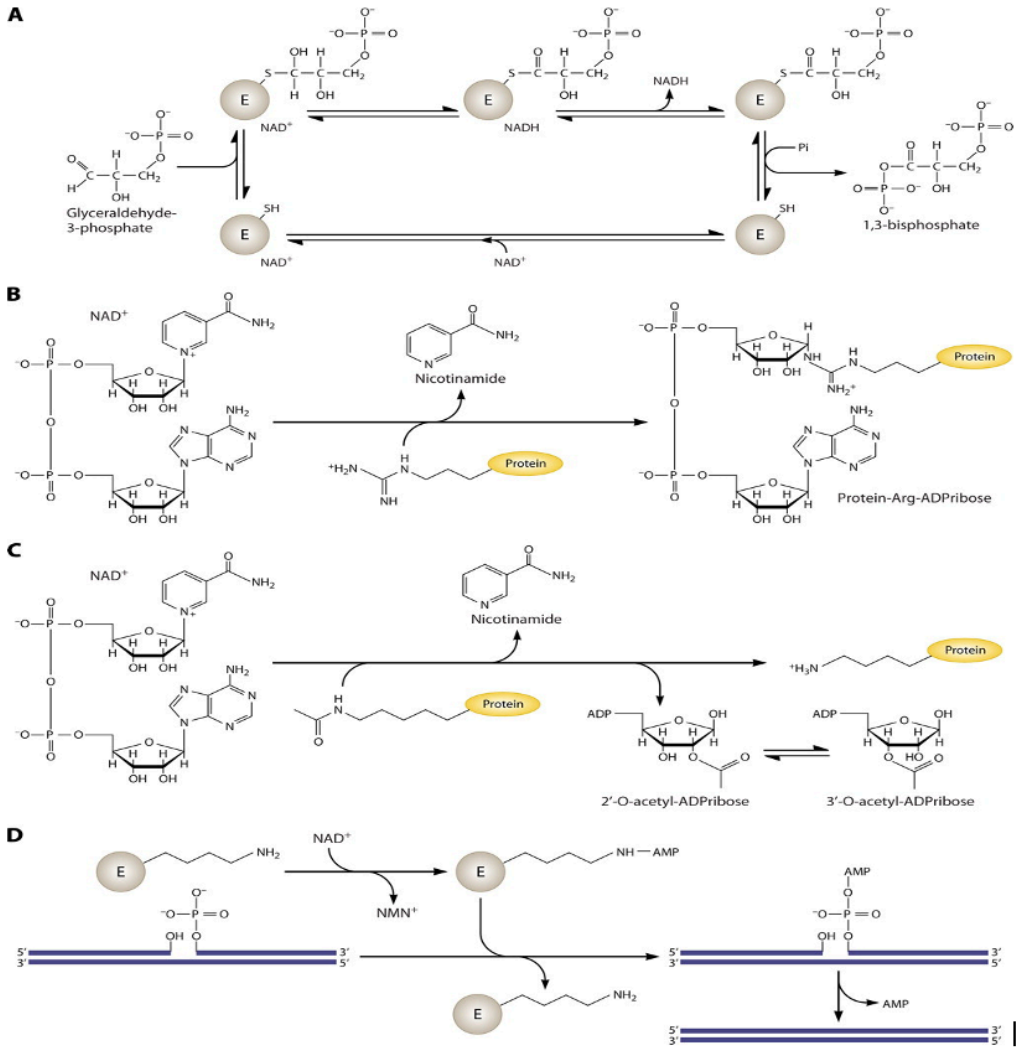

Figure 2.1 NAD^+/ NADH contributions to cellular survival as by Gazzaniga *et al.,* (2009). A) Demonstrates a step within glycolysis, depicting the conversion of glyceraldehyde-3-phosphate to 1,3-bisphosphate through the actions of NAD^+ dependent glyceraldehyde dehydrogenase. B) Denotes NAD^+ as the substrate for ADP-ribose transferase. C) NAD^+-dependent lysine deacetylation by sirtuins. D) NAD^+-dependent lysine adenylation by DNA ligase.

As presented in Figure 2.1, the mode of action of NAD^+ is incredibly diverse. Given these roles, the dysregulation of NAD^+ formation is linked to several disease states, including ageing, diabetes, atherosclerosis, retinal degeneration, and more (Covarrubias et al., 2021). Further implications arise from the possibility of targeting the production pathway of NAD^+ for therapeutic strategies against microbial infections and ageing. The NNAT enzymes have long been investigated as a potential druggable target for this production pathway as it is centrally routed in the synthesis of NAD^+ (Jeje et al., 2022; Magni et al., 2004). Briefly, the synthesis of NAD^+ occurs through two potential pathways: i) *de novo* synthesis and ii) a salvage pathway. The *de novo* synthesis of NAD^+ converts tryptophan to nicotinic acid mononucleotide (NaMN), a direct substrate for the NNAT enzyme (Covarrubias et al., 2021). The salvage pathway utilises nicotinamide, converting it to nicotinamide mononucleotide (NMN) using nicotinamide phosphoribosyltransferase (NAMPT). NNAT then conjugates either NaMN or NMN to ATP, forming nicotinic acid adenine dinucleotide (NaAD) or nicotinamide adenine dinucleotide (NAD^+), respectively (Magni et al., 2004). NaAD is later amidated to form NAD^+ by NAD^+ synthetase.

Given its central role within cellular mechanics, NAD^+ synthesis has been considered a target for therapeutic intervention. Though, the therapeutic potential of NNAT is still under investigation. As NNAT plays a central role in the synthesis of the energy carrier, converging the several mechanisms that form the precursors and substrates of the NAD^+ synthesis pathway. Fortunately, large volumes of information are available across multiple NNAT species, enabling the formulation of relatable theoretical models for the NNAT species of interest. Given the limited public information for *Kp*NNAT and *Ef*NNAT, this relation to theoretical models is paramount to visualising the potential occurrences within these NNAT species.

2.1.3. NNAT structure, catalytic function, and substrate binding

Across all NNAT species, there is significant sequence variation, yet despite this, there are still substantial structural similarities when considering the enzyme fold architecture (Magni et al., 2004). This similarity is primarily predominated through the highly conserved dinucleotide

binding domain, making up the core of the enzyme structure (D'Angelo et al., 2000; Saridakis et al., 2001). The NNAT core is described as a large hydrophobic cleft located within the centre of the enzyme, which makes up the two binding sites for NMN and ATP; they are closely positioned to one another to enable direct contact with each other (Lau et al., 2009; Magni et al., 2004). Given the summary above, this section shall introduce the known structural and mechanical functioning of the NNAT enzyme and its interaction with its substrates.

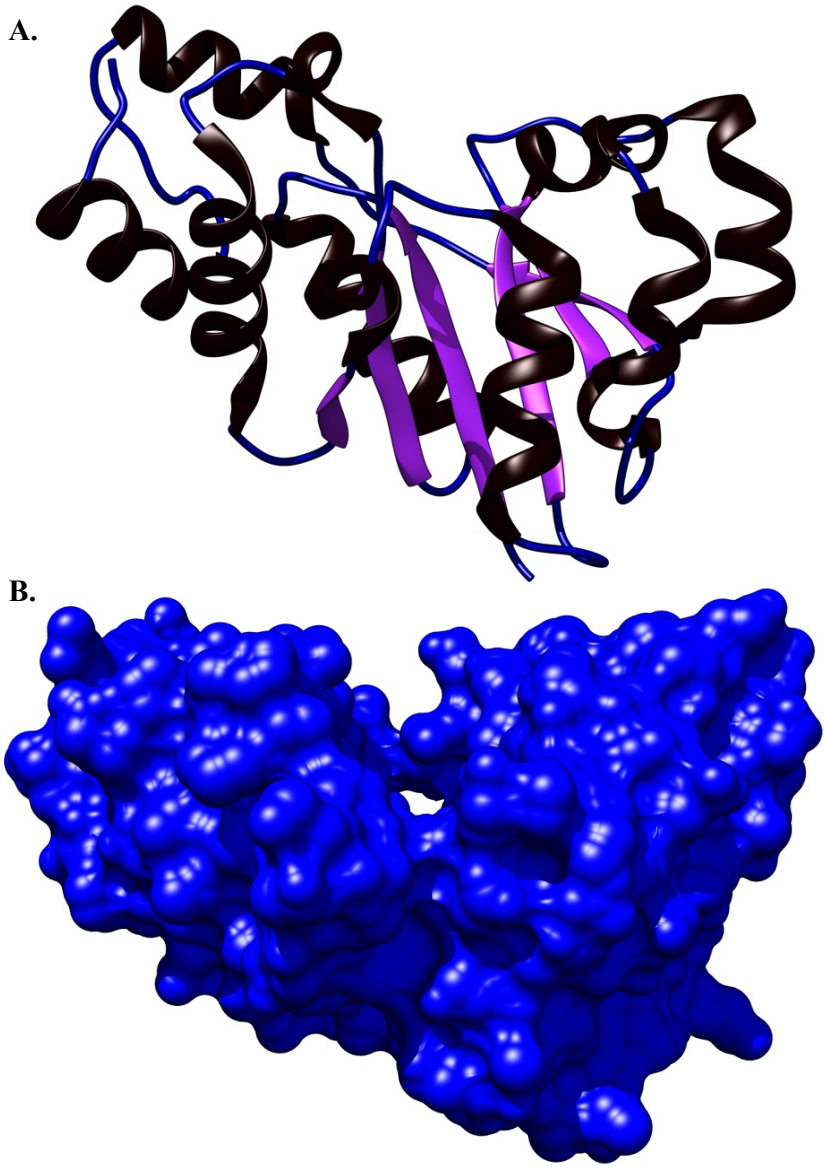

Figure 2.2 Surface and ribbon representation of *Pseudomonas aeruginosa* NNAT (PDB ID: 1YUN). A) depicts the ribbon structure of the enzyme displaying the beta-sheeted core (purple) and the flanking helices (black), and random coils (blue). B) Denotes the surface representation of *Pa*NNAT, displaying the central binding cleft.

Figure 2.2 displays the global architecture of the NNAT enzyme, depicting the largely alpha-helical and beta-sheeted makeup. This folding structure is highly conserved across all NNAT species as it defines the modified nucleotide-binding domain. The binding domain comprises a beta-sheeted core surrounded by alpha-helices (D'Angelo et al., 2000; Lau et al., 2009; Zhang et al., 2002). This structure's specific arrangement of alternating beta strands and alpha helices corresponds to a Rossmann fold. Of course, the number of helices and sheets formed varies among NNAT species, but the overall global folding architecture, as presented above, is retained. This fold enables the classification of the enzyme as a nucleotidyltransferase α/β phosphodiesterase (D'Angelo et al., 2000; Saridakis et al., 2001).

The structure of this enzyme core defines its binding capability to both the pyridine nucleotide (NMN/ NaMN) and ATP. Though this structure is shared mainly across all NNAT species, some species still have a direct preference for one of the pyridine nucleotides, with only a select few having no specific preference. These preferences are thought to originate from subtle architectural changes to the directly interacting residues, allowing alternate electrostatic distributions which would result in varying substrate stabilisation mechanics (Lau et al., 2009; Magni et al., 2004; Sorci et al., 2007; Zhang et al., 2002). Multiple NNAT species exhibit this variability, with the most notable distinction being the contrasting Gram status of the organisms. To elaborate, Gram-negative bacterial NNATs, such as *Kp*NNAT, are known to favour NMN as opposed to NaMN, and Gram-positive bacterial NNATs, such as *Ef*NNAT, are thought to favour NaMN as opposed to NMN (Jeje et al., 2022). It is important to note that this preference does not describe an inability to bind any potential pyridine nucleotide substrates; instead, it implies a greater reactivity towards one than the other.

Fortunately, such variability is not present within the ATP binding capability of the enzyme. This binding capability is primarily facilitated through highly conserved sequence motifs, such as a (H/T)XXH sequence at the N-terminal end of the enzyme (Magni et al., 2004; Saridakis et al., 2001; Sorci et al., 2007). This sequence is largely conserved across the enzyme class and is present within all NNAT species. For NNATs, this conserved region has been redefined as the (H/T)XGH conserved binding domain. The first histidine interacts with the β-phosphate and the second histidine interacts with the α-phosphate of the ATP substrate, and the glycine forms part of a secondary conserved binding motif referred to as the GXXXXG binding loop. This loop facilitates interaction with the leaving group, the pyrophosphate (Magni et al., 2004; Saridakis et al., 2001; Sorci et al., 2007). The (H/T)XGH binding motif is primarily involved

in the initial binding of the ATP substrate, facilitating the spatial coordination of the ATP molecule. The importance of this binding motif cannot be overstated, with previous literature displaying a complete reversal of ATP binding capability upon single-point mutations of the conserved sequence (Magni et al., 2004; Saridakis et al., 2001; Saridakis and Pai, 2003; Sorci et al., 2007). These observations define that this binding motif is incredibly sensitive to structural or mutational alterations. This binding motif acts in partnership with the highly conserved SXXXXR binding motif at the C-terminal end of the protein. However, no specific evidence suggests that this motif is involved in the direct hydrolysis of the ATP substrate. Instead, it assists in the spatial coordination of the substrate, thereby defining its global binding location within the enzyme core (Sershon et al., 2009). Here, the first serine residue forms a hydrogen bond with the main-chain nitrogen of the β-phosphate, and the arginine residue forms a salt bridge interaction with the γ-phosphate. Together these conserved binding motifs allow the initial spatial coordination of the ATP substrate assisting in the primary ATP binding event.

The initial ATP binding event is achieved and regulated through various factors defining protein-substrate contacts, ion stabilisations, and potential dimerisation (Sershon et al., 2009). The latter has an unknown impact on the binding event but is thought to contribute to intermediate stabilisation. In this regard, NNATs are prone to form homo-oligomeric structures defined by initial dimerisation, where the hexamer is composed of a trimer of dimers. Primarily dimerisation is driven through hydrophobic interactions between the monomeric subunits; these hydrophobic interactions assist in substrate stabilisation (Lau et al., 2009; Olland et al., 2002). Forming pseudo-twofold symmetries centred on a β-sheet upstream of the SXXXXR binding motif. For instance, *Bacillus subtilis* NNAT (*Bs*NNAT) dimerises through a hydrophobic interaction between Pro150 and a downstream hydrophobic residue. A further conserved interaction assists in dimerisation between the C-terminal loop and the 5th β-sheet (Olland et al., 2002). These interactions, including hydrophobic interactions and electrostatic conditions, are responsible for the dimerisation process and help to maintain the dimeric structure. This dimerisation enables a regulated response to the present substrates (Lau et al., 2009; Olland et al., 2002). In this regard, dimerisation enables a control mechanism whereby the initial association of an ATP molecule within a dimer reduces the binding capability of the alternative or second ATP binding site (Sershon et al., 2009). This control serves as a regulatory mechanism for the catalytic event. However, this system of regulation has only been reported within *Ba*NNAT. Little is understood as to the kinetic influence of dimerisation, though its role in substrate stabilisation and incorporation is clear. Like this, divalent metal ions are well-

known ATP stabilising co-factors that enable the ATP to be biologically active. Here, divalent metal ions stabilise the progressive charge development of the evolving intermediates in any ATPase-based interaction.

Briefly, NNAT hydrolyses ATP at the α-β phosphoanhydride bond, allowing the conjugation of an adenosine monophosphate (AMP) molecule to a pyridine nucleotide (Magni et al., 2004). This reaction is due to the combination of factors briefly discussed, such as protein-substrate contacts, ion stabilisations, and dimerisation, allowing the optimal positioning of the ATP substrate to favour nucleophilic attack of the 5'-phosphate of the pyridine nucleotide. Whereby the ester bond relating to the α-β phosphates becomes destabilised, displacing the pyridine nucleotide and ultimately forming NAD^+ or NaAD (Magni et al., 2004; Sershon et al., 2009; Sorci et al., 2007; Zhai et al., 2009; Zhang et al., 2002). This reaction schematic is represented in Figure 2.3.

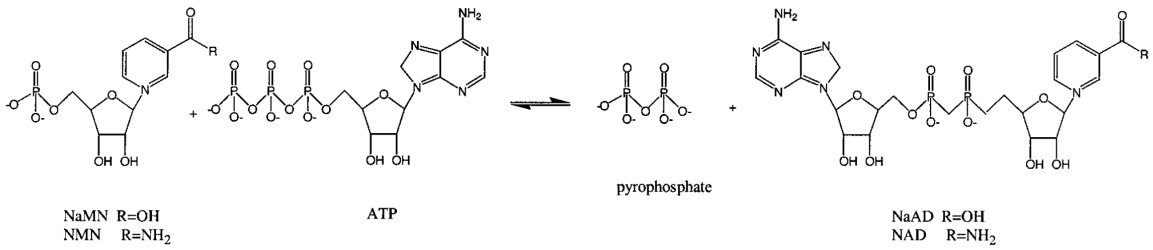

Figure 2.3 NAD/NaAD reaction mechanism as presented by Olland *et al.,* (2002). NNAT catalyses the reversible addition of NaMN or NMN to ATP yields NaAD or NAD^+, respectively.

The Figure above (Figure 2.3) depicts the bi-substrate reaction scheme of the general NNAT reaction. All known NNAT enzymes function on a sequential binding mechanism, with the binding order being variable and species-dependent (Magni et al., 2004). Human NNAT (hNNAT), for example, depicts ordered sequential binding mechanics. This interaction scheme is summarised below.

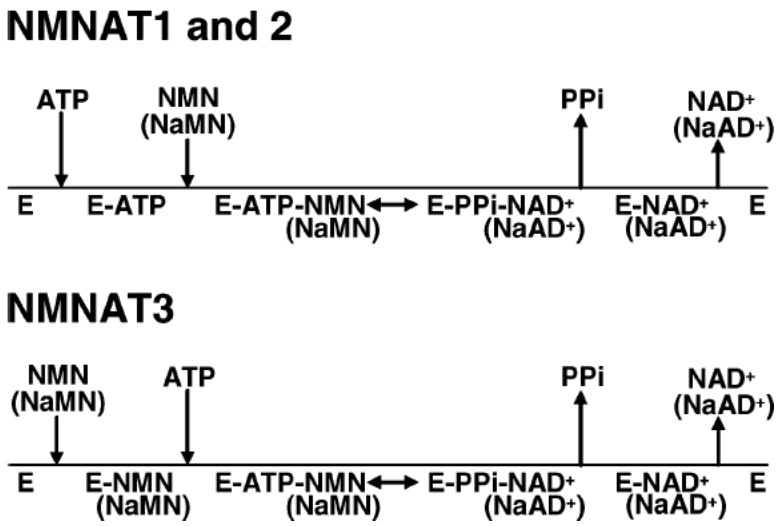

Figure 2.4 Steady-state kinetic mechanism of hNNAT as represented by Sorci *et al.,* (2007). The reaction architecture is described in Cleland's nomenclature.

Across all NNAT species, the inorganic pyrophosphate is released first (Figure 2.4). However, hNNAT-1 and hNNAT-2 initially bind ATP before the pyridine nucleotide, while hNNAT-3 demonstrates the reverse pattern (Figure 2.4). Similarly, multiple eukaryotic NNATs follow this reaction scheme, while archaeal NNATs exhibit a random order (Emanuelli et al., 1992; Natalini et al., 1986; Sorci et al., 2007). The purpose of this reaction order is two-fold, to i) correctly position the substrates and ii) to adapt the enzyme structure to allow close contact between the two substrates. This mechanism is beautifully illustrated within the random order mechanics of *Ba*NNAT (Sershon et al., 2009). Upon associating both substrates, the substrates are internalised into the core to facilitate direct contact. This structural change is enabled by i) the conformational adaptability of substrate association and ii) the stabilisation mechanisms for the evolving intermediates.

2.1.4. ATP binding mechanics, influenced by divalent metal ions

Regardless of the binding order of the ATP substrate, the enzyme immediately associates with it, followed by the formation of direct interactions with the present divalent metal ion. Literature suggests that this divalent metal ion would probably be Mg^{2+}, though alternative metal ions can be used. This ATP interaction is predominately facilitated and stabilised by three components i) directly interacting residues, ii) charge mitigation, and iii) coordinating water molecules. All these components allow the initial association event, followed by stabilising the newly formed complex and its evolving intermediates. As presented above, this section aims to provide an overview of the ATP association event and the involved stabilisation mechanics.

As previously discussed, the conserved binding motifs facilitate the initial association event, enabling direct contact with the ATP substrate and charge mitigation mechanics. These evolving mechanics enable the ATP substrate to bind within the upper binding cleft. The positive dipole established by the conserved SXXXXR binding motif drives the initial association, creating a strong positive electrostatic field. Upon its initial binding, ATP is shunted inward as a preliminary step to connect the substrate with the pyridine nucleotide. This phenomenon can be visualised by the crystalised *Sa*NNAT presented by Han, *et al.,* (2006).

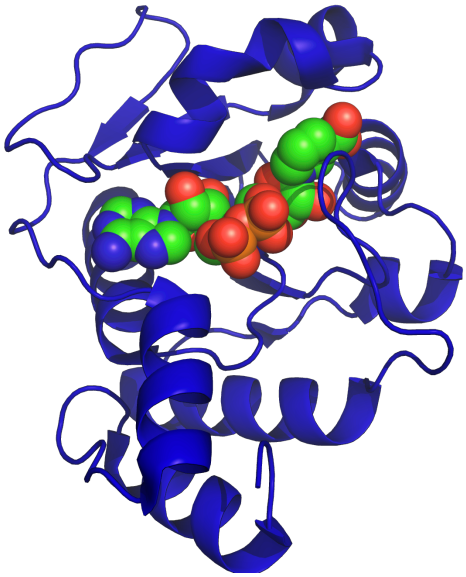

Figure 2.5 *Sa*NNAT complexed with NaAD as represented by Han *et al.,* (2006). A monomer of *Sa*NNAT is shown complexed with the NaAD product (spherical representation). The solvent-exposed diphosphate group is highlighted in red, emphasising the involvement of the solvent molecules for structural stabilisation.

Figure 2.5 displays the spatial association of the ATP substrate with the solvent-exposed diphosphate group. This Figure displays a single intermediate that requires stabilisation mechanics (Han et al., 2006). Whereby compiling several sources confirms that the positive dipole allows strong molecule retention. The surrounding water molecules enhance substrate retention by forming and coordinating hydrogen bonds. They facilitate the construction of a hydrogen bonding network that accommodates varying charged substrates, enabling electrostatic variability, which contributes to substrate selectivity (Han et al., 2006). In summary, several interactions ranging from direct amino acid interactions to optimisation of the local hydrogen bonding network facilitate the initial association of the ATP substrate with further contributions to complex stability. The latter, however, is a function primarily associated with the presented divalent metal ions.

When ATP binds to NNAT, it immediately interacts with the divalent metal ion, driving a highly bent conformation at the α-β phosphate bonds. Here, the most commonly favoured ion is Mg^{2+}, which is seen within most NNAT species (Sorci et al., 2007). With minimal evidence suggesting that Zn^{2+} may have a similar effect, though this has only been reported within hNNAT-1 (Sorci et al., 2007). Sorci *et al.,* (2007) showed that 20 mM Zn^{2+} achieves 95% activity compared to 20 mM Mg^{2+}, emphasising that hNNAT-1 can use Zn^{2+} as an alternative to Mg^{2+} with a minimal penalty to the percentage of activity. It further displayed no notable selective behaviour to either. Notably, Sorci *et al.,* (2007) tested multiple divalent metal ions, but only Zn^{2+} had sufficient reactivity compared to Mg^{2+}.

The extent to which the divalent ions are required is not fully understood, but D'Angelo *et al.,* (2000) postulated that the divalent ion might have two functions. Firstly, the divalent metal ion stabilises the pentavalent transition-state intermediate, adding to the already positive charge conveyed by the binding motifs discussed earlier. This structural involvement was evident as an Mg^{2+} ion is typically within ~3 Å from the α-phosphate of the ATP molecule. Secondly, D'Angelo *et al.,* (2000) postulated that the metal ion influences the electrophilic character of the α-phosphate, acting as a polariser, enabling the reaction to favour a nucleophilic attack. These postulates are in strong agreement with the previously established theory. The Mg^{2+} ions play a critical role in substrate and product stabilisation. As presented by Williams, who demonstrated that ATP binding is primarily stabilised by a positive binding pocket that results from the contribution of the Mg^{2+} ion, further stating that it is responsible for stabilising the increasing negative charge that results from hydrolysis, effectively stabilising the transition state (Williams, 2000). The findings from Williams are expanded upon by Frick *et al.,* (2007) who confirmed that the Mg^{2+} ion coordinates the ATP molecule and advances ATP hydrolysis by serving as a putative catalytic base (Frick et al., 2007).

Given those mentioned above, it becomes essential to understand the relationship between the Mg^{2+} ion and the inactivity of *Ef*NNAT. Further, given the potential significance of the NNAT enzyme, it is of paramount importance that a complete overview of its catalytic mechanism exists.

2.2. Methodological theory

Presently, both these NNAT species have been promising for drug target assessment, with a sudden bloom of available research greatly expanding our understanding of their underlying structural dynamics and functional kinetics. The above literature review illustrates these prospects currently in development. Chapter 1 highlighted this study's primary aim and subsequent objectives, defining the individual methodologies employed to investigate the aim. The following section will describe the theoretical background of the methodologies used to provide a greater understanding. This theoretical introduction aims to foster a greater understanding of the results presented in the later chapters.

2.2.1. Overexpression and purification of *Kp*NNAT and *Ef*NNAT

The fundamental cornerstone of protein biochemistry is the production of sufficient quantities of the target protein. Several techniques enable this, each with distinct advantages and limitations. These techniques include whole cell/tissue harvesting and recombinant expression across various hosts. The former produces native wild types, essentially the "original" copy, whereas the latter offers enzyme engineering and the mass production of these altered structures. Typically, whole cell/tissue harvesting is limited in the amount of protein produced, as it solely relies on the natural expression thereof. In comparison, recombinant expression enables the overexpression of the recombinant protein, often producing proteins within the low millimolar range.

In this regard, as will become apparent in later chapters, both *Kp*NNAT and *Ef*NNAT were recombinantly overexpressed within *E. coli* cells. This method is a well-established protocol that already describes the high purity and high yield obtainable through this technique with these enzyme species (Jeje et al., 2022). This technique offers controlled overexpression within *E. coli* cells with a high doubling rate. Briefly, this recombinant expression system is typically referred to as the T7-expression system. The T7-expression system, utilising the T7-RNA polymerase of the T7 bacteriophage, offers high specificity for its promoter sequences, allowing specific target gene overexpression. This overexpression, however, still occurs within a host *E. coli* cell with its native proteome present. Thereby, several purification steps may be required to isolate the target proteins. However, in this case, it is known that both *Kp*NNAT and *Ef*NNAT have efficient purifications with a single Ni^{2+}-IMAC steps, which uses a metal-ion coordination scheme to trap specific amino acids. This purification method is possible as

the recombinant *Kp*NNAT and *Ef*NNAT have engineered $(His)_6$-tags that significantly improve metal ion coordination to Ni^{2+}-IMAC.

Recombinant overexpression with the T7 expression system utilises the T7-RNA polymerase specific to the T7-promoter sequence. T7-RNA polymerase is employed explicitly due to its enhanced rate of RNA synthesis, less frequent termination events, and high specificity to its promoter sequence (Tabor, 2001). As implied by Figure 2.6, the typical annotation of expression strains follows the cell line, DE3 and pLysS or other relevant plasmids (should they be present). Among all, though, the DE3 confers the maintenance of the T7-RNA polymerase gene under the control of the lac operon, which is further inhibited or suppressed by a lac repressor (typically *lac I*). Upon the addition of an allolactose inhibitor, such as the non-hydrolysable allolactose isopropyl β-d-1-thiogalactopyranoside (IPTG), the structure of the lac repressor is altered, preventing its repressive capabilities (Gay et al., 2014; Studier and Moffatt, 1986; Tabor, 2001). This alteration is known as induction. A similar mechanism will be followed with the inclusion of the recombinant vector as it will also be under the control of a lac operon, and protein synthesis can continue only on the inhibition of the lac repressor. Alternative cell lines offer an additional pLysS vector, offering additional control over the basal level of expression (Gay et al., 2014; Qin et al., 2012; Studier and Moffatt, 1986; Tabor, 2001). Under all conditions and restrictions, these recombinant genes will undergo basal expression, which in some instances may exhibit cytotoxicity. Therefore, mitigating these "leaky" expressions to the greatest extent possible is crucial. Hence, the inclusion of the additional control through the pLysS plasmid, which expresses the T7 lysozyme, will inhibit the activity of the T7 RNA polymerase under uninduced conditions and ultimately helps minimise the leaky expression of the recombinant cell lines (Gay et al., 2014; Qin et al., 2012; Studier and Moffatt, 1986).

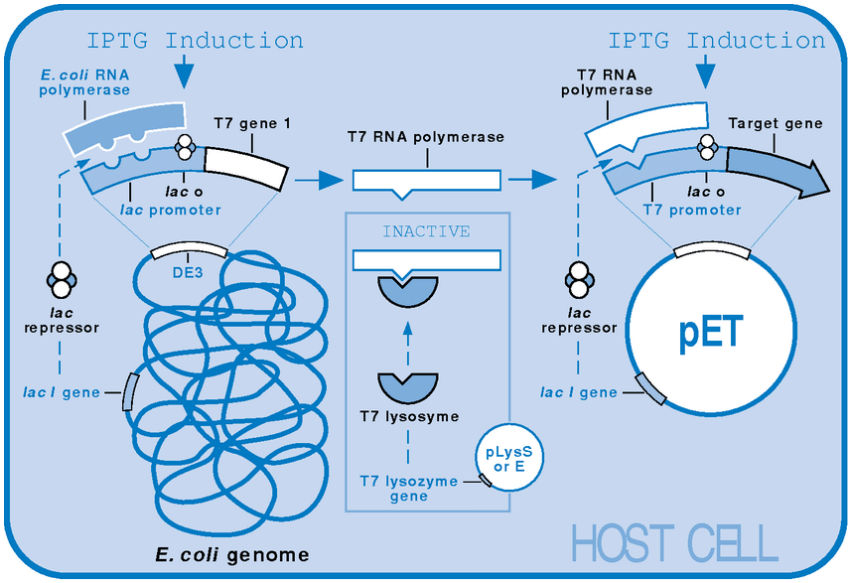

Figure 2.6 T7-expression system overview. Illustrating the generalised schematic presented within T7 expression systems. The figure illustrates the repression of the *lac o* sites through the *lac* repressor. The *lac* repressor prevents gene expression. By the inhibition of the *lac* repressor, gene expression will continue. Additionally, the figure illustrates the pLysS mechanism of action. Here pLysS expresses the T7 lysosyme which inactivates free floating T7 RNA polymerases, preventing basal expression.

Typically, after the recombinant overexpression of these proteins and even cell lysis, there remains a mixture of cellular debris and natively expressed proteins; for any further *in vitro* investigations, these "contaminants" need to be removed. Thereby, incorporating an affinity tag to the recombinant enzymes greatly improves purification quality and throughput as a single Ni^{2+}-IMAC step offers sufficient purification of recombinant-*Kp*NNAT and -*Ef*NNAT for downstream applications. In this regard, IMAC is a powerful purification strategy that has become the industry standard for the purification of recombinant proteins. It utilises the interaction between specific amino acids and transition metals such as Ni^{2+}, Co^{2+}, Cu^{2+}, and Zn^{2+}. Typically, Ni^{2+} offers the best balance between binding capacity and specificity, but should the latter need improvement, the other metal ions might offer a better alternative (Porath et al., 1975).

IMAC is a separation strategy that capitalises on the affinities between metal ions and proteins. This technique utilises covalently bound chelating compounds, which interact and coordinate the metal ions (Arnold, 1991; Gaberc-Porekar and Menart, 2001). The chelating compounds are attached to a solid chromatographic support matrix, serving as anchors for coordinating the metal ions on the matrix's surface. Commonly employed metal ions in IMAC include Ni^{2+}, Zn^{2+}, Co^{2+}, Cu^{2+}, and Fe^{2+} (Arnold, 1991; Gaberc-Porekar and Menart, 2001). Water or buffer molecules, such as imidazole, further facilitate coordination in this process. The interactions

between proteins and these metal ions result in retention, effectively replacing most interactions between the solid support matrix and water/buffer molecules. Specifically, the interactions occur between an electron donor on the protein surface and an electron acceptor, the metal ion (Arnold, 1991; Gaberc-Porekar and Menart, 2001).

The choice of different metal ions enables obtaining varying specificities and affinities. From the protein's perspective, specific functional groups in various amino acid residues can mediate these interactions leading to retention, such as Glu, Asp, Tyr, Cys, His, Arg, Lys, and Met. However, it is primarily the histidyl groups of histidine residues that predominantly contribute to retention. Consequently, the retention strength is primarily determined by the number of surface-accessible histidine residues. To enhance binding specificity, histidine affinity tags are engineered at the protein's N- or C-terminal ends (Arnold, 1991; Gaberc-Porekar and Menart, 2001). This combination allows for a specific interaction between the metal ions and the protein surface, rivalling other separation strategies that rely on "biospecific" affinities.

In summary, the combination of recombinant overexpression, utilising the T7 expression system, and the purification technique of Ni^{2+}-IMAC enables the production of high-quality and high-yield recombinant proteins for downstream applications. These methodologies pave the way for a comprehensive analysis of the structural and functional properties of *Kp*NNAT and *Ef*NNAT, contributing to a deeper understanding of their biological significance.

2.2.2. Structural characterisation through far-UV CD and extrinsic ANS fluorescence

Far-UV CD refers to the spectropolarimetric technique that measures the unequal absorption of right-and-left-handed circularly polarised light, which is a consequence of the asymmetric interaction between the chromophores, being the peptide bond, and the circularly polarised light (Greenfield, 2006). Briefly, circularly polarised light refers to the right-handed and left-handed sinusoidal waves, which generate vectors that trace circles in clockwise and counterclockwise directions (Greenfield, 2006). The asymmetrical chromophores, absorb these polarised waves in different quantities modifying the generated vectors to trace an ellipse, changing ellipticity. This quantifiable change in ellipticity is the measured quantity that creates the absorbance spectra (Woody, 1995). With the changing ellipticity, this technique allows the identification of the protein's global secondary structure as specific SSE such as α-helices, β-sheets and random coils present characteristic, unique and well-defined spectra (Woody 1995).

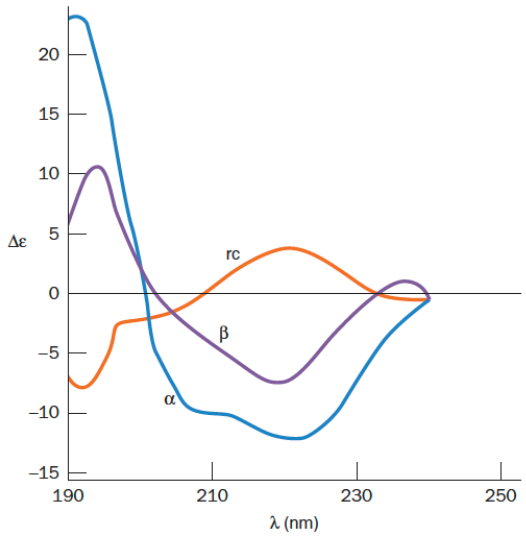

Figure 2.7 Far-UV CD spectra as presented by Greenfield (2006). α-helices (blue) are characterised as having troughs at 208 nm and 222nm with a positive peak at 193 nm. β-sheets (purple) are characterised by a large trough at 218 nm and a positive peak at 195 nm. Random coils are typically characterised by negative ellipticity at 200 nm.

This technique enables the identification of the global composition of these elements rather than defining the SSEs involved with specific amino acids. Far-UV CD uses small sample concentrations (usually not exceeding 5 μM) and is rapidly executed (Greenfield, 2006). Despite being unable to identify more specific structural information, this technique enables the rapid identification, characterisation, or confirmation of the global secondary structure. Though this technique provides global information, the characteristic spectra can be deconvolved using modelled data fitting tools such as the online server DichroWeb. Which compares the spectra of model proteins against the experimental spectra, assessing the percentage composition of the individual SSEs (Miles et al., 2022; Whitmore and Wallace, 2008, 2004). This deconvolution allows us to monitor and quantitate structural changes. These measurements and predictions should be carefully considered and typically rely on corroborating techniques. A readily employed technique used to define the tertiary structure of the proteins is extrinsic fluorescence using the ANS probe. Extrinsic ANS is a routinely used technique that is typically an appropriate corroborating technique for far-UV CD.

ANS, an anionic dye with a specific affinity for hydrophobic regions, is frequently employed as a probe to investigate the hydrophobic surfaces of proteins and potentially identify binding pockets (Engelhard and Evans, 1995; Gasymov and Glasgow, 2007; Semisotnov et al., 1991; Slavík, 1982). The fluorescent emissions from ANS are highly susceptible to the environment, to such an extent that when in free solution, ANS is excited at 390 nm and emits at 540 nm.

However, when the anionic dye is bound to the protein, the emission signal is blue-shifted with increased quantum yield (Engelhard and Evans, 1995; Gasymov and Glasgow, 2007; Kosower and Huppert, 1986; Kosower and Kanety, 1983; Semisotnov et al., 1991; Slavík, 1982). This phenomenon is a consequence of ion-pairing between a cationic amino acid, typically arginine or lysine, and the sulphonate group of the ANS, reducing the intermolecular charge transfer (CT) rate constant; this causes an increase in fluorescence as the intermolecular charge transfer correlates with the excitation of the ANS molecules (Gasymov and Glasgow, 2007). Using ANS as an extrinsic fluorescent tag is a highly sensitive technique commonly used to assess hydrophobic regions, protein folding, and potentially map ligand-binding locations. Similar to far-UV CD, this technique does not allow the characterisation of specific interacting residues; instead, it is only capable of providing a global perspective (Engelhard and Evans, 1995; Semisotnov et al., 1991; Slavík, 1982). With sample concentrations of 5 µM or lower, this technique requires minimal sample consumption while maintaining high accuracy (Engelhard and Evans, 1995; Semisotnov et al., 1991; Slavík, 1982). Further, this technique is readily employed in corroboration with other structural analyses, such as far-UV CD and has been applied within *Kp*NNAT (Daya et al., 2022; Jeje et al., 2022).

Far-UV CD and extrinsic fluorescence using the ANS probe offer complementary tools for studying protein structure and dynamics. With minimal sample consumption and high accuracy, these techniques can provide valuable information for characterising proteins' secondary structure and hydrophobic regions. Combined with other structural analyses, such as enzyme kinetic characterisation, they contribute to a more comprehensive understanding of protein structure-function relationships.

2.2.3. Enzyme assays and Stopped-flow Mant-ATP association studies

NNAT activity is, unfortunately, a more challenging aspect to quantify/parametrise, as its product NAD^+ does not have a distinguishable absorbance maximum. It absorbs light at 260 nm, but so does NADH; considering how easily NAD^+ becomes reduced, it becomes difficult to quantify the NAD^+ production directly.

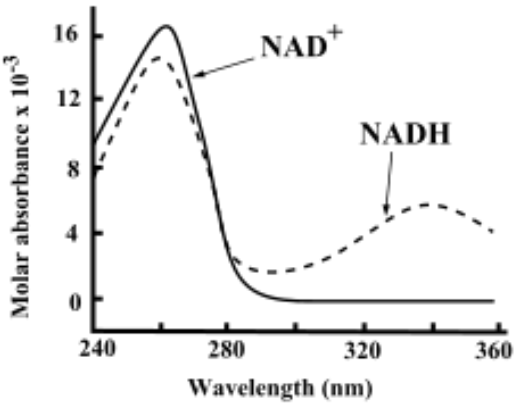

Figure 2.8 NAD^+ and NADH absorbance spectrums. Depicting the absorbance overlap with respect to NAD^+ (solid line) and NADH (dotted line) at 260 nm, with only NADH peaking at 340 nm (De Ruyck et al., 2007).

Thereby, the determination of NNAT activity has essentially become reliant on a coupled enzyme assay. The action of NNAT is coupled to that of alcohol dehydrogenase (ADH), which catalysis the reduction of NAD^+ to NADH using ethanol. The reaction mechanism is laid out below in Figure 2.9.

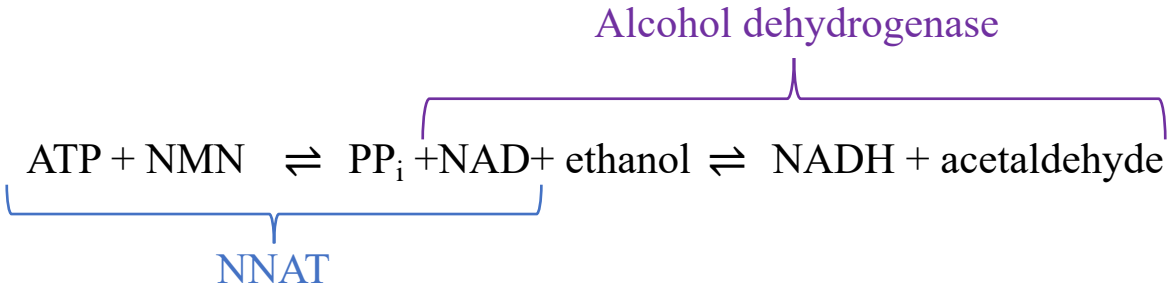

Figure 2.9 Coupled-enzyme reaction of NNAT and ADH. The chemical equation displays the reaction scheme of the coupled-enzyme reaction depicting how ADH uses the product of the NNAT reaction, NAD^+, to produce NADH and acetaldehyde. Where NADH is detectable at 260 nm and 340 nm (Figure 2.8).

In assessing NNAT activity (Figure 2.9), a coupled enzyme activity assay is employed, which provides "pseudo" kinetic parameters rather than directly measuring the activity of NNAT. To provide clarification, the term "pseudo"-kinetic parameters are linked explicitly to the coupled-enzyme mechanism. It is an in-house classification used to denote that the kinetic parameters obtained through this technique only indicate the true parameters. This nomenclature is primarily employed to maintain consistency with previously published literature by Daya, *et al*., (2022) and Jeje, *et al*., (2022). This limited parameterisation is an unfortunate side-effect

that can be mitigated, provided certain aspects are considered (Daya et al., 2022; Jeje et al., 2022).

Due to the nature of the coupled enzyme assay, the initial phase of the reaction has to be the rate-limiting step, as the rate-limiting step defines the true rate of the reaction. Thereby, the second phase (typically referred to as the indicator reaction) has to occur at a faster rate. Here, an extended lag phase can be anticipated, and a linear steady-state phase will only be reached once the conversion of intermediates becomes constant. The assay follows what Daya *et al.* (2022) and Jeje *et al.* (2022) presented with similar alterations in strategy.

With increasing NNAT concentrations and maintaining constant substrate concentrations, the "pseudo"-specific activity of both the NNAT species was determined in μmol/min/mg. These kinetic parameters will confirm NNAT activity post-expression and will be able to define the kinetic influence of the divalent metal ions. However, alternative techniques, such as a discontinuous reverse-phase HPLC assay and isothermal titration calorimetry (ITC), have been utilised more recently. In brief, for the current applications, a reverse-phase HPLC kinetic assay involving discontinuous NNAT reactions is impractical due to the large number of reactions required to obtain a sufficient kinetic overview. This technique relies on isolating and quantifying the products of the reaction through reverse-phase HPLC, which makes it time-consuming and impractical. Alternatively, isothermal titration calorimetry (ITC) can monitor the heat produced during the catalytic event, providing absolute accuracy. However, ITC itself is a laborious process, and considering the volume of experimental procedures planned, it is also impractical. Therefore, both these techniques are time-consuming and, considering the simplistic applications in mind, they become too tedious and laborious to apply in the current system.

Furthermore, to gain a deeper understanding of the reaction scheme, a rapid mixing technique known as stopped-flow is employed. Relative to experimental design, stopped-flow enables the isolation of individual reaction events enabling more specific monitoring capabilities such as ligand association/ disassociation, enzymatic turnover, and rate-limiting conformational changes, all on a millisecond time scale. Stopped-flow combines rapid mixing and an automated initiation system, making a large portion of the technique automated, allowing rapid response with mitigated error. Briefly, the stopped-flow can be described through the illustration presented below (Figure 2.10).

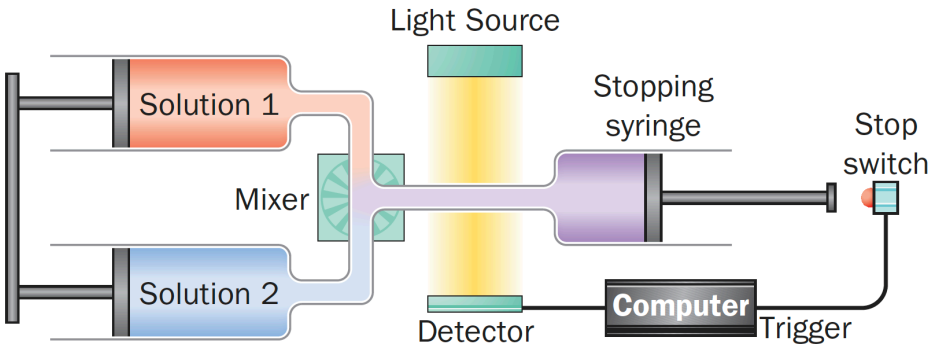

Figure 2.10 Stopped-flow workflow and operation as depicted by Johnson (1998). The whole reaction scheme is broken into two components and separated into solution 1 and solution 2. The two solutions are injected and rapidly mixed, with the mixed solution filling the stopping syringe. Once an appropriate volume is dispensed, the stop switch is triggered, signalling the detector to measure the event (Johnson, 1998).

Stopped-flow is a powerful technique that requires careful consideration of essential features and events during experimental design. The machine deadtime refers to the period from injection to the point when the detector is triggered without any monitored signal. It is crucial to account for the machine deadtime, mainly if the reaction event occurs faster than this duration, as it may result in signal loss. Stopped-flow offers versatility by allowing various detection options, such as far-UV CD, basic spectroscopy, fluorometry, and fluorescent polarisation. Understanding the technique's functionality is key to leveraging its value in experimental design. As stated previously, stopped-flow allows for the creative separation of a specific reaction enabling the isolation of a specific reaction event. For example, as depicted in Patel *et al.* (2014) characterised the ATP-turnover cycle of the protein known as MCAK using stopped-flow analysis. Using Mant-ATP, they performed a series of kinetic assays allowing the characterisation of the four stages as reflected in Figure 2.11.

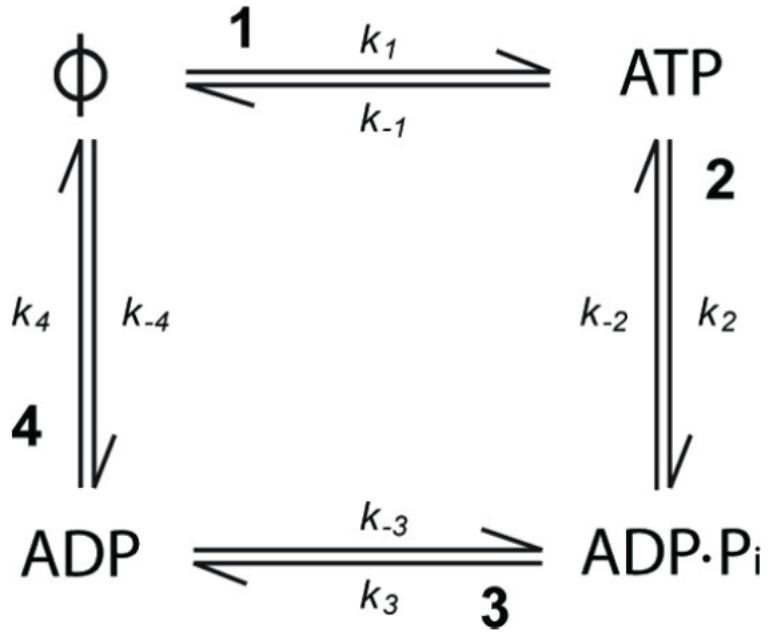

Figure 2.11 Theoretical enzymatic-based ATP turnover cycle. The Figure demonstrates the theoretical ATP-turnover cycle of most typical ATPases. The Φ is the apo-enzyme structure, followed by the progressive association/disassociation event with their respective rate constant (Friel et al., 2011).

Using Mant-labelled substrates such as Mant-ATP and Mant-ADP Patel *et al.* (2014) could characterise the association rate constant (k_{on}/ k_1/ k_2) and the dissociation rate constant (k_{off}/ k_{-1}/ k_{-2}), using stopped-flow. This characterisation was possible as the Mant label is a fluorescent label that increases in fluorescent yield when complexed with a protein structure. To apply focus, the first step, represented in Figure 2.11, the ATP association event to MCAK, was monitored by looking at the exponential rise in the fluorescent signal on the Mant-ATP association. These measurements resulted in a convoluted rate constant that defined both the direct association and disassociation event of Mant-ATP. Patel *et al.* (2014) subsequently used a linear deconvolution varying Mant-ATP concentration to deconvolve the rate constant into the respective rate constants, as depicted in Figure 2.11. Though this gives the rate constant of dissociation (k_{-1}), this does not provide the dissociation constant (k_d), which is the more commonly used equilibrium constant (Corzo, 2006).

Typically understood, the k_d is an equilibrium constant that defines the stability of the protein-ligand complex in kinetic parameters. The equilibrium constant of the protein-ligand complex takes into account the relative lifespan of the complex, which is determined by the rate constants: the rate constant of association (k_{on}/k_1) and the rate constant of disassociation (k_{off}/k_{-1}). Take the ligand association interaction as depicted below in Figure 2.12; ATP's association to the NNAT active site is described by the second-order rate constant k_1 in units of

concentration multiplied by a unit of time (commonly $M^{-1}.sec^{-1}$). The k_1 describes the rate of ligand binding and has an upper limit as ligand binding must be preceded by molecule collision (Corzo, 2006). ATP's disassociation from the NNAT active site is described by the first-order rate constant k_{-1} in a unit of time (commonly sec^{-1}). The k_{-1} is directly related to the lifetime of the ATP-NNAT complex. Therefore, the culmination of these rate constants describes the timeline of the ATP-NNAT complex from formation to decomposition, thereby describing the stability of the complex.

$$\mathbf{ATP + NNAT} \underset{k_{-1}}{\overset{k_1}{\rightleftharpoons}} \mathbf{ATP\text{-}NNAT}$$

Figure 2.12 ATP-NNAT complex formation. The figure above describes the formation of the ATP-NNAT complex in relation to its association rate constant (k_1) and disassociation rate constant (k_{-1}).

he equilibrium constant k_d defines the culmination of these rate constants as it equals k_1/k_{-1} and is represented in units of concentration (commonly M). This k_d is the more typical rate constant reported and used to justify complex stability (Corzo, 2006). Though helpful, it does not describe the reaction timeline as accurately as combining all these rate constants to describe the reaction events. These descriptors clearly define the reaction events even within reactions with similar k_d values. As previously discussed, stopped-flow was utilised to directly determine the association and dissociation rate constants of the ATP-NNAT complex and subsequently calculate the k_d. Additionally, using all three values to describe the reaction evolution under varying conditions; in the presence and absence of various divalent metal ions. These reaction descriptions were used to describe how the divalent metal ions influence the formation and decomposition of the ATP-NNAT complex, describing its reliance on the divalent metal ions.

2.2.4. Computational modelling

Regrettably, the lack of crystal structures for both *Kp*NNAT and *Ef*NNAT poses a significant limitation that has hindered further research in these species (Daya et al., 2022). As a protein biochemist, the lack of available crystal structures is a fundamental issue, as understanding protein function is intricately linked to its structure. In the absence of a crystal structure, researchers must rely on predicted or modelled protein models that utilise structural homologs to infer potential or probable structural conformations. The current industry standard is homology modelling, which uses structural comparisons between evolutionary homologs based on primary sequence to predict protein structure (Waterhouse et al., 2018). This

technique is highly dependent on sequence identity with loss of confidence with decreasing identity. In recent developments, the application of artificial intelligence to the protein folding problem has showcased remarkable potential (Baek et al., 2021). Ground-breaking modelling systems like Alpha Fold 2 and Rosetta Fold have emerged, sparking a revolution in the field. Unfortunately, at the time of this research, Alpha Fold 2 was not publicly available, and its predecessor fell short compared to the offerings of Rosetta Fold. Rosetta Fold balanced accuracy and computing power, providing the highest achievable accuracy while minimising the computational resources required (Baek et al., 2021).

In this regard, Rosetta Fold employs a three-fold neural network consisting of two primary neural networks working together alongside a constant third neural network. Fundamentally, these neural networks describe its ability to consider multiple sections of the protein folding hierarchy at once by i) describing the primary sequence in relation to similar sequences through multiple sequence alignments, ii) creating two-dimensional distance maps that are optimised through converging multiple conformations, and iii) considering the three-dimensional coordinate space (Baek et al., 2021). The third neural network defines the connection between the sequence, residue-residue distances and orientations, and atomic coordinates. The third neural network also constantly runs in parallel to the other neural networks, providing a constant consideration of the 3D coordinate space at all levels of predictions (Baek et al., 2021). All of which prioritise the initial development of the protein backbone using it as a skeletal model. This consideration of the third neural network offers a distinct advantage as it is the first software to incorporate it, and its closest competitor, Alpha Fold 2, considers the primary sequence and the distance maps (Baek et al., 2021). Thereby, Rosetta Fold offers an improved understanding of the sequence-structure relationships. This enabled Rosetta Fold to achieve great success within the critical assessment of protein structure prediction (CASP 14) competition of 2021, yielding an average of ~80 % prediction accuracy as tested against a series of blind protein structures (Baek et al., 2021). This success, as well as its three-fold neural network, are conveyed in Figure 2.13.

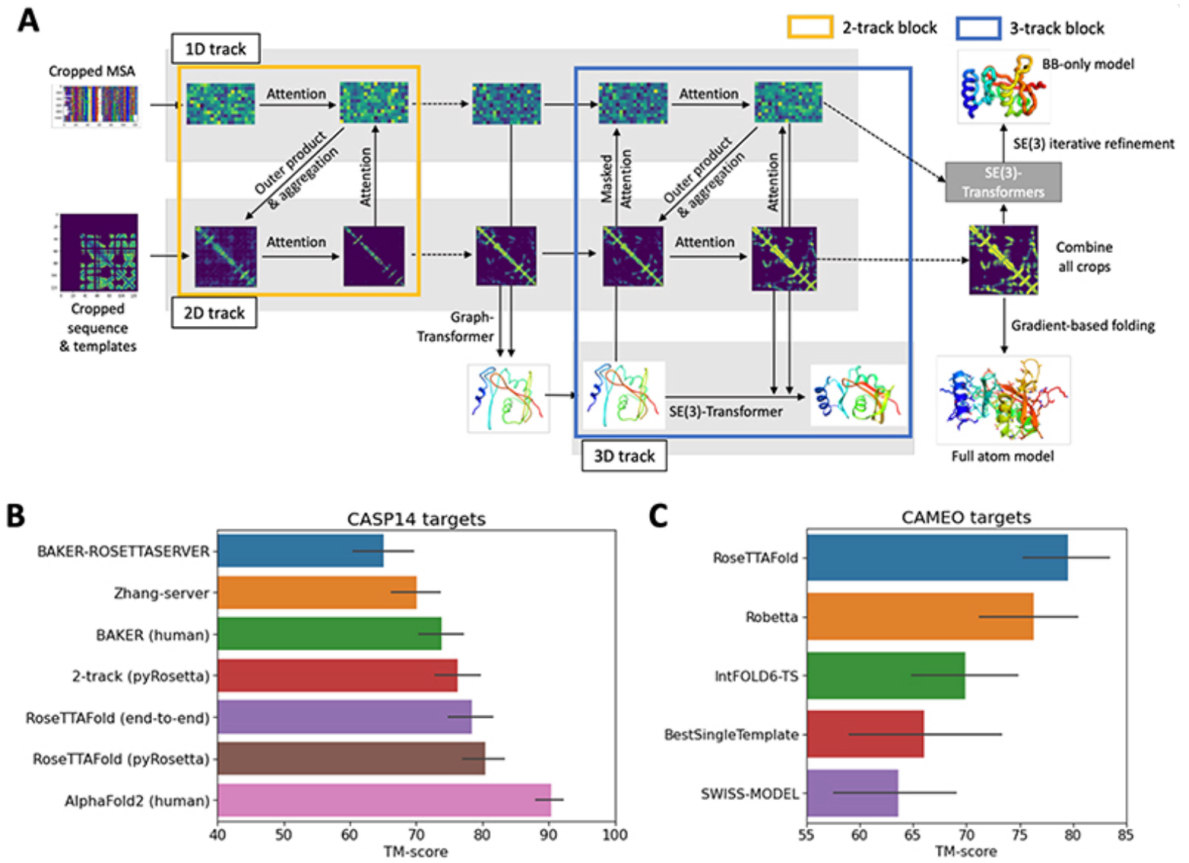

Figure 2.13 Rosetta Fold prediction algorithm and accuracy. A) Displays the three-fold neural network considered upon the protein structure prediction, displaying the 1D, 2D and 3D considerations. B) Displays the blind targets of the CASP-14 and their representative TM scores; the higher, the better. Here, AlphaFold 2 and Rosetta Fold were the top performing algorithms. C) Displaying the success rate of the individual programs submitted to CASP-14 (Baek et al., 2021). This panel displays the success of Rosetta Fold against alternative techniques such as the popular homology modelling tool Swiss-Model.

As seen in Figure 2.13, Rosetta Fold was among the best performers within CASP-14, displaying higher accuracies than the alternative techniques considered and previously used within these enzyme systems, *Kp*NNAT and *Ef*NNAT. Quite recently, a paper was released detailing similar computational methods for *Kp*NNAT, utilising Swiss-Model to define homology models (Jeje et al., 2022). However, given Rosetta Fold's recent successes, illustrating its accuracy, it certainly offers an alternative to this proposed method.

Rosetta Fold is a highly versatile software suite that combines *ab initio* modelling, fragment-based assembly, and other advanced algorithms to predict protein structures. Rosetta Fold excels in situations with limited or no known templates, making it useful for modelling novel protein folds and challenging protein structures (Baek et al., 2021). On the other hand, Swiss-Model leverages a template-based modelling approach, where it compares the target protein sequence to a database of experimentally determined protein structures (templates) and uses

this information to predict the structure of the target protein. SWISS-MODEL is particularly useful when a closely related template with a known structure is available, as it can provide accurate predictions in such cases. Unfortunately, the closest template structures available have an ~75 % sequence identity for *Kp*NNAT and ~47 % sequence identity for *Ef*NNAT. Though acceptable for *Kp*NNAT, it remains unadvisable for *Ef*NNAT. Therefore, an alternative technique is required to model both structures consistently. Given the success of Rosetta Fold, it was implemented as this alternative modelling tool, generating predicted structures of *Kp*NNAT and *Ef*NNAT. These structures were then docked with ATP using induced-fit docking (IFD) to create a functional model of the ATP binding event.

IFD is a tool within the Schrödinger Maestro v12.2 algorithm and uses a combination of the Glide and Prime algorithms to simulate specific molecular interactions. IFD exploits the induced fit model of protein-ligand interactions, which suggests this interaction is dynamic and corresponds with conformational changes within both side chain and main-chain residues to accommodate the ligand (Friesner et al., 2004). These considerations suggest that the interaction will shift to the lowest possible energy state to produce a low energy conformation. This method is facilitated through an exhaustive search of potential ligand and protein conformations through the Glide algorithm (Friesner et al., 2004). The resulting structures are docked within Glide and scored using Glidescore, which assesses Van der Waals energy, Coulomb energy, and H-bonds (Friesner et al., 2004). Prime predictions utilise the top-scoring complexes while excluding the most unfavourable complexes. The Prime algorithm predicts the side chain conformations surrounding the ligand (Friesner et al., 2004). Subsequently, energy minimisation is performed on the resulting complex. The final protein conformations obtained represent the induced-fit structure of the protein. The ligands are redocked using Glide and scored according to the Glidescore, binding energy and the IFD score (Friesner et al., 2004).

Typically docking protocols are merely implemented as the initial production of the input structures for later simulations. This requirement for later simulations is primarily due to the limited applicability drawn from a single static image. The resultant models are typically used in subsequent simulation systems such as Brownian dynamic simulations (BD), MD simulations and Molecular mechanic simulations (MM). These provide more thorough predictions, offering dynamic data and tracking molecular movement at varying levels. Though imperfect, MD simulations offer a powerful analytical tool enabling the visualisations of events

not necessarily seen within experimental techniques. The MD simulations are the most robust and industry-accepted tool available for this research and have been previously applied within *Kp*NNAT (Jeje et al., 2022). These simulations, however, did not display the involvement of the divalent metal ions as a directly interacting structure. Thus, employing the aforementioned preparation strategies enabled the creation of input structures that incorporate the divalent metal ions within the NNAT enzyme structures.

The simulations presented by Jeje *et al.* (2022) provide an excellent starting point for further investigation. Simulations involving the formation of metal centres and related structural features require extended time frames. Fortunately, technological advancements have made it considerably easier to accomplish this, as current simulation systems allow simulations within the microsecond time scale. Hence, this research is a natural extension of the MD simulations conducted in the previously published data (Jeje et al., 2022). To clearly understand the methodology behind MD simulations, Figure 2.14 provides a summarised depiction of the workflow of the standard MD simulation system.

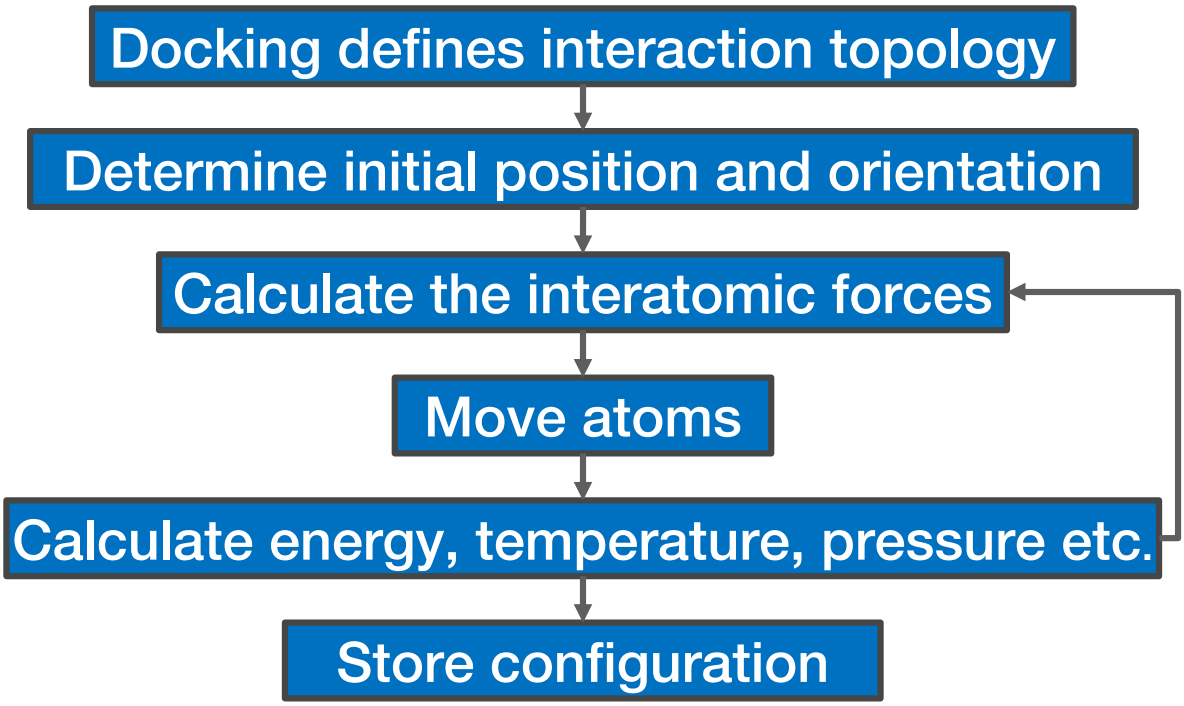

Figure 2.14 MD simulation workflow. Displays the development of MD simulations from input structure to the generation of a final conformation for a given frame. This process is repeated for multiple frames, ultimately generating a dynamic animation of the structural mobility with the target structures.

We will perform MD simulations using the Desmond tool within Schrödinger Maestro v12.2. MD simulations exploit the explicit solvent model (Bowers et al., 2006). The explicit solvent model considers the interacting waters on an atomistic level. This means that each water molecule is represented by its constituent atoms, typically oxygen and hydrogen atoms. Initially, a solvent box containing the water molecules and selected buffer molecules is generated. This solvent box represents the multidimensional simulation space and is typically described through crystal unit cell conventions (Bowers et al., 2006). Desmond determines the initial position and orientation of the docked molecules within the multidimensional simulation space (Figure 2.14). The simulation considers an atomistic view, simulating the motion and dynamics of the individual molecules. The interacting forces are calculated, and the direction and velocity of motion are determined based on Newton's laws of motion (Bowers et al., 2006). The molecules move according to the calculations, and the structure is subsequently minimised. The system's resulting energies, temperature, pressure, and volume are calculated, and the configuration is stored as a trajectory (Figure 2.14). These steps are repeated to fill the simulation time, each building on the previous step (Bowers et al., 2006). Due to the explicit solvent model, MD simulations require significant computational power. However, this downside is mitigated by highly dependable predictions.

3. Chapter three

Overexpression and purification of *Kp*NNAT and *Ef*NNAT

3.1. Introduction

For *in vitro* analysis of the relevant proteins, recombinant expression within a host cell is necessary. Briefly, the cDNA sequences that encode *Kp*NNAT (Uniprot: A6T6A0) and *Ef*NNAT (Uniprot: A0A133MWI0) were cloned into pET-28a(+) and pET-11a, respectively. To clarify, cDNA represents the complementary DNA sequence of mRNA, exclusively encompassing the coding sequences responsible for mRNA expression. Here, KpNNAT and *Ef*NNAT were cloned into different cloning vectors to facilitate clear distinction between them during overexpression procedures. These vectors can transform *Escherichia coli* cells, where the resultant recombinant *E. coli* are subject to the relevant expression system and high doubling rates (Twyman et al., 2003). This targeted expression and high doubling rates of the recombinant *E. coli* serve to "mass produce" the proteins within the cloning vector. As mentioned earlier, we used the T7-expression system in this study due to its ability to achieve high expression rates with minimal "leaky" expression. Specifically, the T7-express *E. coli* cell line, marketed as an enhanced BL21 derivative, offers high-efficiency transformation, phage resistance and deficiency in Lon and OmpT protease species. T7-express cells were transformed with the recombinant NNAT vectors, enabling their overexpression.

Overexpression is a consequence of the *lac* operon encoded within the bacterial cell line. Upon the transcription of this operon, it expresses T7 RNA polymerase in the presence of the non-hydrolysable allolactose mimic isopropyl β-d-1-thiogalactopyranoside (IPTG). The T7 RNA polymerase transcribes explicitly the gene sequences located downstream from the T7 promoter region, in this case being the respective NNAT vectors (Gay et al., 2014; Qin et al., 2012; Studier and Moffatt, 1986). This specific transcription enables the expression of recombinant proteins under the control of the T7 promoter. Fortunately, such tight control over the recombinant gene expression adds several advantages, such as limiting leaky expression, which minimises the metabolic load placed upon by the overexpression, avoiding potential toxicity. The utilisation of recombinant genes enables genetic engineering to optimise protein expression and further downstream applications, the most common of which include adding an affinity tag.

The cDNA of both NNAT species was engineered to contain a hexahistidine affinity tag, intending to utilise this for Ni^{2+}-IMAC purification. IMAC is a separation strategy that exploits the affinities between metal ions and proteins. The technique uses covalently bound chelating compounds attached to a solid chromatographic support matrix (Arnold, 1991; Gaberc-Porekar and Menart, 2001). The chelating compounds coordinate the metal ions on the surface of this chromatographic support, commonly involving metal ions such as Ni^{2+}, Zn^{2+}, Co^{2+}, Cu^{2+}, and Fe^{2+} (Arnold, 1991; Gaberc-Porekar and Menart, 2001). Water/buffer molecules, such as imidazole, facilitate further coordination. As previously stated, retention results from interactions between the proteins and these metal ions. These interactions replace most interactions between the solid support matrix and the water/buffer molecules. The interactions with the protein surface are between an electron donor on the protein surface and an electron acceptor, the metal ion (Arnold, 1991; Gaberc-Porekar and Menart, 2001).

Varying specificities and affinities can be obtained with the different metal ions chosen. From the protein's perspective, these interactions facilitate retention and can be mediated by specific functional groups of numerous amino acid residues: Glu, Asp, Tyr, Cys, His, Arg, Lys, and Met. However, retention is primarily a result of the histidyl groups of the histidine residues. Therefore, the number of surface-accessible histidine residues predominantly determines the retention strength. Histidine affinity tags are engineered onto a protein's N- or C-terminal end to increase binding specificity (Arnold, 1991; Gaberc-Porekar and Menart, 2001). This combination allows an interaction between the metal ions and the protein surface with a specificity that rivals similar separation strategies that employ "biospecific" affinities. With the information presented above, this section aims to report and discuss the recombinant overexpression and purification of both *Kp*NNAT and *Ef*NNAT.

3.2. Materials

Codon-optimised vectors of recombinant *Kp*NNAT (pET-28a(+)) and *Ef*NNAT (pET-11a) were procured from GenScript (GenScript, USA). A 5 mL HisTrap™ high performance chromatography column, NMN, ATP, ADH from *Saccharomyces cerevisiae* (Catalogue number: A7011), and DTT were purchased from Sigma-Aldrich (Merck Group, USA). PageRuler™ (10 to 250 kDa) protein ladder and Snakeskin™ dialysis tubing (10K MWCO, 22 mm) were acquired from Thermo Fisher (Thermo Fisher Scientific, USA). Other buffer components and reagents such as ethanol, sodium phosphate, sodium azide, Trizima base,

sodium acetate, and magnesium chloride ($MgCl_2$) were purchased from Sigma-Aldrich (Merck Group, USA) and were of analytical grade.

3.3. Methods

3.3.1. Vector design of KpNNAT and EfNNAT

The sequences of *Kp*NNAT and *Ef*NNAT were inserted into pET-28a(+) and pET-11a, respectively. Both sequences were engineered to include a hexahistidine affinity tag. For *Kp*NNAT, the $(his)_6$-tag was positioned at the C-terminus, accompanied by a downstream thrombin cleavage site that enables the subsequent removal of the $(his)_6$-tag. In the case of *Ef*NNAT, the $(his)_6$-tag was attached to the N-terminus to avoid potential interference with C-terminal dimerisation. However, the N-terminal $(his)_6$-tag for *Ef*NNAT did not have any adjacent cleavage sites, rendering it uncleavable. As presented in Figure 3.1, the gene of *Kp*NNAT was inserted in between the *NcoI* (C/CATGG) and the *BamHI* (G/GATCC) cleavage sites of pET-28a and the gene of *Ef*NNAT was inserted in between the *NdeI* (CA/TATG) and the *BamHI* (G/GATCC) site of pET-11a. The vectors further contained resistance genes, particularly resistance to ampicillin (pET-28a) and kanamycin (pET-11a). These resistances facilitate the selection of transformed cells, as discussed later.

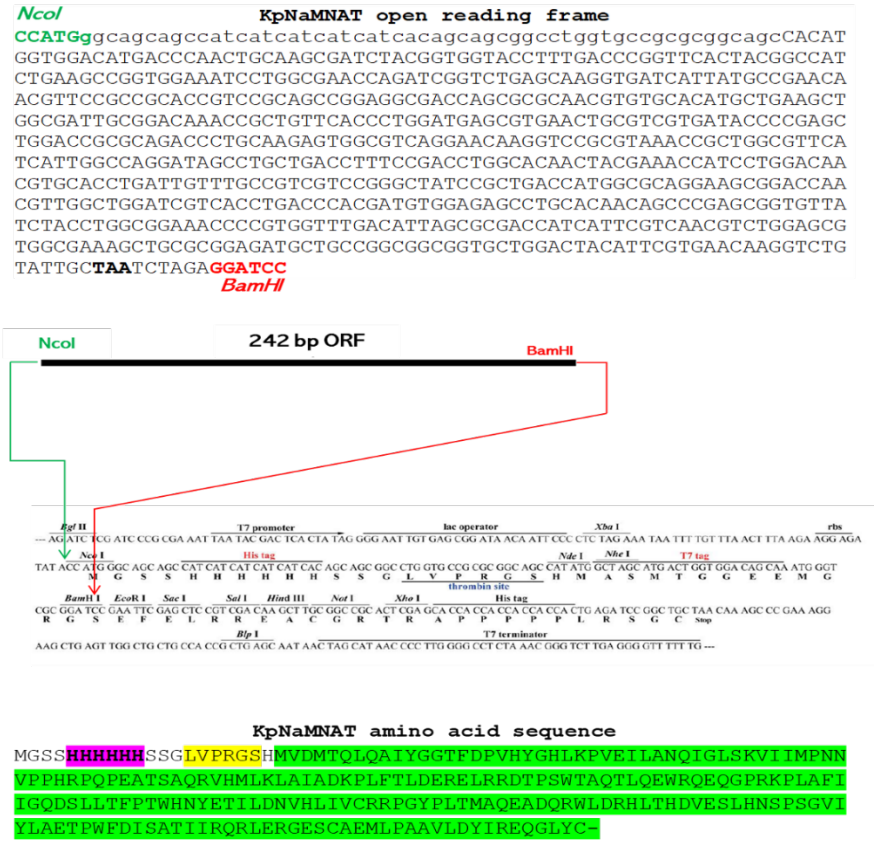

Figure 3.1 Vector design for recombinant overexpression of *Kp*NNAT**.** The gene's open reading frame (ORF) was inserted between the *NcoI* (C/CATGG) and the *BamHI* (G/GATCC) cleavage sites of pET-28a. The recombinant gene was engineered to contain a (His)6-tag and a thrombin cleavage site at the C-terminus.

The vector design utilised for *Kp*NNAT is illustrated in the above figure. These vectors were obtained from GenScript (GenScript, USA). As shown in Figure 3.1, the codon optimised vector featured a cleavable $(His)_6$-tag, which could be cleaved using a thrombin cleavage site. A similar vector design was employed for encoding *Ef*NNAT, as depicted in the Figure 3.2.

Figure 3.2 Vector design for recombinant overexpression of *Ef*NNAT**.** The gene's ORF was inserted between the *NdeI* (CA/TATG) and the *BamHI* (G/GATCC) cleavage sites of pET-11a. The recombinant gene was engineered to contain a (His)6-tag at the N-terminus.

The vector design utilised for *Ef*NNAT is illustrated in the above figure. These vectors were obtained from GenScript (GenScript, USA). As shown in Figure 3.2, the codon optimised vector featured an uncleavable $(His)_6$-tag.

3.3.2. Transformation of T7 express competent cells

The transformation was facilitated with T7-express competent cells, using heat shock as the transformation method. A mixture of ~100 ng of vector DNA and competent T-7 express *E. coli* cells were prepared and incubated at 4 °C for 30 minutes. This mixture was heat-shocked at 42 °C for precisely 45 seconds, followed by a 5-minute incubation at 4 °C. The transformed cells were added to SOC media (incubated at room temperature) and allowed to grow at 37 °C under agitation (250 rpm) for 1 hour. The cell broth was diluted, and a spread plate was prepared and incubated for 16 hours at 37 °C. The spread plate for the transformed cells containing the vector of *Kp*NNAT was supplemented with 35 µg/ml kanamycin and

chloramphenicol. In contrast, the spread plate for the transformed cells containing *Ef*NNAT was supplemented with 100 µg/ml of ampicillin and 35 µg/ml of chloramphenicol. Single colonies were selected, and overnight cell broths were prepared within 2x YT media (1.6 % (w/v) tryptone, 1 % (w/v) yeast extract, and 0.5 % (w/v) NaCl), supplemented with the respective antibiotics as previously stated.

3.3.3. Overexpression and lysate preparation of *Kp*NNAT and *Ef*NNAT

Using the previous overnight cell broth, a 1:10 dilution was prepared using fresh 2x YT media (1.6 % (w/v) tryptone, 1 % (w/v) yeast extract, and 0.5 % (w/v) NaCl). It was supplemented with 35 µg/ml of kanamycin for the expression of *Kp*NNAT and 100 µg/ml of ampicillin for the expression of *Ef*NNAT. Following inoculation with the respective recombinant cell lines, the broth grew to an OD_{600} of 4.6 AU at 37 °C under agitation (230 rpm). This OD_{600} signifies the optimum point to induce expression in a way that minimises cell death and maximises protein expression. Once at this OD_{600}, the cell broth was cold-shocked at 4 °C for 20 minutes, and expression was induced with 0.5 mM IPTG. The cell broth was overexpressed for 6 hours at 30 °C under agitation (230 rpm). The cells were harvested via centrifugation (4 °C, 5000×*g*, 5 min) and were resuspended in PBS buffer pH 7.2, supplemented with 75 mM imidazole, using 25 ml buffer for every 1 L of expression media. This mixture was frozen at -21 °C for storage and cell lysis. The cells were subsequently lysed using a combination of freeze-thawing and sonication (QSonica Q55 sonicator, QSonica sonicators, USA). Here, the samples were sonicated (at 10 amps) on ice for 1 minute, this was repeated 5 times. The sample was subjected to DNase activity for 30 min. The lysate was centrifugated (4 °C, 18000×*g*, 15 min) to separate the soluble and insoluble fractions. Each sample was collected for SDS-PAGE analysis, and the supernatant was collected.

3.3.4. IMAC purification and quantification of recombinant *Kp*NNAT and *Ef*NNAT

Both NNAT species followed the same IMAC purification protocol. Both proteins were purified on the AKTA start system (GE Healthcare AKTA start, GE HealthCare Technologies Inc., USA). Using a prepacked 5 ml His-trap column, the column was equilibrated with 10 column volumes (at 5 ml/min) of filtered PBS, pH 7.2 (supplemented with 0.02 % sodium azide and 75 mM imidazole). The inclusion of 75 mM imidazole is to shield the column from non-specific interactions, improving the overall quality of the purification. The cell lysate was filtered and loaded onto the column (at 2 ml/min). Following that, two consecutive 10-column

volume wash steps were performed at a 5 ml/min flow rate. The first wash step used filtered PBS, pH 7.2, containing 0.02% (w/v) sodium azide, 25 mM imidazole, and 2% (v/v) Tween 20. The second wash step used filtered PBS, pH 7.2, supplemented with 0.02% (w/v) sodium azide and 25 mM imidazole. The bound protein was eluted with filtered PBS, pH 7.2 (supplemented with 0.02 % (w/v) sodium azide and 500 mM imidazole). The protein peak was collected in 1 ml fractions where the fractions with the highest protein concentrations were pooled and dialysed, at 4 °C overnight, into PBS, pH 7.2, supplemented with 0.02 % (w/v) sodium azide and 1 mM DTT. Here, the samples were typically dialysed within 4 L of dialysis buffer, using the Snakeskin™ dialysis tubing (10K MWCO, 22 mm) acquired from Thermo Fisher (Thermo Fisher Scientific, USA).

3.3.5. Confirming *Kp*NNAT and *Ef*NNAT purity through SDS-PAGE

All SDS-PAGE runs were performed using a 12.5% gel. The samples were prepared by mixing them in a 1:1 ratio with a reducing sample buffer comprising 125 mM Tris-HCl, 20% (v/v) glycerol, 4% (w/v) SDS, 0.02% (w/v) bromophenol blue, and 5% (v/v) freshly added β-mercaptoethanol (pH 6.8). Following preparation, the samples were heated at 95 °C for 5 minutes. Electrophoresis was then carried out at 160 V for approximately 2 hours. After the electrophoresis, the gels were subjected to staining with a solution consisting of 2% (w/v) Coomassie Blue R250, 13.5% (v/v) glacial acetic acid, and 18.75% (v/v) ethanol for approximately 2 hours. Subsequently, the stained gels were destained overnight using 40% (v/v) ethanol and 10% (v/v) glacial acetic acid. During analysis, the samples were compared to the PageRuler™ protein ladder, and were deemed appropriate based on their alignment within the 25-27 kDa range. This range corresponded to the predicted molecular weights of these enzymes obtained from the online resource ProtParam.

3.3.6. Spectroscopic quantification of *Kp*NNAT and *Ef*NNAT

*Kp*NNAT and *Ef*NNAT were quantified using their ability to absorb light at 280 nm. Here a 1:10 serial dilution was prepared for each protein stock, and their absorbance was measured at 260 nm, 280 nm and 340 nm. The measurements were made on a Jasco V-730 UV-visible spectrophotometer (Jasco Inc, USA), using a 10 mm pathlength quartz cuvette. The measurement at 340 nm was used to account for protein/ sample precipitation. The samples were blank-corrected, and the 340 nm measurements were subtracted from the 280 nm. The

280 measurements were plotted against the dilution factor in Microsoft Excel (Microsoft Corporation, USA) to yield a linear plot in which the slope represented the corrected absorbance value. These corrected absorbances were used along with the extinction coefficients of *Kp*NNAT (38055 $M^{-1}.cm^{-1}$) and *Ef*NNAT (30370 $M^{-1}.cm^{-1}$) to calculate the final molar concentrations of the enzyme stock solutions. The analysis was performed in triplicate, and the displayed plots depict the averaged result. The difference between the replicates was encapsulated using error bars based on the data set's standard deviation of the means.

3.3.7. ADH coupled enzyme assay of NNAT species

The enzyme reaction scheme largely followed that as previously presented. NADH production was monitored at 340 nm as per the activity of alcohol ADH. The coupled enzyme assay was utilised to determine the "pseudo"-specific activity of the NNAT enzymes, thereby providing a quantifiable measure of whether they were active. The measurements were made on a Jasco V-730 UV-visible spectrophotometer (Jasco Inc, USA), using a 10 mm pathlength quartz cuvette. A dilution series of the protein, with a starting concentration of 1.6 µM, was prepared within the reaction buffer, being filtered 100 mM Tris-HCl, pH 9 supplemented with 1 % (v/v) ethanol, 1 mM ATP, 5 mM of the respective metal salts (i.e. MgCl2 and CaCl2) and 1 U/ml ADH stock. The reaction was initiated using 1 mM NMN and monitored for 1 minute, measuring the increasing signal at 340 nm. The raw data were processed and plotted using Microsoft Excel (Microsoft Corporation, USA), as only linear regressions were required for this data set. The absorbance was corrected to µmole (using the extinction coefficient: 6220 M-1.cm-1), which was plotted against the reaction time (minutes). Here, the linear regression slope represents the reaction rate in µmol/min for the respective protein concentrations. The individual protein concentrations' rates (µmol/min) were compiled and plotted against their respective enzyme mass in mg to yield a linear plot to which the linear regression slope represents the "pseudo"-specific activity of the enzyme in µmol/min/mg. The analysis was performed in triplicate, and the displayed plots depict the averaged result. The difference between the replicates was encapsulated using error bars based on the data set's standard deviation of the means.

3.4. Results

Both NNAT species were successfully purified within a single Ni^{2+} -IMAC step. The proteins were loaded onto the columns and eluted using 500 mM imidazole. Here, the high imidazole concentrations outcompeted the coordination between the immobilised metals and the $(His)_6$-tag. In both NNAT species, the chromatograms yielded 4 distinct phases, as represented in the Figure 3.3.

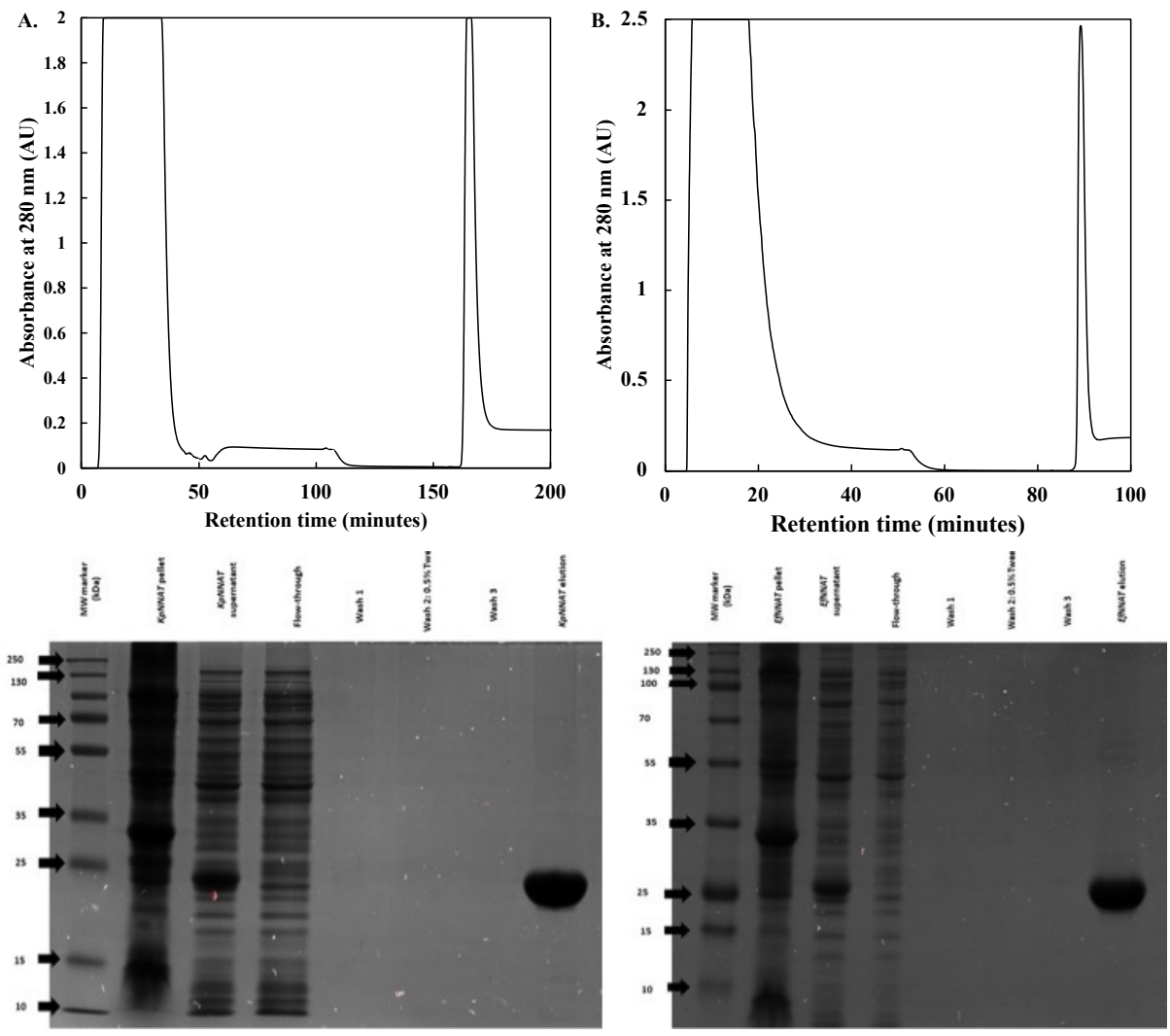

Figure 3.3 Purification of both NNAT species. The figure above denotes the IMAC purification chromatograms for *Kp*NNAT (A) and *Ef*NNAT (B) with their respective SDS-PAGE gels represented below the plot. In both chromatograms, four phases were apparent and consistently observed. From left to right, i) the flowthrough, non-binding/interacting protein species pass through the column. ii) The first wash with 2 % (v/v) 20 tween, with no apparent contaminant eluting. iii) The second wash with PBS and 25 mM imidazole, with no apparent contamination. iv) The NNAT elution peak was collected in 1 ml fractions and facilitated with 500 mM imidazole. Soluble protein was collected for both NNAT species and purified to a high yield sufficient for downstream application. In both SDS-PAGE gels, the

NNAT species were solely identified to approximately 25 kDa, further identifying the homogeneity of the protein stock solutions.

As depicted in Figure 3.3, there were four apparent phases to the purification step, i) the advent of the cell lysate yielding the flowthrough, ii) the initial detergent wash step containing 2 % Tween-20-PBS which removed remaining contaminants, iii) the second wash step to remove the contaminating detergent and iv) protein elution achieved with 500 mM imidazole. A single sample was taken at each phase for further analysis through SDS-PAGE. Both NNAT species were purified with a single Ni^{2+}-IMAC step. This purity can be visualised by the single bands of an approximate molecular weight of 25 kDa, placing it well within the predicted parameters, owing to 25 kDa for *Kp*NNAT and 24,8 kDa for *Ef*NNAT (Figure 3.3). Although no formal analysis was performed to determine the percent purity, based on the SDS-PAGE results, both NNAT enzymes were estimated to have been purified to over 95%. Upon confirmation of protein purity and dialysis into the storage buffer, the concentrations of the recombinant proteins were determined using a serial dilution, as displayed in the Figure 3.4.

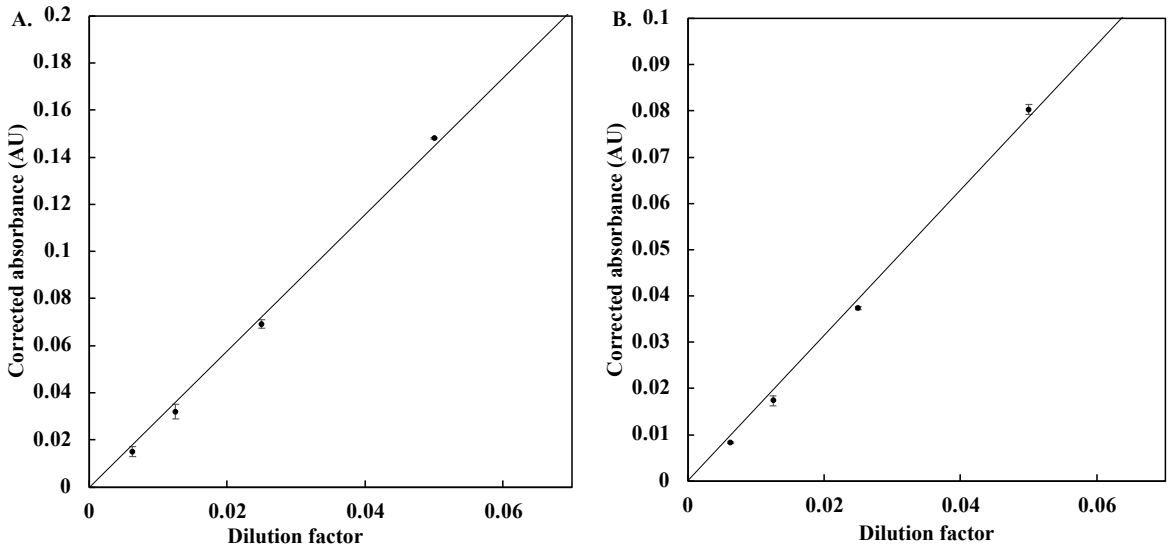

Figure 3.4 Concentration analysis of *Kp*NNAT and *Ef*NNAT. The linear plots represent the increasing absorbance at 280 nm with increasing *Kp*NNAT (A) and *Ef*NNAT (B) concentrations. *Kp*NNAT (A) yielded high sample volumes of high protein concentrations, calculated using the 2.9 slope against the predicted extinction coefficient (38055 $M^{-1}.cm^{-1}$). Owing to a 76.14 µM (~2 mg/ml) protein stock stored within PBS, pH7.2, supplemented with 1 mM DTT. *Ef*NNAT (B) yielded high sample volumes of high protein concentrations, calculated using the 1.6 slopes against the predicted extinction coefficient (30370 $M^{-1}.cm^{-1}$). Owing to a 51.75 µM (~2.6 mg/ml) protein stock stored within PBS, pH 7.2, supplemented with 1 mM DTT.

Figure 3.4 illustrated the high yield of purified recombinant NNAT proteins, demonstrating the success of the purification process. Here, *KpNNAT* expressed to 76.14 µM and *EfNNAT*

expressed to 51.75 µM. Both *Kp*NNAT and *Ef*NNAT were purified with a high yield, whereby both stock concentrations were ~ 2 mg/ml. Table 3.1 summarises the parameters discussed above.

Table 3.1 Relevant parameters expressed and used during *Kp*NNAT and *Ef*NNATs purification.

NNAT species	**Molecular weight (kDa)**	**Extinction coefficient ($M^{-1}.cm^{-1}$)**	**Corrected absorbance (AU)**	**Yield (mg/ml)**	**Estimated purity (%)**
***Kp*NNAT**	24.8	38055	2.9	1.9	> 95
***Ef*NNAT**	24.9	30370	1.6	2.6	> 95

Table 3.1 describes the molecular weight (kDa), extinction coefficient ($M^{-1}.cm^{-1}$), corrected absorbance (AU), protein yield (mg/ml), and the estimated purity of *Kp*NNAT and *Ef*NNAT. The molecular weights and extinction coefficients are used to calculate the protein yield. These calculations use the corrected absorbances which were extrapolated from the slopes of Figure 3.4. The yield expresses the final protein concentration within the purified stock solution. The estimated purity represents the estimated total percent of *Kp*NNAT and *Ef*NNAT within the purified stock solutions.

Table 3.1 summarised that both *Kp*NNAT (final yield of 1.9 mg/ml) and *Ef*NNAT (final yield of 2.6 mg/ml) were successfully purified to an estimated greater than 95 %. Here, it is important to note that the estimated purity (Table 3.1) purely depicts visual ques from Figure 3.3 and does not represent any quantitative measure. Therefore, to further ensure enzyme identity, additional measures were taken. Here, using the ADH-coupled enzyme assay, we confirmed the functionality of *Kp*NNAT, yielding sufficient NADH formation to visualise the activity of ADH (Figure 3.5). Thereby, recombinant *Kp*NNAT was purified to a chemically active state in a single Ni^{2+}-IMAC step. To the contrary, recombinant *Ef*NNAT yielded no such activity, whereby two arguments are possible i) *Ef*NNAT does not interact with NMN and instead is expected to interact with the alternative NaMN, or ii) recombinant *Ef*NNAT is inactive. The latter is a complex issue concerning how the vector was designed and constructed, as well as subsequent expression and purification steps.

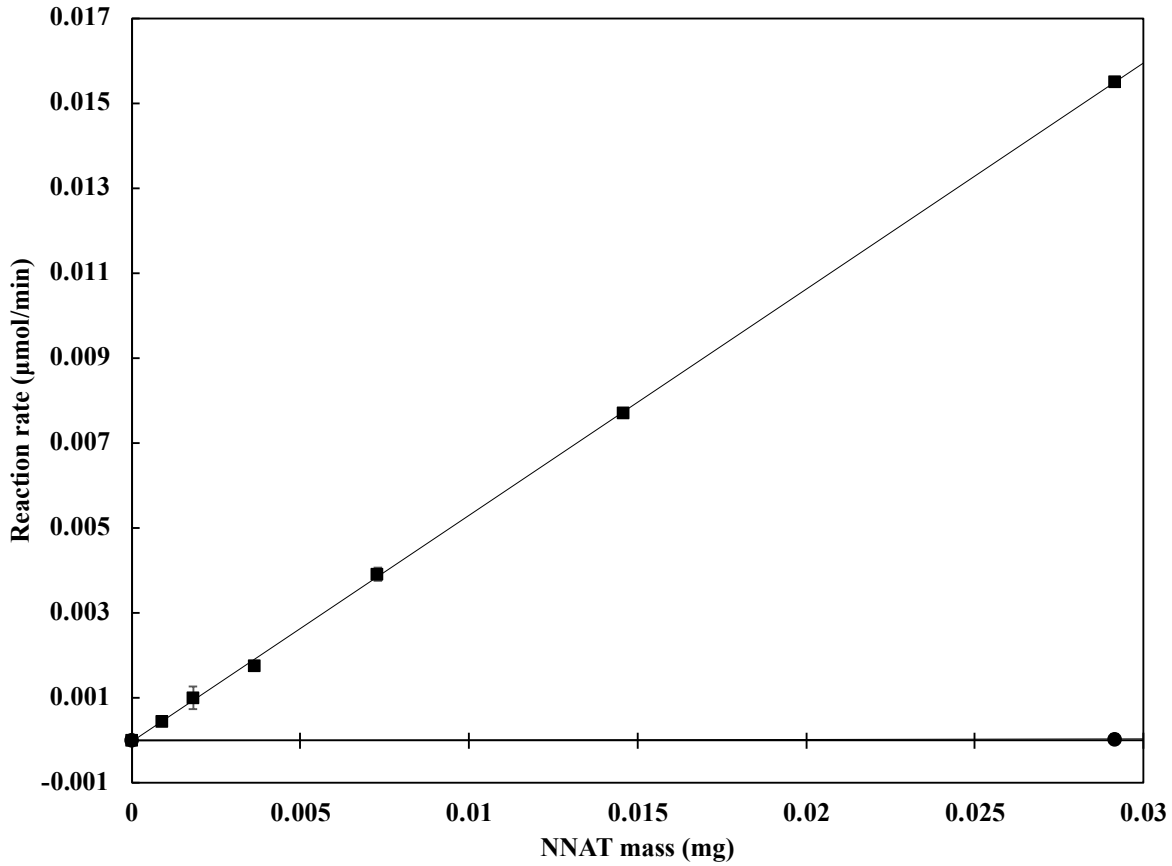

Figure 3.5 ADH-coupled enzyme activity assay of *Kp*NNAT and *Ef*NNAT. The squares, *Kp*NNAT, displays explicit activity, yielding sufficient NADH production for ADH fermentation. The circles, *Ef*NNAT, display negligible activity at the highest NNAT concentration, displaying limited activity relating to the NMN substrate.

Unfortunately, to precisely define *Ef*NNATs inactivity, direct testing of both NNAT substrates must confirm substrate specificity. Unfortunately, NaMN is a costly substrate, which made direct testing impractical. Thereby, the analytical data relating to the activity of both NNAT species are more directly examined and reported on within Chapter 5. Figure 3.5 illustrates and confirms the functionality of the NNAT proteins.

3.5. Discussion

Its critical role in cellular function within prokaryotic organisms makes NNAT an attractive druggable target that can be implemented in developing new-generation antimicrobial chemotherapy. However, several complications prevent its further usage as a druggable target, such as the lack of a 3D structure (especially within ESKAPE species) and the need for kinetic classification of the enzymes. The bottlenecks in these processes are derived from the high-throughput recombinant expression and purification of the relevant NNAT species (Daya et al.,

2022). Thereby, to characterise these NNAT species, the codon-optimised ORFs of *Kp*NNAT and *Ef*NNAT were cloned into pET-28a and pET-11a, respectively. These ORFs were adjoined with a $(His)_6$-tag to enable Ni^{2+}-IMAC as a purification step.

The recombinant overexpression conditions were derived from Jeje *et al.*, (2022) as they used similar ORF structures as presented here. Briefly, NNAT expression was initiated (with 0.5 mM IPTG) at an OD_{600} of between 0.4 – 0.5 and expressed for 6 hours at 30 °C. Under these expression conditions, both *Kp*NNAT and *Ef*NNAT were overexpressed within the soluble fractions of the cell lysate and were subsequently purified using Ni^{2+}-IMAC. The purification conditions were derived, again, from Jeje *et al.,* (2022); however, these conditions are supported mainly by previous and similar purification strategies (Daya et al., 2022; Jeje et al., 2022; Sershon et al., 2009; Zhang et al., 2003). Whereby, upon loading, the recombinant NNAT species interacts with the Ni^{2+}-IMAC column, trapping it and delaying its passage. The subsequent wash steps containing 2 % detergent (Tween-20-PBS) did not influence the interaction between the protein and the column and further assisted in the purification (Figure 3.3). As depicted in Figure 3.3, elution on the Ni^{2+}-IMAC columns was achieved with 500 mM imidazole, visualised by the singular peak elution.

NNAT purity was confirmed using SDS-PAGE, whereby the sample homogeneity was visualised within Figure 3.3, with a single band from the elution sample placed between the 25 kDa and 35 kDa molecular weight marker. This positioning indicated an estimated protein size of approximately 27 kDa in both NNAT species. These protein sizes strongly corroborated the predicted sizes set at 25 kDa for *Kp*NNAT and 24.8 kDa for *Ef*NNAT. Which is in strong corroboration of existing recombinant NNAT proteins, yielding molecular weights of the monomeric protein forms within a range of 20 – 27 kDa, depending on the present affinity tags (Daya et al., 2022; Jeje et al., 2022; Sershon et al., 2009; Zhang et al., 2003).

The purified NNAT proteins were of high concentration, as depicted in Figure 3.4, having a yield greater than 2 mg/ml in protein stock; this was comparable to existing literature (Daya et al., 2022; Jeje et al., 2022). Furthermore, both NNAT enzymes exhibited sufficient stability, with the stock solutions remaining viable for up to 4 weeks after expression when stored at 4 °C. The pure *Kp*NNAT was chemically active, generating sufficient NADH for ADH activity over a series of enzyme concentrations. This chemical activity illustrated that *Kp*NNAT has expressed and folded into a functional state, making it viable for further analysis. Daya *et*

al., (2022) and Jeje *et al.,* (2022) report similar activities for *Kp*NNAT under similar conditions relating to the ADH-coupled enzyme assay. Unfortunately, this cannot be stated for *Ef*NNAT, as seen by the negligible activity displayed by the recombinant enzyme within Figure 3.5. Though *Ef*NNAT has folded correctly (depicted in Chapter 4), the negligible activity indicates a potential substrate dispute or an issue within the vector design.

Currently, no one has successfully demonstrated activity within *Ef*NNAT concerning the NMN substrate. Thereby, it is highly probable that *Ef*NNAT prefers the alternative substrate, namely, NaMN. This substrate preference is corroborated by Sershon *et al.*, (2009) who displayed activity within *Ef*NNATs closest solved familial homolog *Ba*NNAT, using the NaMN substrate. Though they never investigated *Ba*NNATs activity relating to NMN, there was a strong indication that NaMN is the preferred substrate for Gram-positive bacteria. Thereby, the functionality of *Ef*NNAT becomes challenging to prove, as NaMN is required for direct testing. However, NaMN is a costly substrate, and due to financial limitations, its acquisition for confirmational techniques was impractical. Thereby, *Ef*NNATs quality was primarily assessed using structural data, inferring that the enzyme is within a correctly folded state, thereby of sufficient quality for downstream applications. See Chapter 4 for the analysis of the *Ef*NNAT structure.

Due to the observed inactivity of *Ef*NNAT, it would be inappropriate to confidently conclude that the enzyme was adequately purified. The only measure available to support the claim was that the enzyme's structure closely matched the expected characteristics of *Ef*NNAT. However, it is essential to note that this measure alone is insufficient for definitive confirmation. Unfortunately, other techniques, such as Western blotting, which could have provided clearer insights, were not feasible during the time of the study. As a result, the lack of explicit confirmation regarding the purity of *Ef*NNAT remains an unfortunate limitation of this research.

Both NNAT species were recombinantly overexpressed and purified to an acceptable level, having high enzyme yields. The sample purity and quality were sufficient for further downstream application, as *Kp*NNAT showed enzymatic activity and *Ef*NNAT displayed appropriate folding patterns (data displayed in Chapter 4). Further kinetic investigations, which will be reported in later chapters, will provide additional insights into the activity or lack thereof with *Ef*NNAT.

4. Chapter four

Structural influences of the divalent cations

4.1. Introduction

Recent publications have provided an excellent framework for the general fold structure and structural dynamics of *Kp*NNAT and a new reference point for *Ef*NNAT. The presence and type of metal ions are influential within the NNAT enzyme's structural fold, where it is apparent that specific divalent metal ions (Zn^{2+} and Cu^{2+}) can introduce structural perturbations resulting in a complete unfolding of the enzyme structure. This phenomenon emphasises the importance of understanding the influence of the divalent metal ions. As stated previously, the divalent ions will influence *Kp*NNAT and *Ef*NNAT on both a structural and functional level as it plays a role in the structural stabilisations of the intermediates. Additionally, the divalent metal ions serve as a chemical stabiliser advancing hydrolysis through altering the electrophilic character of the enzyme. Thereby, this section aims to discuss the structural influence of different divalent metal ions on both *Kp*NNAT and *Ef*NNAT with respect to ATP binding.

Initially, the fold composition of both NNAT species were tested by far-UV CD. This technique ultimately tests the unequal absorption of circularly polarised light. A result of the interaction between the peptide bonds and the circularly polarised light. The unequal absorption generates a sinusoidal plot representing a culmination of spectra generated by alpha-helices and beta-sheets. These sinusoidal plots provide the global fold composition of the NNAT species. This incredibly sensitive analysis requires small sample volumes at low concentrations and can be used to track fold composition changes. Thereby, NNATs' ability to rotate circularly polarised light was tested in the presence and absence of ATP, $MgCl_2$, $CaCl_2$ and $NiCl_2$, as similarly presented in Jeje *et al*., (2022). This investigation evaluated the impact of divalent metal ions and ATP binding on the folding structure. The resulting data was then correlated with tertiary structural probes, providing a comprehensive understanding of the observed structural dynamics during the binding of divalent metal ions and ATP.

The tertiary structure of both NNAT species was probed using extrinsic ANS fluorescence. As previously stated, ANS is a fluorophore with a high affinity to hydrophobic regions within the protein. Upon binding, ANS experiences an increased fluorescent signal accompanied by a hypso- or hyperchromic shift, depending on solvent accessibility. Thereby, ANS was used as a probe for the tertiary structure of the NNAT species. It can provide information about relative

active sites, global tertiary structure, and may illustrate the chemistry of the relevant metal-binding sites. Extrinsic ANS fluorescence was utilised in the presence and absence of ATP and the relevant divalent metal ions.

Both these techniques were used in the past for *Kp*NNAT, with published data presented by Jeje, *et al.*, (2022) and Daya, *et al.,* (2022). Here, they displayed predominant alpha-helical structures, which were in line with the existing literature.

4.2. Materials

ATP, ANS (Catalogue number: A3125) and DTT were purchased from Sigma-Aldrich (Merck Group, USA). Snakeskin^{TM} dialysis tubing (10K MWCO, 22 mm) was purchased from Thermo Fisher (Thermo Fisher Scientific, USA). Other buffer components and reagents used, such as sodium phosphate, sodium azide, Trizima base, magnesium chloride, nickel chloride, calcium chloride and urea, were purchased from Sigma-Aldrich (Merck Group, USA) and were of analytical quality. Data fittings were performed according to the DichroWeb online tool, and data plots were generated using Microsoft Excel (Microsoft Corporation, USA).

4.3. Methods

4.3.1. Far-UV CD, secondary structural analysis

To analyse the secondary structure of the recombinant *Kp*NNAT and *Ef*NNAT, 5 µM of the stock protein was prepared in PBS diluted with MilliQ water, with 5 mM of the metal ions (i.e. $MgCl_2$, $NiCl_2$ and $CaCl_2$), thereby, buffered in 0.5 mM PBS pH 7.2. This dilution minimised the salt aggregation due to the addition of the metal ions (i.e., $MgCl_2$, $NiCl_2$ and $CaCl_2$). The prepared samples were subjected to far-UV CD spectroscopy at 20 °C using a Jasco J-810 spectropolarimeter (Jasco Inc., Japan), set to a 2.5 nm bandwidth and a 1 nm data pitch. CD spectra were collected between 180-255 nm using a 1 mm pathlength high transparency CD quartz cuvette under continuous nitrogen flush to remove oxygen. A 5 µM aliquot was treated with 8 M urea to denature the protein and subjected to far-UV CD spectroscopy under the same running conditions. To analyse the effect of ATP on the secondary structure, the above conditions were adjusted to 0.5 mM PBS pH 7.2 with 1.25 mM $MgCl_2$ and $CaCl_2$ as well as 0.25 mM ATP. Take note, that the concentrations were adjusted to account for noise generation. Additionally, $NiCl_2$ was later excluded due to its structural interference with both

NNAT species. For each sample, 5 accumulations were automatically collected and averaged; these were collected in triplicate and averaged. The resulting averaged spectra were normalised by calculating the mean residue ellipticity (θ) deg.cm^2.dmol^{-1}.residue^{-1} using Equation 4.1.

$$[\theta] = {}^{(100 \times \theta)}\Big/_{(C.n.l)}$$

Equation 4.1 Mean residue ellipticity.

Where θ refers to the far-UV CD signal in millidegrees, C is the protein concentration in mM, n is the number of residues, and l is the pathlength in cm. The resulting spectra were deconvoluted through DichroWeb analysis using the CONTIN-LL program, the fraction of amino acids in the formation of the specific SSE (i.e. α-helices, β-sheets and random coils) was determined (Miles et al., 2022; Whitmore and Wallace, 2008, 2004). The collected data was corrected for the buffer signal by subtracting the signal produced by the buffer blanks.

4.3.2. Extrinsic ANS fluorescence, tertiary structure analysis

The global tertiary structure of both *Kp*NNAT and *Ef*NNAT was assessed using the binding dynamics of ANS. The samples were prepared to 10 µM of protein in 20 mM Tris-HCl, with 1 mM DTT, pH 7.5 with 1 mM ATP and 5 mM of the respective metal ions ($MgCl_2$, $NiCl_2$, $CaCl_2$). ANS fluorescence was measured at 20 °C using a Jasco FP-6300 spectrofluorometer with Spectra Manager software v1.5.00 (Jasco Inc., Japan). ANS was excited at 395 nm, and emission was monitored between 400 and 650 nm. Fluorescence was detected within a fluorescence quartz cuvette (10 mm pathlength) with a 5 nm excitation bandwidth and a 5 nm emission bandwidth. The samples were read with a 0.5 nm data pitch and 200 nm/min scanning speed. Samples were analysed in triplicate and averaged. All emission spectra were corrected for free ANS as well as buffer absorption.

4.3.3. Monitoring protein aggregation through UV scans

UV scans were performed as supplementary measurements to confirm the structural disruption caused by $NiCl_2$ on the NNAT species and to provide further validation for the observed changes within the previously discussed methodologies. A Jasco v-730 with Spectra Manager software v1.5.00 (Jasco Inc., Japan) was used to measure the absorbance of the samples between the wavelength range of 200 – 400 nm. The samples consisted of NNAT protein at a concentration of 10 µM in 20 mM Tris-HCl, with 1 mM DTT, pH 7.5. The NNAT proteins were incubated in 5 mM $NiCl_2$, $MgCl_2$, and $CaCl_2$. This technique fundamentally derives the

proportion of aggregation and describes the sample's transparency. In this way, it defines the sample's viability within spectroscopic studies. This step was necessary due to observing protein aggregation in the presence of 5 mM $NiCl_2$ for both NNAT species. It was essential to ensure accurate conclusions could be drawn from the obtained data. The UV scans were collected in triplicate and displayed an averaged spectrum.

4.4. Results

*Kp*NNAT and *EfNNAT's* ability to polarise light was tested with far-UV CD. The far-UV CD spectral analysis was performed at room temperature using a Jasco J-810 spectropolarimeter. The spectral analysis was conducted with a quartz cuvette with a 2 mm pathlength, using 5 µM of protein, in the presence of 5 mM $MgCl_2$, $NiCl_2$, or $CaCl_2$. Further, denatured samples were analysed, where aliquots were denatured using 8 M urea. The data were deconvoluted using the online resource DichroWeb. The resulting spectra are depicted in the following figures.

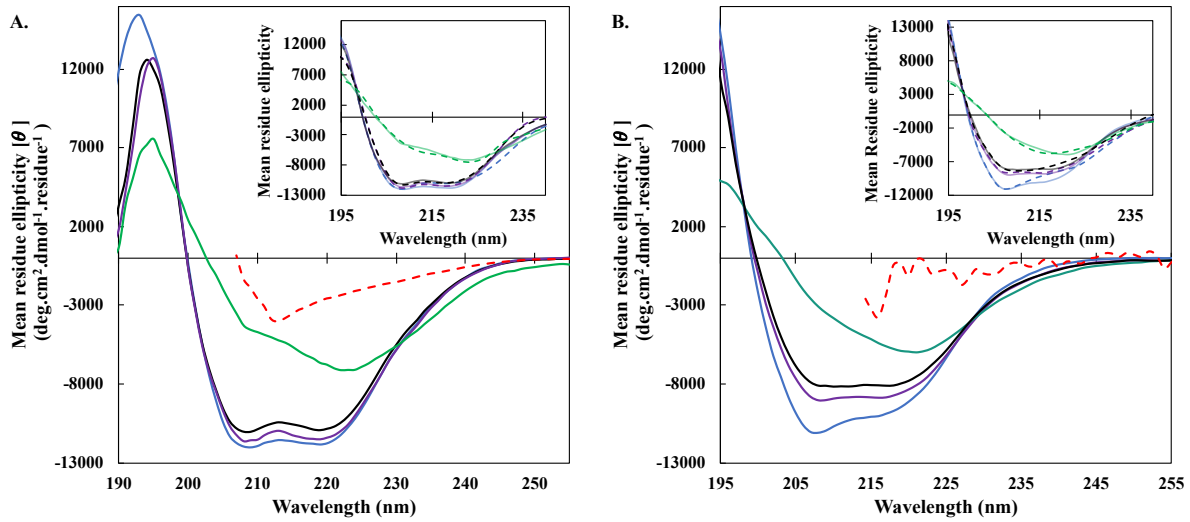

Figure 4.1 Secondary structural analysis of *Kp*- and *Ef*-NNAT through far-UV CD. The CD spectra of *Kp*NNAT (A) and *Ef*NNAT (B) are in the figure above, with the DichroWeb fitted data presented in the respective insets. The spectral data of NNAT samples were analysed using different metal ions: no metal ion (blue), 5 mM $MgCl_2$ (purple), 5 mM $NiCl_2$ (green), and 5 mM $CaCl_2$ (black). Dashed red lines represent denatured samples. The insets' colour scheme remains consistent, with solid lines representing experimental plots and dashed lines representing fitted plots. Overall, *Kp*NNAT and *Ef*NNAT predominantly consist of alpha-helices and beta-sheets. While there is a slight decrease in signal in the presence of $CaCl_2$ and $MgCl_2$ compared to native structures, their compositions are largely preserved, but the presence of $NiCl_2$ results in a substantial loss of alpha-helical content in both *Kp*NNAT and *Ef*NNAT. The DichroWeb analyses provided well-fitting plots, with an average NRMSD (Normalised Root Mean Square Deviation) of 0.146 Å for *Kp*NNAT and 0.089 Å for *Ef*NNAT, indicating successful deconvolution of the experimental data.

Kp- and *Ef*-NNAT were primarily composed of alpha-helices and beta-sheets (Figure 4.1), which is consistent with most NNAT species due to the largely conserved nucleotide-binding domain. Here, 5 mM $MgCl_2$ and 5 mM $CaCl_2$ preserved these compositions, seen through the positive peak at 190 ± 0.5 nm and the two troughs at 208 ± 0.5 nm and 220 ± 0.5 nm. Notably, in both NNAT species, there was a slight signal loss in the presence of $MgCl_2$ and $CaCl_2$, though they still retain a similar structure compared to the native complexes. Further, there was a substantial loss of alpha-helical content in the presence of $NiCl_2$, which suggests that Ni^{2+} might be involved in partial structural disruptions (Figure 4.1). To further understand the structural changes resulting from the association of the divalent metal ions, the CD data were deconvoluted with the online source DichroWeb, to show the percentage of each secondary structural element (SSE), represented in Table 4.1.

Table 4.1 Global secondary structure composition of *Kp*NNAT and *Ef*NNAT.

A.

SSE	SSE composition (%)			
	No Divalent Cation	**5 mM $MgCl_2$**	**5 mM $NiCl_2$**	**5 mM $CaCl_2$**
Helix	36.3	31.7	18.1	36.8
Sheets	16.9	14.5	21.1	17.4
Turns	24.4	20.4	16.3	21.4
Unordered	22.5	33.4	44.5	24.5

B.

SSE	SSE composition (%)			
	No Divalent Cation	**5 mM $MgCl_2$**	**5 mM $NiCl_2$**	**5 mM $CaCl_2$**
Helix	20.7	20.2	3.4	16.9
Sheets	31.4	28.6	44.9	30.2
Turns	20.7	23.5	22.3	21.0
Unordered	27.1	27.6	29.4	32.0

Table 4.1 A) denotes the global secondary structure composition of *Kp*NNAT, and B) is that of *Ef*NNAT. *Kp*NNAT retains the predominate alpha-helical structure in the native structure and in the presence of 5 mM Mg^{2+} and Ca^{2+}, having similar percentage distributions for most structural elements. Only a slight increase in the unordered fold is present in the presence of Mg^{2+}. *Ef*NNAT shows similar compositions when comparing the native structure and *Ef*NNAT in the presence of Mg^{2+}; there is a slight loss of alpha-helical content in the presence of Ca^{2+}. As seen in Figure 4.1, in the presence of Ni^{2+}, there is a substantial loss of the alpha-helical content in both *Kp*- and *Ef*-NNAT.

The data presented in Table 4.1 confirmed the loss of helical content in the presence of 5 mM $NiCl_2$. This total loss was 18.2 % and 17.3 % for *Kp*NNAT and *Ef*NNAT, respectively. The data, however, confirmed that the global composition of the SSE was predominantly alpha-helical and beta-sheeted. Predominantly beta-sheeted for *Ef*NNAT, owing to 31.4 % of sheeted content in the apo-enzyme structure. *Kp*NNAT was predominantly alpha-helical, owing to a 36.3 % helical content within the apo-enzyme structure. There were slight changes in these

ratios in the presence of the varying metal ions, which confirmed that these co-factors influence the structural dynamics of the respective enzymes to a limited extent (Table 4.1). To further illustrate the structural dynamics imposed by these metal ions, extrinsic ANS fluorescence was performed to highlight the global tertiary structure of the enzymes in the presence and absence of ATP and the metal ion co-factors.

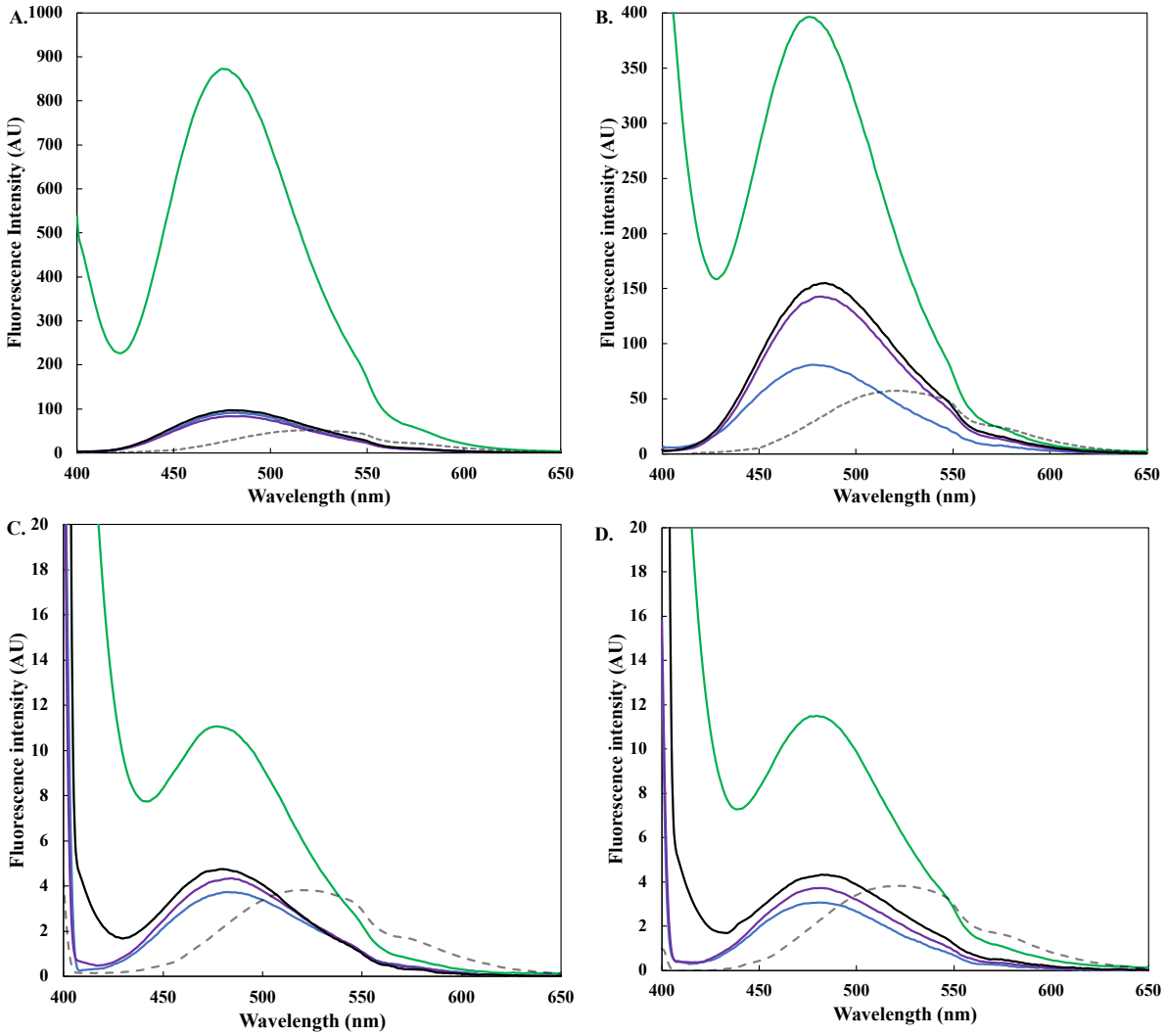

Figure 4.2 Extrinsic ANS fluorescence analysis of *Kp*NNAT and *Ef*NNAT. The emission spectra of *Kp*NNAT in the absence of 1 mM ATP (A), in the presence of 1 mM ATP (B), *Ef*NNAT in the absence of 1 mM ATP (C), and in the presence of 1 mM ATP (D). NNAT with no metal ion present is represented in blue, NNAT with 5 mM $MgCl_2$ is represented in purple, NNAT with 5 mM $NiCl_2$ is represented in green, and NNAT with 5 mM $CaCl_2$ is represented in black. (Figure 4.2 A-B) All emission spectra had a blue shift in the wavelength maximum and an increased fluorescent yield, indicating ANS binding. In both conditions, there was an increased fluorescent signal in the presence of 5 mM $NiCl_2$, indicating an increased hydrophobic binding surface agreeing with partial structural disruptions. This signal increase was mitigated by ATP binding. In the absence of ATP (Figure A), the emission spectra between the apo-*Kp*NNAT structures were comparable to that of the presence of both $MgCl_2$ and $CaCl_2$. An increased fluorescent yield was speculated to arise from dynamic structural changes to accommodate the ATP molecule and consequent ligands in the presence of ATP. (Figure 4.2 C-D) All emission spectra had a blue shift in the wavelength maximum and an increased fluorescent

yield, indicating ANS binding. In both conditions, there was an increased fluorescent signal in the presence of 5 mM $NiCl_2$, indicating an increased hydrophobic binding surface agreeing with partial structural disruptions. The emission spectra between the apo-*Ef*NNAT structures were comparable to that of the presence of both $MgCl_2$ and $CaCl_2$, with similar observations pertaining to the presence of 1 mM ATP.

The structural dynamics illustrated in Figure 4.2 strongly agreed with the data presented in Figure 4.1. In the presence of $NiCl_2$, the enzyme structure was partially disrupted; however, this structural destabilisation was mitigated to some extent in the presence of 1 mM ATP, confirming the stabilising effect present within this complex set of interactions. As apparent in Figures 4.1 and 4.2, the structural dynamics of the divalent metal ions Mg^{2+} and Ca^{2+} were comparable to the native NNAT structures. This observation indicated that these co-factors had no discernible structural impact on the NNAT species relating to the global secondary or tertiary structure. In the presence of 1 mM ATP, however, there was an increase in the fluorescent yield for *Kp*NNAT (Figure 4.2), which suggested an increased hydrophobic binding area. This indicates either i) the binding of ATP in the presence of either $MgCl_2$ or $CaCl_2$ results in an opening of the central hydrophobic cleft, thereby attempting to accommodate potential future ligands, or ii) the presence of both ATP and these divalent metal ions results in slight structural destabilisation. These observations only relate to *Kp*NNAT and not *Ef*NNAT, as seen in Figure 4.2, whereby no such structural change was observed within *Ef*NNAT. This lack of interaction could draw two possible conclusions i) there are no/ limited interactions between ATP and *Ef*NNAT, or ii) ATP association does not induce large structural changes within the tertiary level. If it is the former, the limited interaction may be a comment on vector design and the inclusion of the $(his)_6$-tag. These conclusions, however, can only be confirmed by ATP association studies (see Chapter 5).

UV scans were used as supplementary data to confirm that $NiCl_2$ partially disrupts the structure of these NNAT species and to provide further validation to the observations. Here, measuring the sample (10 μM of NNAT protein) absorbance between 200 – 400 nm. The characteristic spectra of pure protein were used to assess sample quality and viability. This validation step was deemed necessary as, in the presence of 5 mM $NiCl_2$, both NNAT species had some aggregation. This precautionary step ensured that accurate conclusions were drawn from the data obtained. As seen in Figure 4.3, the sample with the 5 mM $NiCl_2$ yielded insoluble precipitant, which ultimately influenced the transparency of the sample. Thereby, the data obtained under these conditions are subject to low confidence. This trend was repeated at lowered concentrations of $NiCl_2$ (data not shown), but unfortunately, even minimal

concentrations (as low as 60 µM) yielded precipitant. Therefore, it was concluded that no further work would be done in the presence of $NiCl_2$ as the low confidence in the data made valid conclusions impossible.

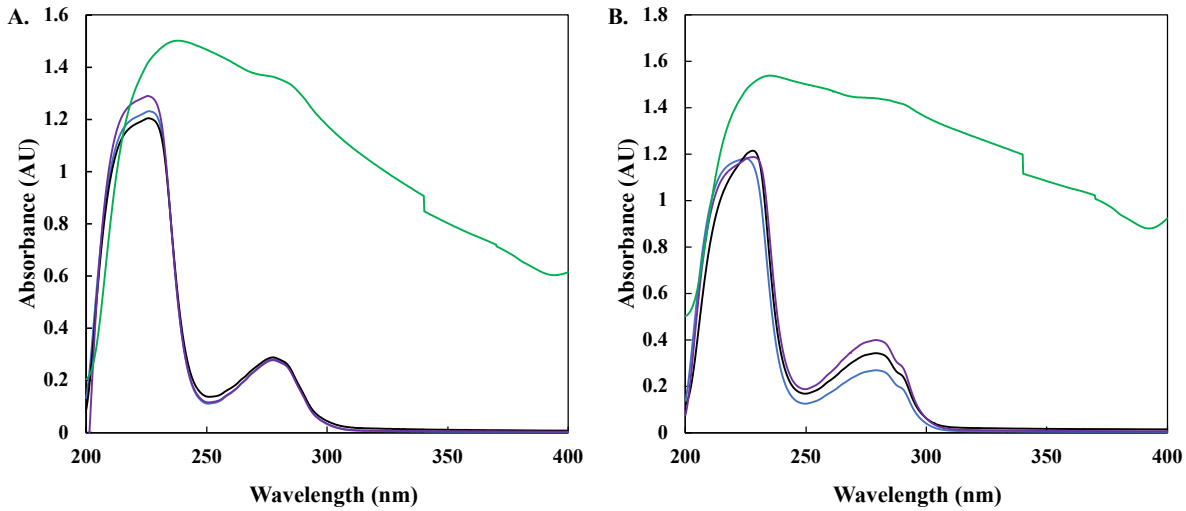

Figure 4.3 UV-scans of *Kp*NNAT and *Ef*NNAT. *Kp*NNAT (A) and *Ef*NNAT (B). NNAT with no metal ion present is represented in blue, NNAT with 5 mM $MgCl_2$ is represented in purple, NNAT with 5 mM $NiCl_2$ is represented in green, and NNAT with 5 mM $CaCl_2$ is represented in black. A and B; the spectra are comparable between the apo-NNAT structure and that in the presence of 5 mM $MgCl_2$ and $CaCl_2$. The signal is indistinguishable in the presence of 5 mM $NiCl_2$ because of low sample transparency.

Given the further exclusion of investigations relating to $NiCl_2$, the following results will solely depict the absence of the divalent metal ions and the presence of $MgCl_2$ and $CaCl_2$. These samples were excluded to avoid potential erroneous assumptions based on the observations, further justified by the fact that most of the techniques employed were spectroscopic. Therefore, the samples must be transparent for any accurate measurement. The presence of $MgCl_2$ and $CaCl_2$ had minor influences on the global secondary structure and, to an even more limited extent, on the global tertiary structure. At this level, however, a large structural change was observed for *Kp*NNAT in the presence of ATP (Figure 4.2). Thereby, to expand on these observations, additional far-UV CD spectra were obtained under various conditions: 0.25 mM ATP alone, without divalent metal ions and in the presence of 1.25 mM $MgCl_2$ and $CaCl_2$. Note that the concentration of the divalent metal ions was adjusted as the combination of ATP and the divalent metal ions yielded too much noise for any reliable data to be acquired. Figure 4.4 reflects the far-UV CD spectra generated under the abovementioned conditions, where the data were deconvolved using the DichroWeb online tool.

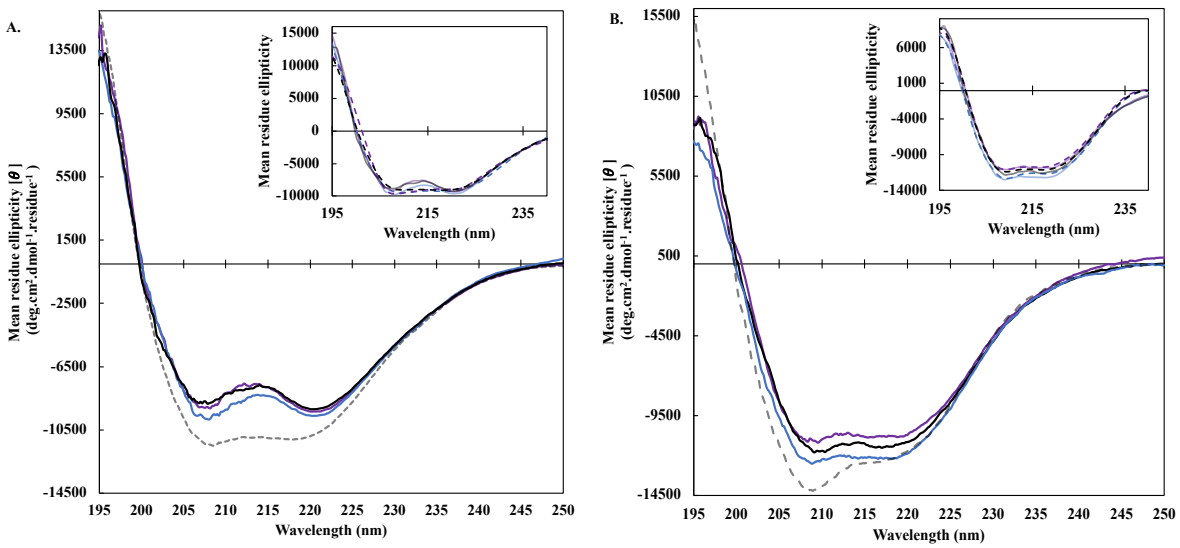

Figure 4.4 Far-UV CD of *Kp*NNAT and *Ef*NNAT in the presence of 0.25 mM ATP. The above figure represents the far-UV CD spectra generated for *Kp*NNAT (A) and *Ef*NNAT (B) in the presence of 0.25 mM ATP, with the insets showing the fitted data from the DichroWeb analysis. In blue is the absence of divalent metal ions, in purple is the presence of 1.25 mM $MgCl_2$, in black is the presence of 1.25 mM $CaCl_2$, and the dashed grey line represents the respective apo-enzyme structures used as a reference. The insets follow the same colour scheme, with the experimental plots represented by the solid plots and the fitted data represented by the dashed lines. (Figure 4.3 A) *Kp*NNAT displayed apparent structural changes within the presence of 1.25 mM ATP, a loss in signal intensity, and a shift in the structural composition were clear indicators of ATP association. Seen across all conditions. (Figure 3.4 B) *Ef*NNAT displayed structural changes but to a lesser extent, indicating a loss of alpha-helical content. These observations were seen across all conditions.

Structural changes on the secondary level were seen in *Kp*NNAT and *Ef*NNAT in the presence of 0.25 mM ATP. The structural changes were more prominent within *Kp*NNAT than in *Ef*NNAT. However, interaction in both NNAT species was apparent. Interestingly, these structural changes were consistent across all conditions, regardless of the divalent metal ions. This observation was suggestive that the NNAT enzymes could bind/ interact with ATP regardless of the present/ absent divalent metal ion. These observations were confirmed through deconvolved data obtained from the online tool DichroWeb. Within Figure 4.4, the fitted data, as interpreted by DichroWeb, has been superimposed over the experimental plots to indicate the deconvolution quality. Overall, the fitted data was relatable to the experimental plots, yielding averaged NRMSD values of 0.130 Å and 0.079 Å for *Kp*NNAT and *Ef*NNAT, respectively. Table 4.2 denotes the deconvolved SSE compositions of both NNAT species in the presence and absence of ATP and the respective divalent metal ions.

Table 4.2 Global secondary structure composition of *Kp*NNAT and *Ef*NNAT in the presence of 0.25 mM ATP

A.

SSE	SSE composition (%)					
	No metal ion		1.25 mM $MgCl_2$		1.25 mM $CaCl_2$	
	Reference	Fitted	Reference	Fitted	Reference	Fitted
Helices	32.5	28.3	36.6	35.1	34.1	24.5
Sheets	17.6	19.1	18.1	19.6	17.8	18.8
Turns	23.7	21.4	24.7	20.1	25.6	21.3
Disordered	26.6	31.1	20.6	25.3	21.7	35.3

B.

SSE	SSE composition (%)					
	No metal ion		1.25 mM $MgCl_2$		1.25 mM $CaCl_2$	
	Reference	Fitted	Reference	Fitted	Reference	Fitted
Helices	20.7	24.8	20.2	24.6	16.9	24.2
Sheets	31.4	21.9	28.6	23.1	30.2	22.8
Turns	20.7	22.0	23.5	22.0	21.0	22.7
Disordered	27.2	31.2	27.6	30.3	32.0	30.4

Table 4.2 depicts the DichroWeb deconvolution of the far-UV CD spectra of *Kp*NNAT (A) and *Ef*NNAT (B) in the presence of 0.25 mM ATP. This compared the referenced structures (NNAT under similar conditions) to the presence of ATP and the respective metal ions (Table 4.2 A). *Kp*NNAT was largely comparable to the reference structure across all conditions, with a slight loss of alpha-helical content and a consequent increase in beta-sheet content. However, the SSE compositions were not precisely comparable to one another. The presence of $MgCl_2$ yielded a larger proportion of alpha-helices and a smaller proportion of disordered content. (Table 4.2 B) Across all conditions, an increased proportion of alpha-helical content within *Ef*NNAT was present, with a proportionate decrease in beta-sheeted structures. Within *Ef*NNAT, there was an additional increase in disordered content in the absence of the divalent metal ions and the presence of 1.25 mM $MgCl_2$.

Both Figure 4.4 and Table 4.2 collectively suggest that ATP association induces comparable structural changes regardless of the presence of divalent metal ions, in *Kp*NNAT and *Ef*NNAT. In the case of *Kp*NNAT, including 0.25 mM ATP led to a decrease in alpha-helical content. The largest decrease of 9.6% (Table 4.2) was observed in the presence of 1.25 mM $CaCl_2$. Additionally, there was an increase in beta-sheeted content and a general increase in disordered folds. Interestingly, the presence of 1.25 mM $MgCl_2$ in *Kp*NNAT resulted in less pronounced structural perturbations, including a 1.5% decrease in alpha-helical content, a 1.5% increase in beta-sheeted content, and a 4.7% increase in disordered folds. These changes represented increases and decreases greater than two-fold compared to the other conditions, namely, the absence of metal ions and the presence of 1.25 mM $CaCl_2$.

On the other hand, *Ef*NNAT exhibited a contrasting trend. It showed an increase in alpha-helical content, with the largest increase of 7.3% observed in the presence of 1.25 mM $CaCl_2$. Additionally, there was a 3.1% increase in alpha helical content in the absence of metal ions and a 3.4% increase in the presence of 1.25 mM $MgCl_2$. Notably, a decrease in beta-sheeted content was relatively consistent across all conditions. However, there was a comparable increase in disordered content within the absence of divalent metal ions and in the presence of 1.25 mM $MgCl_2$. This trend was not observed in the presence of 1.25 mM $CaCl_2$, which showed a 1.6% decrease in disordered content.

Take note; these observations suggest an interaction between *Ef*NNAT and ATP in similar ways as was implied for *Kp*NNAT and ATP. However, these observations did not indicate the extent of these interactions as they offered no quantifiable measure. Here, it simply qualitatively suggests that there may be an interaction between the binding species. This limitation is important to note, considering later conclusions within Chapter 5.

A closer inspection of the SSE composition showed that the metal ions alone limited structural change. However, the varying metal ions seem to have a distinctive structural impact within the presence of ATP. These observations confirmed similar trends in Figure 4.2 for *Kp*NNAT, relating to the global tertiary structure. Nevertheless, these observations were not as clearly defined for *Ef*NNAT as, on a secondary level, limited structural changes implied similar interactions between *Ef*NNAT and ATP. However, on a tertiary level, no changes were observed. Together, these observations imply a weakened interaction between *Ef*NNAT and ATP. However, the techniques used did not offer quantifiable measures to test this. Therefore, ATP association was directly quantified under similar conditions (see Chapter 5).

4.5. Discussion

To comprehensively understand the binding event between ATP and NNAT, it is crucial to elucidate the intricate structural dynamics involved. Jeje, *et al.,* (2022) illustrated the complex structural dynamics of these binding events for *Kp*NNAT, commenting on how *Kp*NNAT's structure changes after the association of ATP, divalent metal ions and NMN. It is well established that ATP binding proteins commonly elicit the help of co-factors, such as divalent metal ions, to assist in stabilising the binding event and the catalytic process by stabilising intermediate states. NNAT, like other ATP-binding proteins, follows a similar pattern, with

extensive evidence supporting the preference for specific divalent metal ions (Jeje et al., 2022; Sorci et al., 2007; Magni et al., 2004). Most NNAT species require the presence of Mg^{2+} in order to maintain maximal activity (Magni et al., 2004). However, in some instances, alternative divalent metal ions are preferred. Human NNAT-1 (hNNAT-1), for instance, can catalyse the adenylation of NMN/NaMN in the presence of Zn^{2+} and maintains a similar rate of activity compared to the presence of Mg^{2+} (Sorci et al., 2007). This example illustrates the variability within differing NNAT species, referring to these divalent metal ions' structural and functional impact. This section aims to discuss the structural impact of different divalent metal ions on the ATP binding event within both *Kp*NNAT and *Ef*NNAT, providing insights into the intricate interplay between ATP and NNAT.

From the data presented, divalent metal ions have a structural impact on multiple forms of the structural hierarchy, resulting in structural alterations causing variation with the apo-enzyme conformation. Overall, the far-UV CD data in Figure 4.1 strongly supports the notion that *Kp*NNAT and *Ef*NNAT are predominantly alpha-helical and beta-sheeted. This observation aligns with the characteristic structural features of most NNAT species, as they commonly possess a central α/β domain that functions as a modified dinucleotide binding Rossmann-fold (Lau et al., 2009; Magni et al., 2004). This Rossmann fold comprises a parallel β-sheet core flanked by several α-helices. As discussed earlier, the shared secondary conformation observed in NNAT species primarily arises from highly conserved active residues. Notably, the SXXXXR region and the (H/T)XGH region play crucial roles in determining this common structural conformation (Magni et al., 2004; Saridakis and Pai, 2003; Sorci et al., 2007).

This shared secondary conformation persists in the presence of 5 mM $MgCl_2$ and $CaCl_2$ for both NNAT species (Figure 4.1). There is a slight loss of alpha-helical content under these conditions, but that only confirms an interaction between the divalent metal ions and the two NNAT species, as these differences are not large enough to warrant concern about the introduction of structural perturbations. Notably, the presence of $NiCl_2$ has caused substantial structural alterations in both NNAT species to such an extent that partial unfolding was plausible.

Within *Kp*NNAT, alpha-helical content was decreased with a consequent increased disordered content (Figure 4.1). Accounting for a 16.8 ± 2.8 % loss of alpha-helical content and a 17.7 ±

5.8 % increase in disordered content, using the other structural compositions as references (Table 4.1, A). Similarly, but more drastic in trend, *Ef*NNAT had a 31.1 ± 9.5 % decrease in alpha-helical content, again using the other structural compositions as reference (Table 4.1, B). This trend illustrates that the introduction of $NiCl_2$ has caused a drastic decrease in the composition of ordered content. This conformational disruption has largely been confirmed by Jeje, *et al.*, (2022) showing correlating values as represented in Table 4.1, further annotating the partial structural loss attributed to the presence of $NiCl_2$. Where Jeje, *et al.,* (2022) further illustrate that similar and even worsened structural deconstructions result from alternative divalent metal ions. This corroboration confirmed the partial destabilisation of $NiCl_2$ while also illustrating that $ZnCl_2$ and $CuCl_2$ cause even greater destabilisations, with $CuCl_2$ acting like a complete denaturant. The data in Figure 4.1 and Table 4.1 suggests that NNAT can interact with multiple divalent metal ions. However, the structural impact solely depends on the present metal ion species. Further, the literature suggests these structural changes are not limited to the secondary structural level, corroborating the extrinsic ANS data (Jeje et al., 2022; Olland et al., 2002; Sershon et al., 2009).

Jeje, *et al.,* (2022) elaborates on ATP binding dynamics within *Kp*NNAT, suggesting that structural changes are apparent in all structural hierarchies. This postulates that the association of ATP in the presence of an applicable divalent metal ion induces the formation of a more open enzyme conformation. A similar observation is stated by Sershon *et al.*, (2009) suggesting similar structural alterations within *Bacillus anthracis* NNAT (*Ba*NNAT). This structural change is involved in the allowance for product release. These examples of *Kp*NNAT and *Ba*NNAT are attributable to the current research context as the former deals with one of the research topics, i.e. *Kp*NNAT, and the latter discusses the closest structural homolog to *Ef*NNAT that has been characterised. With these statements, the extrinsic ANS fluorescence data, as presented in Figure 4.2, strongly agree with the suggestion of a tertiary-level structural change upon ATP binding. However, this change solely relates to *Kp*NNAT, as no such structural change was present within *Ef*NNAT.

For simplicity, Figure 4.2 represents the extrinsic ANS fluorescence of the NNAT-bound ANS compared to the free ANS. As previously established, the binding of ANS is typically associated with increased fluorescent yield and a hypsochromic shift. However, the latter primarily depends on how solvent-exposed the bound ANS fluorophore might be. Examining the metal ion association, *Kp*NNAT and *Ef*NNAT have limited structural alterations, as ANS

binds, as seen through the previously established characteristics. The effect of the divalent metal ions is negligible, as for the most part, the apo-enzyme structures were comparable with those associated with $MgCl_2$ or $CaCl_2$ (Figure 4.2). For *Ef*NNAT, adding 1 mM ATP yielded little alteration to the fluorescent spectrum. As a previously established limitation, this can relate to one of two explanations i) there are no structural changes associated with ATP binding, or ii) the lack of structural changes might suggest no/ limited ATP association. Unfortunately, the techniques as presented do not offer sufficient justification for either and require a more detailed perspective of the binding event to consider any conclusive answer. For *Kp*NNAT, on the other hand, there was an apparent increase in the fluorescence yield compared to the apo-enzyme structure (Figure 4.2). This observation strongly agrees with the data presented by Jeje, *et al.,* (2022) and suggests a similar structural trend as observed by Sershon, *et al*., (2009). The increase in fluorescent yield in the presence of both ATP and a divalent metal ion causes a structural change that facilitates improved/ increased ANS binding, which strongly agrees with the structural accommodations described by Sershon, *et al*., (2009).

Following the ATP-related structural changes imposed upon *Kp*NNAT, further far-UV CD spectra for both NNAT species (under similar conditions) were obtained in the presence of 0.25 mM ATP. The acquisition of additional CD data was primarily driven by the thorough explanation presented by Sershon, *et al*., (2009). As presented in Figure 4.4 and Table 4.2, the inclusion of ATP induces structural changes in both *Kp*NNAT and *Ef*NNAT regardless of the present divalent metal ions. However, it is worth noting that there was no indication to the extent of the ATP association. From this, two primary conclusions were possible, namely, i) ATP has association potential with both NNAT species regardless of whether a divalent metal ion is present, and ii) ATP in conjunction with the divalent metal ions introduce distinctive structural changes on all structural hierarchies for *Kp*NNAT and on a secondary level for *Ef*NNAT. Both are anticipated signs of ligand association, i.e., consequent structural changes.

Remarkably, this information aligns with the findings of Sershon, *et al*., (2009) who conducted a comprehensive analysis of the structural and kinetic aspects to evaluate the biochemical reaction facilitated by *Ba*NNAT. Here they postulate, through a combination of X-ray crystallography and several kinetic studies using NaMN, ATP and NaAD, that the association of the NMN/NaMN yields small structural changes. However, including ATP/ NaAD introduces structural changes that can be primarily monitored on the secondary level, revealing

that three regions of the *Ba*NNAT underwent these changes to accommodate ATP and the product (NaAD) release. These regions include i) an alteration of the first few beta-strands and alpha-helices for the initial association of the NaMN/ NMN substrate, ii) a shift in the central beta-sheet composition that facilitates a stacking interaction with the adenine group of the ATP, and iii) an alteration near the dimer-interface that facilitates substrate binding control. From Figure 4.4 and Table 4.2, a clear structural reform occurs on the secondary level for both NNAT species, which mainly affected the ordered conformations. Structural changes occur within the central beta-sheets to assist in ATP binding. This suggestion strongly agrees with the observations presented by Sershon, *et al*., (2009). Thereby, ATP association is assisted by the enzyme structure and stabilised by the presence of the divalent metal ion (Jeje et al., 2022; Magni et al., 2004; Sershon et al., 2009; Zhang et al., 2002). The latter statement considers the findings presented in Figure 4.2, where the combination of $NiCl_2$ and ATP mitigated the structural destabilisation enforced by the Ni^{2+} ions.

Further, the structural variations imposed by varying divalent metal ions in conjunction with ATP suggest alternative interactive forces. These forces enable the ATP molecule to be active within the enzyme structure. For instance, within most NNAT enzymes, the ATP molecule is required to bind within a bent conformation to place the necessary stress on the α-β phosphate bonds to enable its cleavage (Magni et al., 2004; Olland et al., 2002; Zhang et al., 2003). This idea becomes apparent when considering NNAT activity, as in the absence of the divalent metal ions or within the presence of $CaCl_2$, the NNAT enzymes display negligible activity (see in Chapter 5). Provided ATP could associate with the enzyme, theoretically, the catalytic mechanism should continue in the presence of $CaCl_2$. However, in the presence of $CaCl_2$, the structural change on the secondary level seems similar to the other conditions. This suggests that ATP may have a similar binding orientation within these conditions and an alternate binding mode in the presence of $MgCl_2$, which might explain why only $MgCl_2$ induces activity within the enzyme. Whereby, one can speculate that this might be related to the highly bent conformation of the ATP molecule, where perhaps only in the presence of $MgCl_2$ is this highly bent conformation plausible.

In conclusion, the co-factors, the divalent metal ions, yielded limited structural changes within any of the hierarchical levels. Whereby only within the combined presence of ATP and these co-factors was a structural change apparent. Here, the absence of the co-factors and the presence of $CaCl_2$ yielded similar structural changes within the presence of ATP, suggesting

that these conditions facilitate similar conformational incorporations of the ATP molecule. Moreover, given the differences in the presence of $MgCl_2$, the conformational involvement in *Kp*NNATs activity was highly suggestive. It was postulated that the presence of $MgCl_2$ enabled ATP to bind within the required bent conformation enabling it to be active within the enzyme structure.

5. Chapter five
Kinetic influence of divalent metal ions

5.1. Introduction

The parametrisation of the NNAT kinetic event is a slow-moving process which is reflected in the current literature (Daya et al., 2022; Magni et al., 2004). This bottleneck is primarily due to the reliance on the ADH coupled-enzyme assay as the only technique that enables any kinetic parametrisation of the NNAT enzyme. Though alternative techniques exist, such as discontinuous reverse-phase chromatography or, even more recently, isothermal-titration calorimetry, these techniques are still quite time-consuming and, for anything as simple as base activity checks, makes utilising these techniques a tedious and laborious process (Emanuelli et al., 1996; Yoshino and Imai, 2013). Thereby, limited kinetic data is available for many of the currently researched NNAT species, and almost no relevant data has been available for *Kp*NNAT and *Ef*NNAT until recently. Daya, *et al.,* (2022) presented the first account of *Kp*NNAT activity alongside some rate constants associated with the binding of ATP. Primarily seen through ITC, the paper solely comments on the ATP binding event in the presence of $MgCl_2$ with no reflection on the other divalent metal ions. Thereby, with limited account for the kinetic parameters relating to the enzyme mechanics, parametrisation needs to be performed on a larger scale. This section will introduce the essential aspects of specific parametrisation steps relating to the ATP binding event within the relevant NNAT species.

As stated previously, researchers heavily rely on the ADH-coupled enzyme assay for the classification and parameterisation of the NNAT kinetic event. Historically, this technique served as a validation step for various procedures, including confirming the validity of NNAT and validating alternative techniques that offer kinetic parameters. Though this technique provides "pseudo" values, as is the case for our lab being the "pseudo"- specific activity, the presented information is still of incredible value.

Assuming the mechanisms of the coupled enzyme kinetics, any alteration or deviation from the pre-determined norm indicates the action of the relevant NNAT species. Basic assumptions such as kinetic influences of specific molecules can still be tested to great effect, though the direct quantification becomes limited. Thereby, the influence of the divalent metal ions will be tested utilising the ADH-coupled enzyme assay. This technique is employed as it provides a sufficient indication of the kinetic activity of the relevant enzyme. To such an extent, more

direct quantification steps are not yet necessary or impactful. However, to additional information relating to specific kinetic events are still required. Therefore, necessitating the use of more advanced techniques such as stopped-flow binding studies.

The applications of stopped-flow, as described by Patel *et al.*, (2014) offer a fast-paced screening technique that enables the isolation of specific kinetic events depending on the experimental design. As presented by Patel *et al.*, (2014) this technique offers the ability to parametrise the entirety of the ATP-turnover cycle within the DNA binding protein MCAK. This utilisation presents clear benefits when applied to the NNAT systems as it directly quantifies the ATP association event. Thereby, as previously discussed, with the brief summation, stopped-flow is a rapid mixing technique that measures the progression of a chromogenic signal immediately after mixing. This rapid monitoring ability enables direct quantification from the theoretical start of the kinetic event. Here, the fluorophore Mant-ATP will be utilised, with the Mant group being the signal-producing compound. When Mant interacts with the protein, the fluorescent signal increases. This fluorescence change can be utilised to track the Mant-ATP association. By analysing the fluorescent changes, it is possible to extrapolate the association rate constants. This section will parametrise the ATP binding event concerning the divalent metal ions, further providing inferences of their kinetic impact on the enzyme mechanics.

5.2. Materials

NMN, ATP, Mant-ATP (2'/3'-O-(N-Methyl-anthranilate)-adenosine-5'-triphosphate) (Catalogue number: 18723), and DTT were purchased from Sigma-Aldrich (Merck Group, USA). Other reagents used, such as Trizima base, sodium phosphate, sodium azide, magnesium chloride, and calcium chloride, were all of the analytical grade and purchased from Sigma-Aldrich (Merck Group, USA).

5.3. Methods

5.3.1. ADH coupled enzyme assay of NNAT species

The enzyme reaction scheme largely followed that as presented in Chapter 2. Here a modified ADH-coupled enzyme assay was performed as previously presented (Daya et al., 2022; Jeje et al., 2022). NADH production was monitored at 340 nm as per the activity of alcohol ADH.

The coupled enzyme assay was utilised to determine the "pseudo"-specific activity of the NNAT enzymes, thereby providing a quantifiable measure of whether they were active. The measurements were made on a Jasco V-730 UV-visible spectrophotometer (Jasco Inc, USA), using a 10 mm pathlength quartz cuvette. A dilution series of the protein, with a starting concentration of 1.6 µM, was prepared within the reaction buffer, being filtered 100 mM Tris-HCl, pH 9 supplemented with 1 % (v/v) ethanol, 1 mM ATP, 5 mM of the respective metal salts (i.e. $MgCl_2$ and $CaCl_2$) and 1 U/ml ADH stock. The reaction was initiated using 1 mM NMN and monitored for 1 minute, measuring the increasing signal at 340 nm. The raw data were processed and plotted using Microsoft Excel (Microsoft Corporation, USA), as only linear regressions were required for this data set. The absorbance was corrected to µmole (using the extinction coefficient: 6220 $M^{-1}.cm^{-1}$), which was plotted against the reaction time (minutes). Here, the linear regression slope represents the reaction rate in µmol/min for the respective protein concentrations. The individual protein concentrations' rates (µmol/min) were compiled and plotted against their respective enzyme mass in mg to yield a linear plot. The linear regression slope represents the "pseudo"-specific activity of the enzyme in µmol/min/mg. The analysis was performed in triplicate, and the displayed plots depict the averaged result. The difference between the replicates was encapsulated using error bars based on the data set's standard deviation of the means.

5.3.2. Mant-ATP association kinetics through stopped-flow

A stopped-flow technique was employed to determine the association rate constants and dissociation rate constants of ATP to *Kp*NNAT and *Ef*NNAT. This method rapidly mixed a solution of Mant-ATP and the respective NNAT enzyme. The rate of association was then determined by measuring the increase in fluorescence at wavelengths higher than 400 nm using an Applied Photophysics stopped-flow fluorometer (Applied Photophysics Inc., USA). This technique allowed for precise monitoring and analysis of the kinetics of the interaction between Mant-ATP and the NNAT enzymes. It has been previously demonstrated by Jeje, *et al.,* (2022) that there is a sufficient signal change for these proteins; thereby, Mant-ATP fluorescence spectroscopy was not deemed necessary. The rate constants were determined as depicted by Patel, *et al.*, (2014) whereby maintaining pseudo-first-order kinetics, a protein dilution series was prepared with a starting concentration of 5 µM, in conjugation with a Mant-ATP serial dilution maintaining a 5-fold excess of Mant-ATP for each respective protein concentration. The samples were prepared within 10 mM Tris-HCl, pH 7.5, supplemented with 1 mM DTT.

The samples were prepared under three conditions where the buffers were further supplemented with i) in the absence of divalent metal ions, ii) in the presence of 5 mM $MgCl_2$, and iii) in the presence of 5 mM $CaCl_2$. The stopped-flow injection setup was constructed as depicted in Figure 5.1.

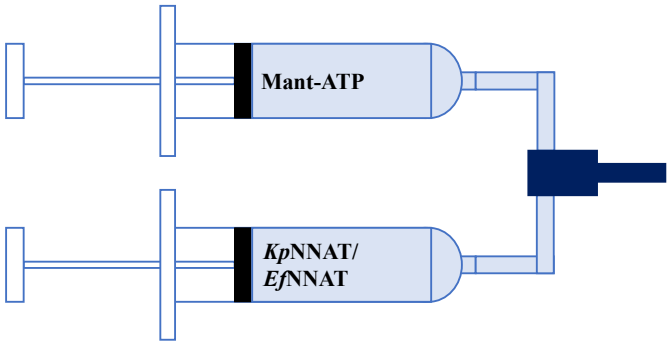

Figure 5.1 Stopped-flow setup. Solutions of Mant-ATP were rapidly mixed with solutions of *Kp*NNAT or *Ef*NNAT in 1:1 ratio. Whereby, the theoretical start of the association event was measured.

The measurement was set for the first 0.1 seconds of the reaction, with wavelength bandwidth set at 2.5 mm. Mant-ATP was excited at 365 nm, and the increase in fluorescence was measured using a greater than 400 nm longpass fluorescent filter. The data were fitted to a single exponential using the ProDataViewer software (Applied Photophysics Inc., USA), and the observed rate constants (k_{obs}) were recorded. The k_{obs} represent a convolution of the k_1 and k_{-1} of Mant-ATP; thereby, the increasing k_{obs} with the increasing Mant-ATP concentrations were plotted to a linear curve, representing $k_{obs}=k_1[Mant\text{-}ATP]+k_{-1}$. Thereby both the k_1 ($M^{-1}.sec^{-1}$) and the k_{-1} (sec^{-1}) were extrapolated from the linear regression plots generated by Microsoft Excel (Microsoft Corporation, USA). Subsequently, the Mant-ATP disassociation constant (k_d) was calculated as $k_d = k_1/k_{-1}$ in molar (M), as described by Corzo. The statistical significance of the differences in averaged *kd* was tested through a students T-test with a significance level of 0.05. The analysis was performed in triplicate, and the displayed plots depict the averaged result. The difference between the replicates was encapsulated using error bars based on the data set's standard deviation of the means.

5.4. Results

There is a clear understanding that ATP requires the presence of divalent metal ions to be an active biological compound. However, the function of the divalent metal ion may vary on a case-by-case basis. ATP binding is a challenge, primarily because it is a highly charged molecule. Hence, divalent metal ions are known to mediate and stabilise ATP binding by acting

in a compensatory role. Thereby, when investigating an ATPase such as these NNATs, it is imperative to establish the kinetic influence of the divalent metal ions as they play a fundamental role within the catalytic capability of the enzyme. In this instance, the kinetic influence of the divalent metal ions Mg^{2+} and Ca^{2+} were determined for *Kp*NNAT and *Ef*NNAT, as depicted below, using an ADH-coupled enzyme activity assay. Whereby ADH's ability to catalyse the formation of NADH from the NNAT product NAD^+ was tested at increasing NNAT concentrations.

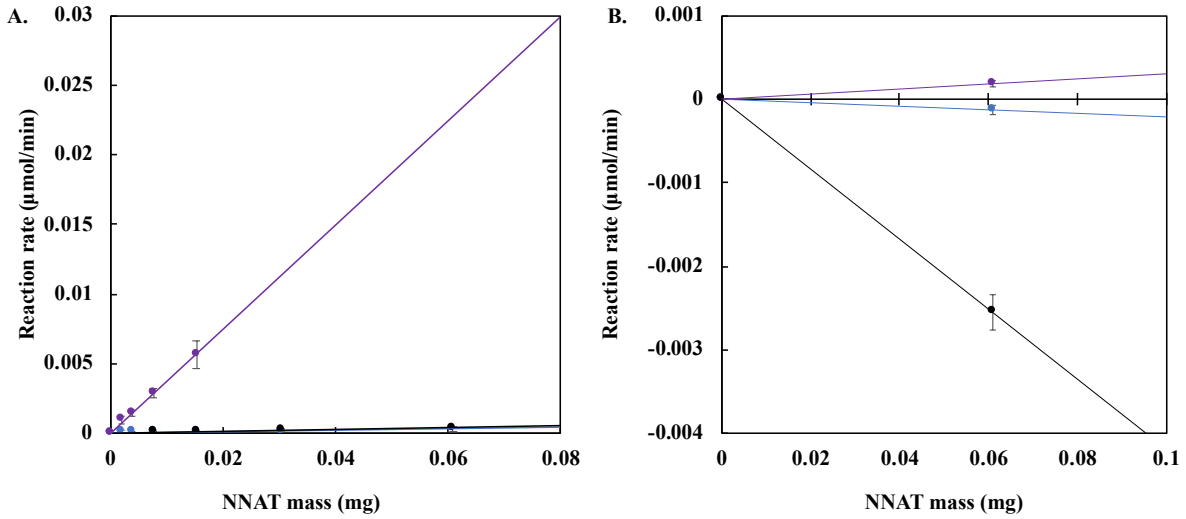

Figure 5.2 "Pseudo"-specific activity of *Kp*NNAT and *Ef*NNAT in the presence/ absence of 5 mM $MgCl_2$ and $CaCl_2$, and 1 mM ATP. The activity of *Kp*NNAT (A) was assessed in the absence of divalent metal ions (blue), with 5 mM $MgCl_2$ (purple), and with 5 mM $CaCl_2$ (black). Only in the presence of 5 mM $MgCl_2$ did *Kp*NNAT exhibit activity (0.374 µmol/min/mg). The activities observed in the absence and presence of 5 mM $CaCl_2$ were negligible (0.0052 µmol/min/mg and 0.0063 µmol/min/mg, respectively). The activity of *Ef*NNAT (B) was evaluated without any divalent metal ions (blue), with 5 mM $MgCl_2$ (purple), and with 5 mM $CaCl_2$ (black). No discernible signal or activity was observed under any conditions, primarily due to buffer noise. Consequently, no definitive conclusions could be drawn from the available data.

*Kp*NNAT displayed explicit activity in the presence of 5 mM $MgCl_2$, owing to a "pseudo"-specific activity of 0.374 µmol/min/mg (Figure 5.2). However, negligible activity was observed without a divalent metal ion or in the presence of 5 mM $CaCl_2$. These activity levels were anticipated as Mg^{2+} is the primary required divalent metal ion, as seen within other NNAT species. There was no or negligible activity for *Ef*NNAT under any conditions. The reason behind this lack of activity is unclear. Even if alternative substrate selectivity (i.e., NaMN) were suspected, *Ef*NNAT would still be expected to exhibit some level of activity using the NMN substrate. This is plausible since Gram-positive bacterial NNATs are primarily

associated with NaMN preference. However, this preference has only commented on the enzyme's efficiencies relating to the specific substrates, not indicating "one or the other".

The presented data not only suggested substrate selectivity but also raised hypotheses concerning *Ef*NNAT's inactivity. Previous chapters discussed limited interactions between *Ef*NNAT and ATP, although these interactions were not explicitly confirmed. These findings introduce complexity to understanding *Ef*NNAT's enzymatic activity. To further investigate the cause of inactivity, direct testing of ATP association was conducted using stopped-flow association studies. Mant-ATP was utilised to examine ATP binding kinetics to *Kp*NNAT and *Ef*NNAT. The association and dissociation rate constants of Mant-ATP to both NNAT species were determined. These rate constants define the ATP-NNAT complex formation and decomposition timeline, providing insights into complex stability and ligand affinity. A revised procedure, based on the one presented by Patel *et al*., (2014) was followed to determine k_1 and k_{-1} of Mant-ATP to both NNAT species in the presence of divalent metal ions Mg^{2+} and Ca^{2+}.

As previously stated, Figure 5.2 showed little activity for *Ef*NNAT, regardless of the present divalent metal ion, potentially suggesting alternate substrate selectivity. However, small-scale activity is still anticipated as the substrate selectivity is typically regarded as a range especially considering the NMN/NaMN substrates. In this regard, Figure 5.3 confirmed *Ef*NNAT*'s* incapability to conjugate ATP to NMN, as little to no ATP binding was detected. The detected signal was indistinguishable from buffer noise and, therefore, highly suggestive of limited ATP binding. The underlying reasons for the reduced ability of *Ef*NNAT to bind to Mant-ATP are not currently well understood. Here, the presence of the Mant group could interfere with the binding event in *Ef*NNAT. However, in Chapter 4, apparent interactions between ATP and *Ef*NNAT were less influential than initially thought. These observations were subject to the limitation of the techniques, only providing qualitative confirmations of an interaction. Here, in Figure 5.2, it is clear that *Ef*NNAT's ability to bind to ATP is weaker than anticipated. Thereby, given the trend was observed previously, it seems unlikely that the Mant group is involved in the reduced ATP binding capability. Instead, it was hypothesised that this could result from interference from the $(his)_6$-tag. This interference, however, required more direct testing to confirm. Unfortunately, due to constraints in time and funding, these tests were not feasible. Consequently, this became an unfortunate endpoint for *Ef*NNAT, as additional studies could not be pursued at that time.

Remarkably, there was a stark contrast in the lack of Mant-ATP association between *Ef*NNAT and *Kp*NNAT. Mant-ATP displayed the capability of binding to *Kp*NNAT, regardless of the present metal ion (Figure 5.3). This observation was interesting as the divalent metal ion was assumed to influence the ATP binding and later stabilising events. The association was apparent with the k_1 of 5.99 $M^{-1}.sec^{-1}$ in the absence of a divalent metal ion (Figure 5.3). In this regard, no pattern was evident on whether the divalent metal ions influenced the direct binding event, as seen through the k_1 of 5.72 $M^{-1}.sec^{-1}$ and 5.95 $M^{-1}.sec^{-1}$ for binding within the presence of Mg^{2+} and Ca^{2+}, respectively. However, the divalent metal ions increased the k_{-1}, indicating a shorter timeframe for which the Mant-ATP remained complexed to *Kp*NNAT.

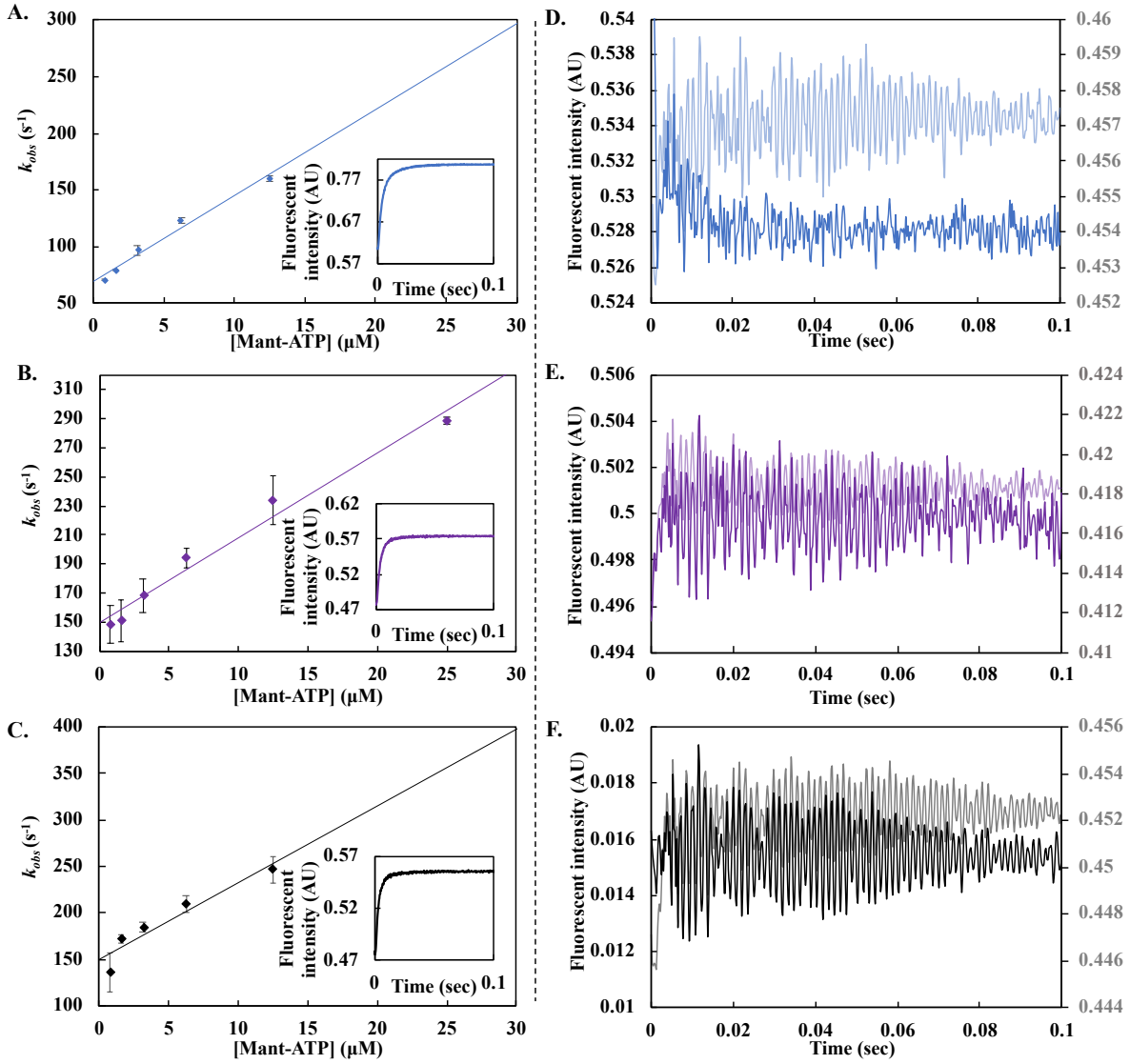

Figure 5.3 Mant-ATP association to *Kp*NNAT and Mant-ATP binding to *Ef*NNAT. Panels A-C display the deconvolution of Mant-ATP k_{obs} to *Kp*NNAT under different conditions, with insets showing the corresponding Mant-ATP binding plots. In panel A (blue), the linear deconvolution in the absence of any metal ions reveals a k_1 of ~6 $M^{-1}.sec^{-1}$ and a k_{-1} of ~80 sec^{-1}. Panel B (purple) represents the linear

deconvolution in the presence of 5 mM $MgCl_2$, showing a k_1 of ~6 $M^{-1}.sec^{-1}$ and a k_{-1} of ~150 sec^{-1}. Panel C (black) shows the linear deconvolution in the presence of 5 mM $CaCl_2$, with a k_1 of ~6 $M^{-1}.sec^{-1}$ and a k_{-1} of ~160 sec^{-1}. In panels A-C, Mant-ATP associates with *Kp*NNAT regardless of the presence of a metal ion, although the metal ion influences the binding speed and stability. Panels D-F present the Mant-ATP binding to *Ef*NNAT under various conditions. In panel D (blue), it shows 0.78 µM (darker blue) and 12.5 µM (lighter blue) Mant-ATP binding to *Ef*NNAT in the absence of any divalent metal ion. Panel E (purple) represents 0.78 µM (darker purple) and 12.5 µM (lighter purple) Mant-ATP binding to *Ef*NNAT in the presence of 5 mM $MgCl_2$. Panel F (black) displays 0.78 µM (darker black) and 12.5 µM (lighter black) Mant-ATP binding to *Ef*NNAT in the presence of 5 mM $CaCl_2$. Panels D-F demonstrate negligible binding between Mant-ATP and *Ef*NNAT, even with a drastic increase in Mant-ATP concentration.

The shorter complexed time observed in the presence of divalent metal ions was an intriguing observation. It challenged the notion that the stabilisation of ATP association would be visualised through prolonged complex maintenance. Clearly, this was not the case. Thereby, to help further understand the complex stability and the influence of the divalent metal ions, the k_d of the respective complexes were calculated and displayed in Table 5.1.

Table 5.1 k_d values of Mant-ATP for *Kp*NNAT in the presence and absence of divalent metal

Conditions	k_1 ($\mu M^{-1}.sec^{-1}$)	k_{-1} (sec^{-1})	k_d (µM)
No metal ion	5.99 ± 1.38	79.48 ± 1.65	13.65 ± 2.56
5 mM $MgCl_2$	5.72 ± 0.71	149.57 ± 10.44	26.62 ± 5.50
5 mM $CaCl_2$	5.95 ± 0.69	159.99 ± 5.08	29.50 ± 5.00

Table 5.1 displays the calculated k_d values in M for *Kp*NNAT with the following conditions: the absence of divalent metal ions, 5 mM $MgCl_2$, and 5 mM $CaCl_2$. The presence of the divalent metal ions reduced the complex stability, as a greater than two-fold increase in the *kd* was observed in the presence of divalent metal ions compared to the absence of a divalent metal ion ($p < 0.05$ t-test).

As previously stated, Mant-ATP could bind to *Kp*NNAT with or without a divalent metal ion. Table 5.1, however, confirms that the presence of a divalent metal ion impacts the stability of the complex. The divalent metal ions are not crucial for the initial binding event as the k_1 across all conditions was comparable. This suggests that the divalent metal ions have a limited effect on the direct association of Mant-ATP. However, the rate of complex decomposition, as indicated by the k_{-1} values, was influenced by the presence of the metal ions. An approximately two-fold increase in the k_{-1} led to a similar trend in the dissociation rate constant (k_d). Comparing the absence of a divalent metal ion (control) to the presence of 5 mM $MgCl_2$, the increased k_d may reflect enzymatic control, where the more rapid dissociation enables the

forward motion of the interaction, allowing for rapid ligand turnover. Similar k_d values were reported in the presence of 5 mM $CaCl_2$. These observations were to be expected as these metal ions should facilitate similar compensation interactions, allowing the charge mitigation of the phosphate tail of the ATP. In Chapter 4, it was concluded that both $MgCl_2$ and $CaCl_2$ resulted in similar ATP binding conformations, although slight differences were observed in terms of tertiary structural changes.

These structural changes suggest that $MgCl_2$ enables the binding conformation that supports enzymatic activity, while $CaCl_2$ enables ATP binding but may not facilitate ATP hydrolysis. Thus, the metal ions play a role in facilitating charge compensation during the ATP binding event. However, they also induce different conformations of ATP, influencing its propensity for hydrolysis and its continuation within the NNAT reaction.

The presence of the divalent metal ions seems to enable compensatory interactions that drive the maintenance of the ATP-NNAT complexes as it is to i) enable the appropriate ATP binding conformation and ii) regulate substrate turnover by decreasing the amount of time spent in the active site of the NNAT enzyme. There is merit to this observation as the retention of two highly charged molecules seems unlikely especially considering that the inclusion of the divalent metal ions increases the flexible range of motion of both the NNAT enzyme and the ATP ligand. Unfortunately, these are mere assumptions made on the structural occurrences based on the presented kinetic data, and it is these systems that were further simulated to provide evidence of such conformational changes to the enzyme and substrate structures.

5.5. Discussion

With many ATPases, understanding the ATP binding event is incredibly important to grasp the enzymes' capability and reactivity. NNAT is no exception to this. As previously established, NNAT conjugates an AMP (from ATP) to NMN to produce NAD^+. This reaction results from the initial hydrolysis of the α-β phosphate bond of the ATP molecule (Magni et al., 2004; Zhang et al., 2003). In this enzyme reaction, the initial coordination of the substrates is of paramount importance to enable the evolution of the reaction. Both substrates are subject to multiple forms of stabilisation that ultimately coordinate their binding in their respective active site positions within the central hydrophobic cleft (D'Angelo et al., 2000; Huang et al., 2010; Jeje et al., 2022; Saridakis and Pai, 2003; Sershon et al., 2009; Yoon et al., 2005; Zhang et al., 2003). Briefly,

the theoretical interaction/ coordination of the ATP substrate is facilitated to achieve the correct spatial and conformational coordination. This theoretical model was constructed from related crystal structures, but as *Kp*NNAT has no available crystal structure, this model is purely theoretical. See the coordination in Figure 5.4.

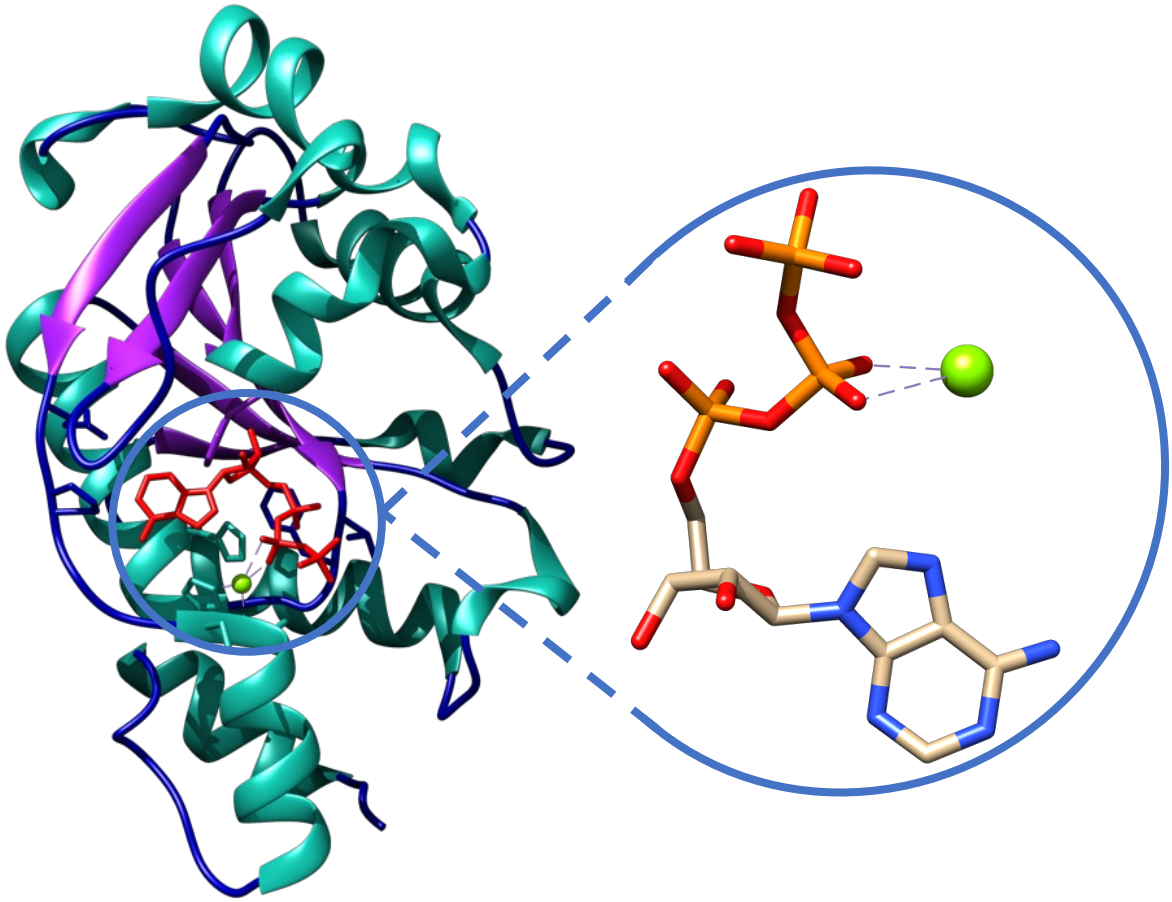

Figure 5.4 ATP coordination within *Pa*NNAT (PDB ID: 1YUN). The above depicts the spatial coordination of ATP within the central hydrophobic cleft (to the left) and the conformational coordination of the ATP molecule within the binding site (to the right). The figure visualises the highly bent conformation of the ATP driven by the Mg^{2+} (green).

As depicted in Figure 5.4, ATP coordination aims to facilitate two objectives i) the spatial coordination of the ATP molecule within the binding cleft and ii) the conformational coordination of the ATP molecule, being the bent conformation. Three critical structural and chemical factors help facilitate these steps. Firstly, essential conserved residues (namely, (H/T)XGH and SXXXXR) impose a positive dipole within the ATP binding pocket, establishing an optimised binding region that allows the binding of highly negatively charged molecules (D'Angelo et al., 2000; Jeje et al., 2022; Sershon et al., 2009; Yoon et al., 2005; Zhang et al., 2002). Secondly, several residues, including the conserved sequences, form direct

interactions with the adenine nucleoside and several phosphates of the triphosphate tail, recognising the ATP substrate and enabling sufficient contact (Sershon et al., 2009). These instances coordinate the initial ATP binding event and are assumed to play a role in ATP positioning. Thirdly, the divalent metal ions introduce charge mitigation (as previously discussed) and allow for the formation of a bent conformation at the α-β phosphates (Figure 5.4). This bent conformation physically strains the α-β bonds, which is a suggested requirement for ATP hydrolysis (D'Angelo et al., 2000; Magni et al., 2004; Sershon et al., 2009). With these defining steps relating to the ATP binding event, the previous observations have clear theoretical backing.

We can relate several previous observations to this theoretical binding mechanism with the abovementioned fundamental binding principles. Here, *Kp*NNAT can interact with ATP regardless of the presence or absence of a divalent metal ion. Zhang *et al.* (2003) confirmed this possibility with a crystal structure depicting h-NNAT complexed with an ATP analogue without a divalent metal ion. The presence of the divalent metal ion is not required for charge mitigation and stabilisation of the initial ATP binding. This phenomenon is consistent with the theoretical binding mechanism, as it proposes that the conserved regions are responsible for the initial recognition and spatial coordination of the ATP molecule.

Although divalent metal ions may not be directly involved in the initial binding event, evidence suggests their role in the prolonged stabilisation of the NNAT-ATP complex. Initially, this stabilisation was believed to result in an extended duration of ATP complexed to NNAT. However, further research has revealed that the divalent metal ions are also hypothesised to play a role in the local alignment of the ATP molecule as a whole, thereby maintaining the necessary conditions for ATP hydrolysis (D'Angelo et al., 2000; Magni et al., 2004; Zhang et al., 2003). Surprisingly, the data indicated that divalent metal ions actually reduce the time spent in the ATP-NNAT complex. This phenomenon was visualised by the increased k_d values, which nearly doubled in the presence of the divalent metal ions. Limited data were available to support these values, but they seem to agree with what is currently represented in the literature. As the k_d values agree with the ITC data presented by Daya, *et al.,* (2022); being the k_d calculation of the ATP-*Kp*NNAT complex in the presence of Mg^{2+}. Both of these k_d values are within reasonable agreement with what has been presented through ITC in Sershon, *et al*., (2009). Notably, Sershon, *et al*., (2009) reported multiple k_d values for *Ba*NNAT, a trimer, including an initial k_d that was twice as high as the one reported here

and by Daya, *et al*., (2022). These differences were acceptable as they pertained to alternate NNAT species and could be further explained by the inclusion of the Mant group. The Mant group is known to influence the kinetic parameters due to binding interferences but still maintains similar trends (Ni et al., 2000).

However, these values, while consistent with previous reports in the literature, demonstrate a trend opposite to what was initially anticipated. Unfortunately, limited information is available regarding the influence of divalent metal ions in this context. Only Jeje, *et al.,* (2022) have conducted a study that sheds light on the stability and kinetic effects of divalent metal ions. Through thermal shift assays, they confirmed that the presence of divalent metal ions does not improve the structural stability of the *Kp*NNAT-ATP complex. Surprisingly, the coexistence of ATP and divalent metal ions increases the structural flexibility and reactivity of *Kp*NNAT towards ATP (Jeje et al., 2022).

These results do not necessarily directly contradict what was initially thought but instead offer an alternative perspective. The inclusion of $MgCl_2$ within an ATPase system could increase the k_d without negatively impacting the enzyme's activity (Saylor et al., 1998). Saylor, *et al.*; for instance, display that within this concentration range (0.2 – 5 mM $MgCl_2$), the metal ion concentration is sufficient for the phosphoryl transfer event, whereby the $MgCl_2$ acts within a high activator capacity. This phenomenon corresponded with an increased k_d and a decreased k_a, illustrating a negative synergism within the binding event (Covy and Giasson, 2010; Saylor et al., 1998).

With the increased k_d, an alternative regulatory mechanism may be present, suggesting a strenuous binding event due to the strict conformational requirements for ATP hydrolysis. The k_d reflects the equilibrium between the free ligand and the complexed ligand, providing insights into its propensity for forming complexes. Moreover, ATP is not typically found freely floating in the cell; it immediately interacts with available divalent metal ions, forming Mg^{2+}-ATP and Ca^{2+}-ATP complexes (Yamanaka et al., 2016). These complexes are larger and more reactive than the native states. The increased reactivity may enable the ATP molecule to sample strenuous conformations, such as a bent conformation, allowing the reaction to proceed. However, as a consequence, the combined influence of these interactions reduces the overall stability of the complex.

The results presented above display similar kinetic and structural implications relating to the presence of $MgCl_2$ compared to that of $CaCl_2$. Considering their similar chemical properties and functionalities within the *in vivo* system, they are expected to yield a similar structural impact should they interact with *Kp*NNAT. However, $CaCl_2$ yielded no detectable activity, as presented in Figure 5.2. Thereby comparing it with the presence of $MgCl_2$, both present similar interactive properties, as they have similar chemistries and similar k_d values, but only one allows NNAT activity. This phenomenon enables the postulation that the kinetic effect is only plausible due to the chemical nature of specific divalent metal ions. Even though ATP can bind without a divalent metal ion, only specific ions can allow for the correct ATP conformation that favours the hydrolysis of the α-β phosphate bond (Chapter 4). Seeing as both $MgCl_2$ and $CaCl_2$ seem to offer similar structural implications, $CaCl_2$ does not convey the chemical properties to allow the correct conformational positioning of the ATP for its hydrolysis. Alternatively, $MgCl_2$ allows for enzyme activity with an increased k_d, potentially illustrating more rapid substrate turnover. Unfortunately, these suggestions question the reaction structure; this cannot be visualised through these kinetic assays alone and require more specific analysis. Thereby, similar conditions to those presented above were simulated within a cumulative simulation of 1 μsec, which is reported in Chapter 6.

Unfortunately, the data presented for *Ef*NNAT illustrated contradicting conclusions, suggesting the inactivity presented through *Ef*NNAT is related to its reduced ability to bind ATP. It is worth noting that the current limitation of the study does not consider the NMN substrate or its alternative NaMN. The literature strongly implies that Gram-positive bacteria based NNATs have a predominant preference for NaMN (Sershon et al., 2009). Thereby, the inactivity may be routed within several concepts i), *Ef*NNAT has a stronger preference for NaMN rather than NMN, or ii) the reduced binding of ATP, as presented in the above figures, prevented sufficient hydrolysis of the molecule, thereby not enabling the reaction to continue. For the former, alternative substrate preference seems a sufficient explanation. However, the selectivity of the pyridine nucleotide is implied to be a matter of higher affinity for the one, instead of a one or the other-based ideology (Magni et al., 2004). Thereby, given the lack of enzyme activity in its entirety suggests the inability of the reaction to continue. This phenomenon seems more fitting to the reduced binding of ATP. If ATP binding is restricted, the reaction will not continue. This explanation, however, raises more questions than answers, with the most apparent unknown being why an ATPase is incapable of interacting with ATP to

a sufficient degree. The presented evidence is, unfortunately, insufficient to provide a clear explanation as to why *Ef*NNAT is incapable of binding ATP.

Currently, this seems to be routed within unforeseen consequences within vector design as brief computational predictions suggest that the $(his)_6$-tag might have interfered with the structure of the (H/T)XGH binding site by introducing increased flexibility in that region. As presented on several levels, the (H/T)XGH site is a critical determinant of the ATP binding event, with single point mutations causing severely diminished ATP binding ability (Sershon et al., 2009; Magni et al., 2004). Thereby, given the increased structural fluctuations introduced by the $(his)_6$-tag, it may have impacted the functional capability of this site, impairing its ability to bind ATP. It is worth noting that the observation of such effects is not uncommon when using affinity tags like $(his)_6$-tags, which are generally effective in isolating various proteins. It is crucial to take into account that the incorporation of a small affinity tag has the potential to impact the behaviour of the protein to which it is attached. While these observations provide valuable insights, the specific mechanism underlying the interference caused by the $(his)_6$-tag remains speculative at this stage. To fully understand the mechanics behind the inactivity of *Ef*NNAT and confirm the impact of the $(his)_6$-tag, further direct investigations are needed. As stated previously, direct testing in this regard was unlikely due to the high costs of the alternative NaMN substrate; further, due to time constraints, this was not further investigated. Unfortunately, given the lack of valuable empirical data, it was thought to exclude *Ef*NNAT from further computational modelling, as the core justifications used for the computational models were derived from the previously presented empirical data.

In conclusion*, Kp*NNAT could interact with ATP in a rapid association event, regardless of the present metal ion. However, the metal ions dictate the kinetic capability of the enzyme. Only specific metal ions offer the appropriate conformational positioning of the ATP to allow its hydrolysis. Unfortunately, these required conformations seem to reduce complex stability, but this can be a potential mechanism to improve substrate turnover. In its totality, the metal ions do not dictate whether or not ATP will bind to *Kp*NNAT. However, the unique chemistries related to these co-factors suggest enzyme activity. Though the exact mechanism to describe this is unclear, MD simulations may offer further insight, as demonstrated in the next chapter (Chapter 6).

6. Chapter six
ATP binding a computational analysis

6.1. Introduction

Computational modelling has increasingly emerged as a valuable approach for investigating and elucidating specific concepts that may be challenging to explore using physical experimental procedures. While physical experiments have inherent limitations regarding sensitivity and applicability, computational modelling offers the advantage of overcoming these constraints. In this regard, computational modelling offers a direct microscopic view at the nanometre scale, providing a wealth of knowledge, especially within the biochemical field. It provides theoretical predictions of molecular behaviour and dynamics, provided the necessary data is available to corroborate these observations within the physical world. This is precisely why combining well-validated computational models with extensively tested systems holds great potential for explaining numerous phenomena that would typically necessitate multiple crystal structures to obtain sufficient evidence. Due to this, computational models have become more mainstream, especially when validated with experimental data.

Considering the promising data obtained for *Kp*NNAT in previous chapters, using computational models has proven invaluable. In this context, similar approaches have been explored by Jeje, *et al*., (2022) who simulated comparable conditions involving *Kp*NNAT and its binding to ATP. The information presented herein was incredibly valuable and fundamental to a lot of the previous conclusions seen within the previous chapters. However, this study has limitations: i) the lack of an available crystal structure for *Kp*NNAT, ii) the lack of direct contact between the divalent metal ion co-factors and the ATP substrate, and iii) the requirement for longer simulation periods. Given these limitations, technological advancements have opened up new possibilities for extending relevant system simulations. Developments in simulation software, for instance, now allow the inclusion of divalent metal ions, providing alternatives to relying solely on available crystal structures. Additionally, these technological advancements enable the sustained simulation of longer periods, facilitating more comprehensive investigations.

Within these advances, the most fundamental addition is the incorporation of artificial intelligence, allowing the accurate prediction of the protein structure. Here, Rosetta Fold offers sufficient accuracy and hierarchical considerations to the protein structures to offer a distinct

advantage towards simple homology models. To briefly state the workflow presented later in this chapter, the most fundamental concept introduced is that multiple validation and verification steps followed each step to ensure the most accurate predictions possible.

Herewith, the structure of *Kp*NNAT was predicted using the online server Rosetta Fold and metal ions were introduced with the use of multiple reference structures. The final structure was validated through multiple structural alignments and structure validation software such as MolProbity. Among these, the most fundamental quantifiable standards were the root mean square deviations (RMSD), detailing the atomistic difference between two structures in Armstrong (Å). The validated structures were subjected to IFD to define the interaction between *Kp*NNAT and ATP, considering a flexible ligand and flexible receptor. The resulting models were again subjected to multiple structural alignments, using the global (complete complex structure) and local (local ATP binding environment) RMSD as the validating parameters. Upon confirmation of sufficient model quality, the docked structures were used within five 200 nsec replicate MD simulations culminating in 1 µsec. This section will discuss the methods as briefly outlined above, further relating the final MD simulations to the previous chapters defining the ATP binding event within *Kp*NNAT.

6.2. Materials

The *in-silico* models and simulations were generated using high-end desktop servers ((16 CPU Intel® core i7TM, 3.3 GHz, 20 M cache), MSI X99 motherboard with 32 GB DDR4-2133 MHz memory and 264 GB RAM, Nvidia GTX 750Ti graphics card, Schrödinger Maestro v12.2, and Linux server (2019 GPU-enabled Schrödinger Desmond) (Council for Scientific and Industrial Research, Cape Town, South Africa).

6.3. Methods

6.3.1. Rosetta fold based structure prediction, modelling and validation

Currently, the largest issue facing the investigation into *Kp*NNAT is the consideration that there is no solved crystal structure of the protein. Though several evolutionary homologs exist, the sequence identity is not ideal. Thereby, alternative methods were considered to mitigate the potential error that would be introduced upon using the evolutionary homologs for homology modelling. Fortunately, recent advances within the protein structure prediction front have

enabled several tools to side-step this issue and provide variability within the approaches. The recent publication and release of the algorithm routed in artificial intelligence, namely Rosetta Fold, has enabled the prediction of the structure of *Kp*NNAT. Rosetta Fold employs a three-track neural network that integrates the one-dimensional protein sequence, two-dimensional distance predictions for molecule interactions, and the potential three-dimensional architecture. This comprehensive approach allows Rosetta Fold to reason and accurately predict the folded structure by considering the hierarchical relationships among these factors. Given the novelty of the approach and the recent successes of Rosetta Fold (due to its publication), it was used to predict the folded three-dimensional structure of *Kp*NNAT. Whereby the *Kp*NNAT amino acid sequence was uploaded to the Rosetta Fold online server along with a multiple sequence alignment based on 5 orthologs of *Kp*NNAT (Baek et al., 2021). For reference, to annotate the orthologs used as well as to visualise their relationship, a phylogenetic tree was constructed (Figure 6.1)

Given the novelty of the technique, extra precautions were taken to validate the resulting structure. Whereby the top-modelled structure was chosen based on the lowest error predictor. The resulting model was analysed on two levels, i) structure validity based on previously established NNAT structures, and ii) structure quality routed in the bonding architecture and fold structure. The primary validation methodology compared the predicted model to the closest evolutionary homolog with a solved crystal structure, being *Ec*NNAT (PDB ID: 1K4K). *Ec*NNAT shares approximately 75 % sequence identity with *Kp*NNAT. A second reference structure was used; a homology model as presented in Jeje, *et al.*, (2022) which was modelled according to *Ec*NNAT. These comparisons were done to confirm that the predicted structure has some theoretical merit by comparing it to *Ec*NNAT as well as establishing that the predicted model, at the very least, is comparable to the previously utilised homology model. Thereby, specific considerations were made, namely, i) global RMSD-based comparison should not differ by more than 2.5 Å, and ii) specific conserved sites should have structural similarity. Thereby, in its totality, confirming that the predicted model of *Kp*NNAT is of sufficient theoretical validity to continue with further computational modelling.

Fortunately, protein structure quality assessment follows a predefined and streamlined process. To ensure the quality of our protein structure, we relied on the widely used online resource, MolProbity. MolProbity is a software tool specifically designed for evaluating protein structure quality. It incorporates multiple assessments, including bonding architecture, theoretical

outliers, and other factors crucial to structure validation. These assessments are summarised through the Clashscore, Ramachandran and rotamer analyses and ultimately combined into a MolProbity score, which provides an overall measure of structural quality.

The Clashscore is a metric utilised to identify steric clashes within the model, while the Ramachandran and rotamer analyses assess the conformational preferences of amino acid side chains. The MolProbity score, on the other hand, offers a composite evaluation of the overall structure quality. Optimal scoring is typically achieved when the structure quality falls within the 98th percentile or higher. Structures within these percentiles demonstrate a strong alignment with other crystal structures of similar resolution, indicating their reliability and accuracy.

To confirm the quality of the predicted *Kp*NNAT model, it was submitted to MolProbity for structural assessment. The results of this assessment confirmed that the predicted model of *Kp*NNAT exhibited satisfactory quality, thereby enabling its use for subsequent computational modelling with confidence.

6.3.2. ATP preparation for induced-fit molecular docking

The 3D structure of ATP was acquired from PubChem (CID: 5461108) and then subjected to the LigPrep tool in Maestro (Schrödinger Maestro v12.2) in the SDF file format. LigPrep, available within Maestro, facilitates the following steps to generate an accurate 3D representation of ATP.

LigPrep prepared and minimised the ATP structure using the OPLS_2005 force field, considering ionisation at pH 7.0 ± 2.0 through the Epik algorithm. Epik specialises in accurately determining a given small molecule's most probable ionisation and tautomeric forms under specific conditions. Subsequently, the structure underwent desalting, and the tautomeric states were predicted.

The chiralities were determined based on the optimised three-dimensional structure to compute stereoisomers. The best-optimised structure was selected based on factors such as the molecule score, ionisation, and Epik state penalties. The molecule score represents the energy associated with the current conformation, with lower scores being more favourable. Similarly, lower Epik

state penalties indicate more energetically favourable ionisation states. The resulting best-scoring molecule was again saved in the SDF file format for further use and analysis.

6.3.3. *Kp*NNAT preparation for induced-fit molecular docking

As the predicted model of *Kp*NNAT contained no divalent metal ions. Here, Mg^{2+} and Ca^{2+} ions were incorporated into the model structure, using several solved crystal structures as reference (PDB ID: 1YUN, 3E27 and 1KQN). This step generated the *Kp*NNAT-Mg^{2+} complex and the *Kp*NNAT-Ca^{2+} complex. The validity of these structures was determined by conducting structural comparisons, which were quantified using global RMSDs. RMSD values greater than 2.5 Å indicated a disagreement with the reference structures.

The resultant structures were submitted to the Protein preparation wizard within Maestro (Schrödinger Maestro v12.2) for structural refinement and optimisation. This multi-step process aimed to enhance the quality and accuracy of the structures. It involved incorporating zero-order bonds related to the metal ions and introducing potential disulfide bonds. Epik ionisation was applied to the global protein structure at pH 7.0 ± 2.0, considering state penalties and corrections. The optimisation also included optimising hydrogen bonding assignments and ionising ionisable protein groups using the PROPKA algorithm at pH 7.0 to ensure an optimised hydrogen bonding network. Finally, restrained minimisation was performed using the OPLS_2005 force field. Briefly, restrained minimisation restricts the movement of specific atoms or groups, enabling a controlled optimisation process of the molecule's three-dimensional structure.

Overall, these steps were undertaken to refine and optimise the structures of the *Kp*NNAT-Mg^{2+} and *Kp*NNAT-Ca^{2+} complexes, incorporating necessary modifications and applying computational techniques to improve their quality and accuracy.

6.3.4. Defining the conserved ATP binding domains through multiple sequence alignment

To establish the relative search area for the IFD (Induced Fit Docking) procedures, the ATP binding region was identified by performing a multiple protein sequence alignment using the Clustal Omega online tool. Here, the NNAT sequence was aligned to several species to define the amino acids relating to the ATP binding event. As previously established, several factors facilitate and stabilise the ATP binding event. Two key binding motifs, the conserved (H/T)XGH and SXXXXR motifs, play crucial roles in the initial recognition and spatial

coordination. These motifs were identified due to their conservation across all NNAT species, which is attributed to the presence of the conserved nucleotide binding Rossmann fold observed in all NNAT structures.

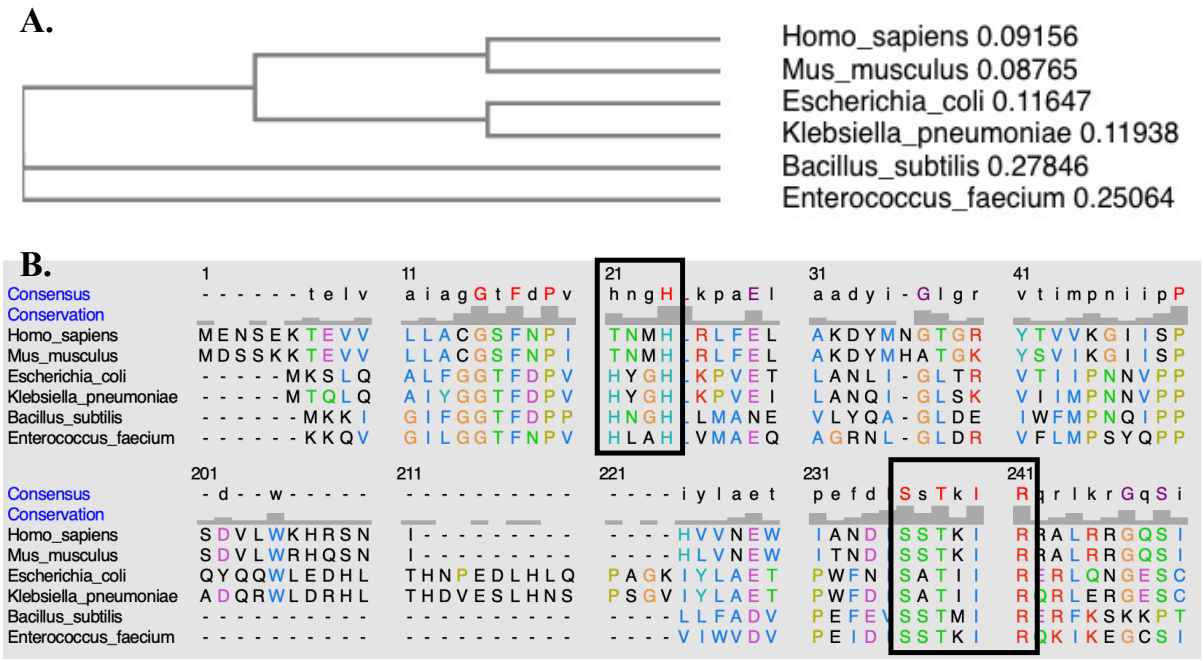

Figure 6.1 Multiple sequence alignment of NNAT orthologs. A.) The figure above depicts the phylogenetic tree of six NNAT orthologs. The orthologs are named according to their species. B.) This panel illustrates the MSA of several NNAT species, labelled by their species name. Panel B further illustrates from top to bottom, the (H/T)XGH conserved motif and the SXXXXR conserved motif.

6.3.5. Induced-fit molecular docking of ATP to *Kp*NNAT, and structure validation

Upon the confirmation of structure validity and quality, and the definition of the ATP binding motifs, the prepared ATP and *Kp*NNAT models were submitted for IFD. Briefly, IFD follows the initial Glide based molecular docking of a flexible ligand (in this case ATP) to a rigid receptor (in this case *Kp*NNAT); the revolving structure around the ligand is refined through Prime in an attempt to emulate the structural changes that result from ligand binding as per the induced-fit model, whereby the ligand is deleted and redocked into the modified structure. This step utilised an extended sampling methodology, where over 40 poses were generated for each condition. Whereby the conserved binding motifs, as previously discussed, were highlighted as the centre of the receptor grid, with a specific focus on the (H/T)XXH and SXXXXR sequences.

The initial docking event comprised several constraints, with the primary constraint defining the metal ion binding regions. The initial docking procedure considered the ATP molecule as flexible, defining the sample ring conformations with an energy window of 113 kJ/ mol, where nonplanar conformations were penalised. Consequently, the Glide docking procedure used van der Waals scaling of 0.5 within the receptor and the ligand. The initially docked structures were refined using Prime, refining residues within 5 Å of the ligand poses. From the docking results, the best-docked structures were primarily defined through the Glide, docking, and IFD scores. These scores were used as the Glide score factors in the Epik state penalties to the docking score. This approach allowed for an evaluation of the penalties imposed on the system and provided an overview of the global docking scores. A lower score indicates a more favourable energetic state. Negative values, in particular, indicate that the conformation is energetically favourable, suggesting a stronger binding affinity or stability of the docked complex. The top-scoring models were subsequently subjected to structural alignments with multiple orthologs globally (whole complex) and locally (ATP binding environment) to define the most theoretically applicable structure. RMSD of greater than 2.5 Å indicated insufficient alignment for an appropriate model.

6.3.6. MD simulations of the ATP-*Kp*NNAT complex and post-dynamic analysis

MD simulations further used these validated structures to define the binding dynamics involved with including an ATP substrate within the presence or absence of a divalent metal ion co-factor. The *Kp*NNAT-ATP complexes were placed within a centre space and solvated using the System Builder tool within Schrödinger Maestro v12.2. The System Builder generates an explicit solvent box in the orthorhombic shape. This tool utilised the TIP4P solvent model to generate the solvent box. The net charge of the solvated system was neutralised with sodium ions, and the whole system was equilibrated with 20 mM NaCl, $MgCl_2$ or $CaCl_2$. The whole system was minimised with the OPLS_2005 force field. The generated solvent box was submitted for MD simulations, structured as five 200 nsec replicates forming a cumulative 1 µsec long simulation. Here, each replicate was used as a continuation of the previous. The simulations were set to maintain the isothermal isobaric (NPT) state variable ensemble at 300 K with a pressure of 1.013 bar.

The resulting trajectories were merged and analysed through the post-dynamic analysis software available within Desmond (Schrödinger Maestro v12.2). Where the simulation quality

analysis initially defined the system equilibration, defining the average, standard deviation of the means, and slope of the total energy (kJ/mol), potential energy (kJ/mol), the temperature (K), the pressure (bar), and the volume ($Å^3$). Here the slopes should be as close to 0 as possible, indicating little change within these factors, confirming full equilibration of the simulation system. Upon confirmation of system equilibration, the simulation interaction analysis was performed. The interaction analysis defined the RMSD of the Cα and ATP ligand, the root-mean-square-fluctuations (RMSF) of the sidechains and ATP, the two-dimensional interaction summary (with a 10 % interaction contact cut-off), and the interactions fractions deconvolution.

6.4. Results

To date, there are no crystal structures of *Kp*NNAT, presenting an extreme limitation towards any technique as little is known about the enzyme's physical structure. With this limited information, two plausible strategies exist to simplify model generation for computational simulations. Utilising either homology modelling or fold prediction algorithms, each with advantages and limitations. In this regard, the neural network Rosetta Fold was utilised to define, predict, and develop a complete three-dimensional model of the enzyme. The cDNA sequence, as presented in Chapter 3, was submitted to the online server, and the resulting structures' validity and quality were tested (Baek et al., 2021; Kim et al., 2004). Figure 6.2 denotes the *Kp*NNAT predicted model, represented against the estimated error.

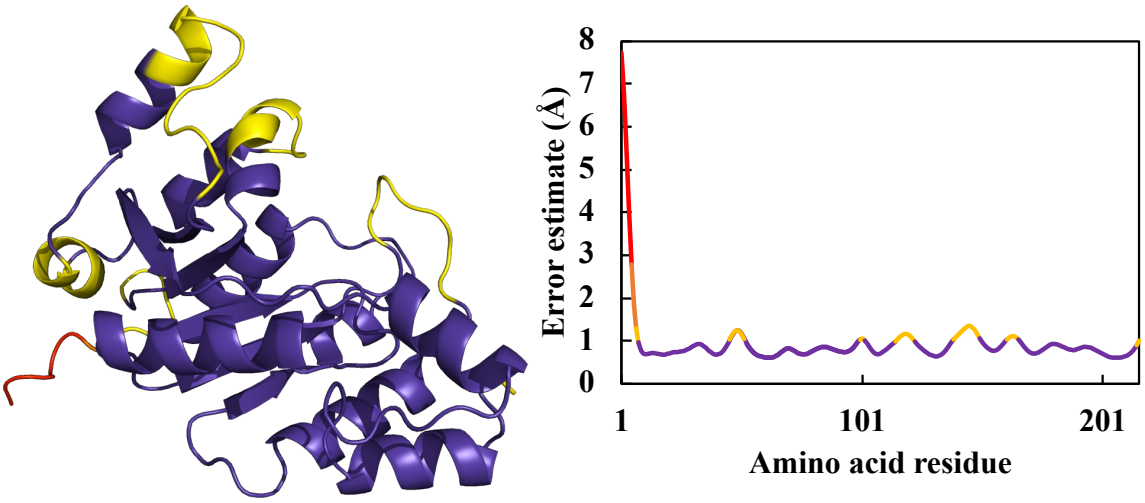

Figure 6.2 Rosetta Fold modelled *Kp*NNAT with its corresponding error estimate. To the left is the 3D representation of the *Kp*NNAT model as the Rosetta Fold server predicted, and to the right is the graph depicting the estimated error of the specific protein regions. The scheme follows an error estimate

greater than 2.5 Å in red, an error estimate between 1.5 Å and 2.5 Å in orange, an error estimate between 1 Å and 1.5 Å in yellow, and an error estimate below 1 Å in purple. Only the flexible N-terminal region displayed an estimated error greater the 2.5 Å. Further, the structure strongly resembles the native reference structures, with error estimates lower than 1.5 Å.

Overall, the model generated by Rosetta Fold had a high confidence yield (between 0-1, the higher, the better) of 0.87. This high confidence was corroborated by low error estimates, with the largest fluctuations existing within a highly flexible N-terminal tail region. This region, characterised by its inherent flexibility, is likely to exhibit higher variability and, as a result, will produce a higher error. The generated model had a satisfactory alignment to solved crystal structures of evolutionary homologs having an averaged RMSD of 0.9 Å when comparing the predicted model to the crystal structure of *Ec*NNAT and a previously generated and published homology model of *Kp*NNAT (Jeje et al., 2022). The global alignment is acceptable but not a sufficient justification for the validity of the predicted model. Therefore, a local alignment targeting the conserved ATP binding regions was conducted. This alignment compared the *Kp*NNAT model to *Ec*NNAT, allowing for identifying and characterising differences between the conserved residues in these regions. An analysis of the variations in the conserved residues can provide a more detailed assessment of the predicted model's validity.

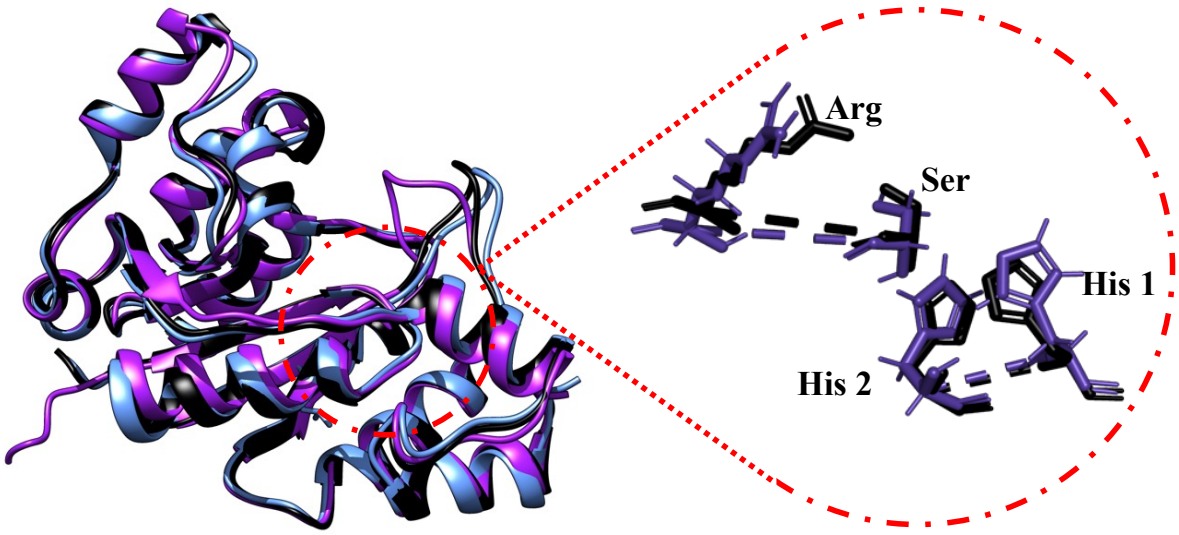

Figure 6.3 Multiple protein structure alignment of the *Kp*NNAT model. The figure above denotes the multiple protein structure alignment to the left, following the predicted *Kp*NNAT model (purple), the *Ec*NNAT crystal structure (black), and the *Kp*NNAT homology model (blue). In its totality, the alignment yielded an average RMSD of 0.9 Å. To the right is an enhanced representation of the conserved regions, following the same colour scheme. The figure depicts the conserved ATP binding motifs, notably (H/T)XXH, depicted as His1 and His2, respectively, and SXXXXR, Ser and Arg, respectively. Both binding domains within the predicted *Kp*NNAT model were remarkably similar to the solved *Ec*NNAT crystal structure.

Figure 6.3 demonstrates that the *Kp*NNAT model Rosetta Fold generated closely resembled the previously accepted reference structures. This similarity was visually depicted through a low RMSD-based comparison with its closest solved evolutionary homolog and a previously utilised homology model. The global RMSD was an excellent indicator of structural validity. However, more than this comparison was necessary to justify further computational modelling. Therefore, the conserved ATP binding domains were analysed by comparing the *Ec*NNAT crystal structure and the predicted *Kp*NNAT model. This step confirmed sufficient structural overlap between all residues of the (H/T)XXH and SXXXXR binding motifs. It was essential to establish sufficient similarity between these components, as it has more recently come to light that these binding motifs are pivotal for the ATP binding event to occur and are extremely sensitive to structural and mutational changes. Given the sufficient local and global overlap, the predicted *Kp*NNAT model had sufficient theoretical backing to confirm viability for further computational modelling. The validity, however, was not the only factor considered. For the structure to be suitable for subsequent computational modelling, it needed to meet specific quality criteria. Thereby, the newly validated structure was submitted to MolProbity for quality assessments.

Table 6.1 MolProbity assessment summary

All-atom contacts	**Clashscore**	0.88		99th percentile
Protein geometry	**Poor rotamers**	0.00	0.00 %	Goal: <0.30 %
	Favoured rotamers	186.00	100.00 %	Goal: >98.00 %
	Ramachandran outliers	0.00	0.00 %	Goal: <0.05 %
	Ramachandran favoured	208.00	99.52 %	Goal: >98.00 %
	MolProbity score	0.77		100th percentile
	Cβ deviations >0.25 Å	0.00	0.00 %	Goal: 0.00
	Bad bonds	5/ 1756	0.28 %	Goal: 0.00 %
	Bad angles	2/ 2397	0.08 %	Goal: <0.10 %
Peptide omegas	**Cis prolines**	1/17	5.88 %	Expected: <5.00 %
Low resolution criteria	**CaBLAM outliers**	1	0.50 %	Goal: <0.10 %
	CA geometry outliers	1	0.48 %	Goal: <0.05 %
Additional validations	**Chiral volume outliers**	0/ 263		
	Waters with clashes	0	0.00 %	

The table above depicts the MolProbity results for the quality assessment of the *Kp*NNAT model. It highlights the Clashscore and the MolProbity score, being 0.88 and 0.77, existing within the 99th and the 100th percentile, respectively. Overall the structure quality was sufficient, with minimal errors or clashes that required reassessment. The only issue was the 0.28 % bad bonds.

Overall, the structure had limited reported errors, outliers, or problematic regions (Table 6.1). Denoting a structure within the 100th percentile in terms of the MolProbity scores, suggesting the structure quality was comparable to other crystal structures of a similar resolution. The primary issue stemmed from the 0.28 % bad bonds. Nevertheless, given the limited Ramachandran outliers and the proportion of favoured rotamer states, the structure quality was generally acceptable for further computational modelling. Figures 6.2, 6.3, and Table 6.1 collectively establish that the *Kp*NNAT model generated by Rosetta Fold possesses both structural validity and the necessary quality to enable further computational modelling. These visual representations and quantitative data proved that the predicted model meets the criteria for its utilisation in subsequent computational modelling studies. Therefore, the *Kp*NNAT

model was prepared for IFD. These IFDs generated multiple complexes under each condition, summarising the best results in Table 6.2.

Table 6.2 Best scoring docked ATP-*Kp*NNAT complexes

Docking conditions		Docking score (kJ/mol)	Glide score (kJ/mol)	Glide emodel	IFD score (kJ/mol)
ATP	**1**	-35.840	-36.141	-125.836	-40346.563
	2	-32.690	-32.991	-115.380	-40339.994
	3	-31.865	-36.045	-116.847	-40334.722
Mg^{2+}-ATP	**1**	-33.798	-34.100	-210.078	-41152.401
	2	-41.597	-41.900	-249.301	-41224.366
	3	-33.798	-34.900	-218.024	-41122.36
Ca^{2+}-ATP	**1**	-42.643	-42.945	-185.974	-41082.738
	2	-37.233	-37.535	-156.175	-41061.274
	3	-39.811	-40.112	-190.337	-41054.328

The table above reflects the three best ATP-*Kp*NNAT complexes within the presence or absence of the divalent metal ions. All depict high-scoring models with limited penalties when considering the glide score. The docking scores were broadly comparable across all conditions; further structural assessments were required to define the most theoretically appropriate structures.

As tabulated above (Table 6.2), the ATP docked *Kp*NNAT were of sufficient quality for further use across all conditions. However, selecting the most appropriate model did not necessarily utilise the top-scoring model. The models were further analysed and compared against crystal structures of similar NNAT species with relevant ligands/ products bound, using this in conjunction with the docking scores to determine the most appropriate model. For all structures, the docking scores were as anticipated, depicting a negative kJ/mol parameter. Again, when considering the glide score, similarly expected results, with limited ionisation penalties across all conditions (Table 6.2).

Given the favourable docking and glide scores, all the presented models were of sufficient quality for further use. The top-scoring models were aligned to several crystal structures i) to define the most appropriate modelled complex and ii) to validate the final chosen complex. From the alignment, the first structures were chosen for the ATP-*Kp*NNAT complex, the ATP-Ca^{2+}-*Kp*NNAT complex, and the third model for the ATP-Mg^{2+}-*Kp*NNAT complex. The third model was chosen as it was the only structure to display the highly bent conformation of the ATP molecule. This conformation allowed for both spatial and conformational alignment of

the ATP molecule. Consequently, these structures were validated by defining i) appropriate ATP spatial coordination and ii) appropriate ATP conformational coordination, using visual cues and RMSD values for the assessment.

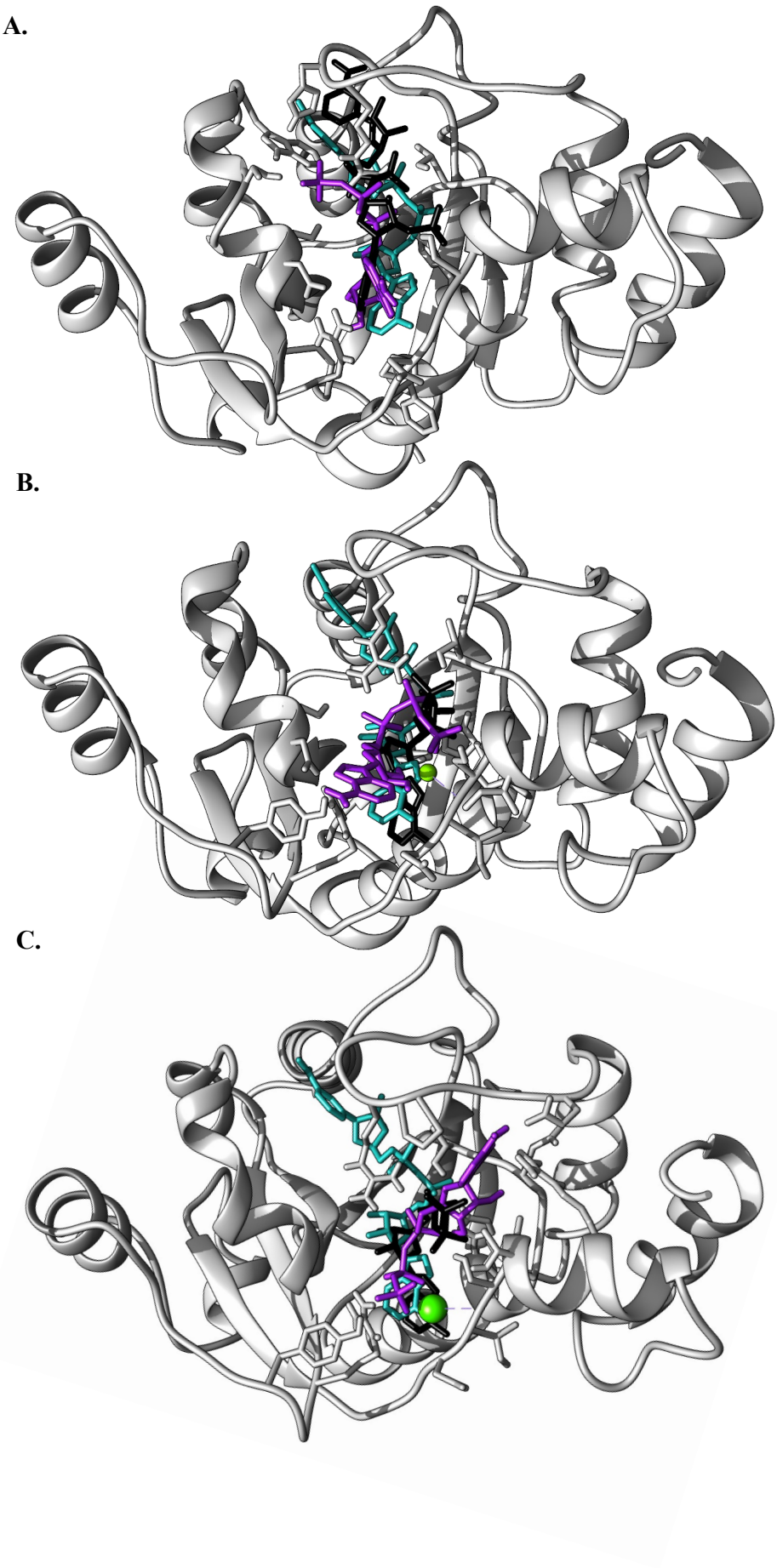
A.
B.
C.

Figure 6.4 ATP-*Kp*NNAT complexes aligned to several reference structures. Above depicts simplified structural alignments to illustrate the similarities and differences between the docked ATP-*Kp*NNAT complexes and solved NNAT crystal structures. A) Depicts ATP-*Kp*NNAT complex, showing docked ATP (purple), the ligand of 3E27 (cyan), and the ligand of 1KQN (black). These reference structures confirmed the correct spatial and conformational coordination of the ATP molecule within the *Kp*NNAT. B) Depicts the ATP-Mg^{2+}-*Kp*NNAT complex, showing docked ATP (purple), the ligand of 1YUN (black), and the ligand of 3E27 (cyan). The alignment to 1YUN yielded highly similar ATP spatial and conformational alignments. C) Depicts the ATP-Ca^{2+}-*Kp*NNAT complex, showing docked ATP (purple), the ligand of 3E27 (cyan), and the ligand of 1YUN (black). The conformational state of the ATP molecule is more extended, with the adenine ring facing inwards (to the core of the enzyme).

The visualisation above (Figure 6.4) represents the spatial and conformational validation of the docked ATP within the ATP-*Kp*NNAT complexes. Across all conditions, sufficient evidence depicts the correct spatial coordination of the ATP molecule, with multiple conformations that align with previously solved crystal structures. These conformations confirm that the divalent metal ions directly interact with the phosphate tail, most likely through electrostatic interactions. These interactions may drive the stabilisation of the ATP molecule through charge mitigation but will also drive the local orientational arrangement of the ATP molecule. This observation aligns with previous knowledge, as it has been established in Chapter 5 that divalent metal ions are primarily involved in the local orientational positioning of the ATP molecule. Here, this potentially allows for specific conformations that promote NNAT activity.

In the absence of the divalent metal ion, a distinct directionality was observed in the ATP molecule. Specifically, the adenine ring was found to face outward while the phosphate tail extended inward. However, in the presence of Ca^{2+}, a reversal of this directionality was observed. Here, the phosphate tail was captured by the divalent metal ion, with the adenine ring extending to the inner enzyme core. The direct interaction between the phosphate tail and the divalent metal ion primarily drove this behaviour. Interestingly, a similar association between the phosphate tail and the divalent metal ion was observed in the presence of Mg^{2+}. However, a notable distinction arose as the adenine ring flipped outward. This conformational distinction allowed for a highly bent arrangement of the phosphate tail. This structural bend was anticipated, as similar confirmations had been documented in multiple other NNAT species. It is crucial to emphasise that the conformations of the complexes mentioned above were considered acceptable because they demonstrated theoretical relevance to the known interactions of the complex. These conformations aligned with the current understanding of how the complex interacts and provided insights that could be applied in a theoretical context. These conformational differences highlight the influence of metal ions on the spatial

orientation of the ATP molecule during docking. The differences between these models were quantified through RMSD to extend this analysis.

Table 6.3 Alignment of docked ATP-*Kp*NNAT models to a set of reference crystal structures.

Reference structure			RMSD (Å)		
PDB	**Ligand**	**Resolution (Å)**	**KpNNAT. no metal**	**KpNNAT. Mg^{2+}**	**KpNNAT. Ca^{2+}**
1YUN	ATP. Mg^{2+}	2.0	1.90	1.57	1.60
3E27	DND. Mg^{2+}	2.2	1.61	1.44	1.48
1KQN	NAD. Xe	2.2	2.24	1.89	2.00
1K4M	NAD	1.9	1.37	1.12	1.15
2H29	NAD	2.0	1.60	1.48	1.53

The table above reflects the structural alignment of the docked ATP-*Kp*NNAT complexes to several NNAT crystal structures. Overall, acceptable RMSD values were observed, with the highest being 2.24 Å.

The structural assessments of the docked ATP-*Kp*NNAT followed two verification steps, i) validate the spatial positioning of the ATP molecule and ii) quantitatively assess the structural differences between the docked models and several related crystal structures. Fortunately, as depicted in Figure 6.4 and Table 6.3, the overall docked structures across all conditions had some relatability to already complexed NNAT crystal structures. Figure 6.4 confirms the relative spatial arrangement of the ATP molecule within *Kp*NNAT. Under different conditions, slight conformational variations were observed in the docking of the ATP molecule. In the absence of any metal ions, the ATP molecule exhibited a more extended conformation, with the adenine ring facing inward. However, in the presence of Ca^{2+}, the ATP molecule adopted a different conformation, with the adenine ring facing outward. In either situation, the phosphate tail seemed to be placed within an accessible region concerning the NMN binding site, which resides deeper within the binding cleft. Therefore, the phosphate tail would be located next to the NMN binding site across all conditions, enabling hydrolysis and conjugation with the NMN substrate.

Further analysis revealed that the docked structures were structurally similar to the respective reference crystal structures, as noted in Table 6.3. Whereby no high RMSD was noted, especially considering structural differences relating to the speciation of the enzymes. Given the structural similarity through all considerations, the selected models were deemed to have

sufficient theoretical relatability to allow further conclusions from more downstream simulations.

Given that these docked structures were of sufficient quality for further assessment, the interactions were more closely evaluated and illustrated below. As represented within Figure 6.5, it is understood that the immediate interaction between ATP and any NNAT is largely predominated by direct connections between the (H/T)XGH and the SXXXXR binding motifs. As previously established, these binding motifs are responsible for the initial recognition and spatial coordination of the ATP binding event. Thereby, it was considered that the docked structures should reflect this coordination. This was confirmed by visualising the *Kp*NNAT to ATP interaction in 3D and 2D interaction diagrams, as displayed below.

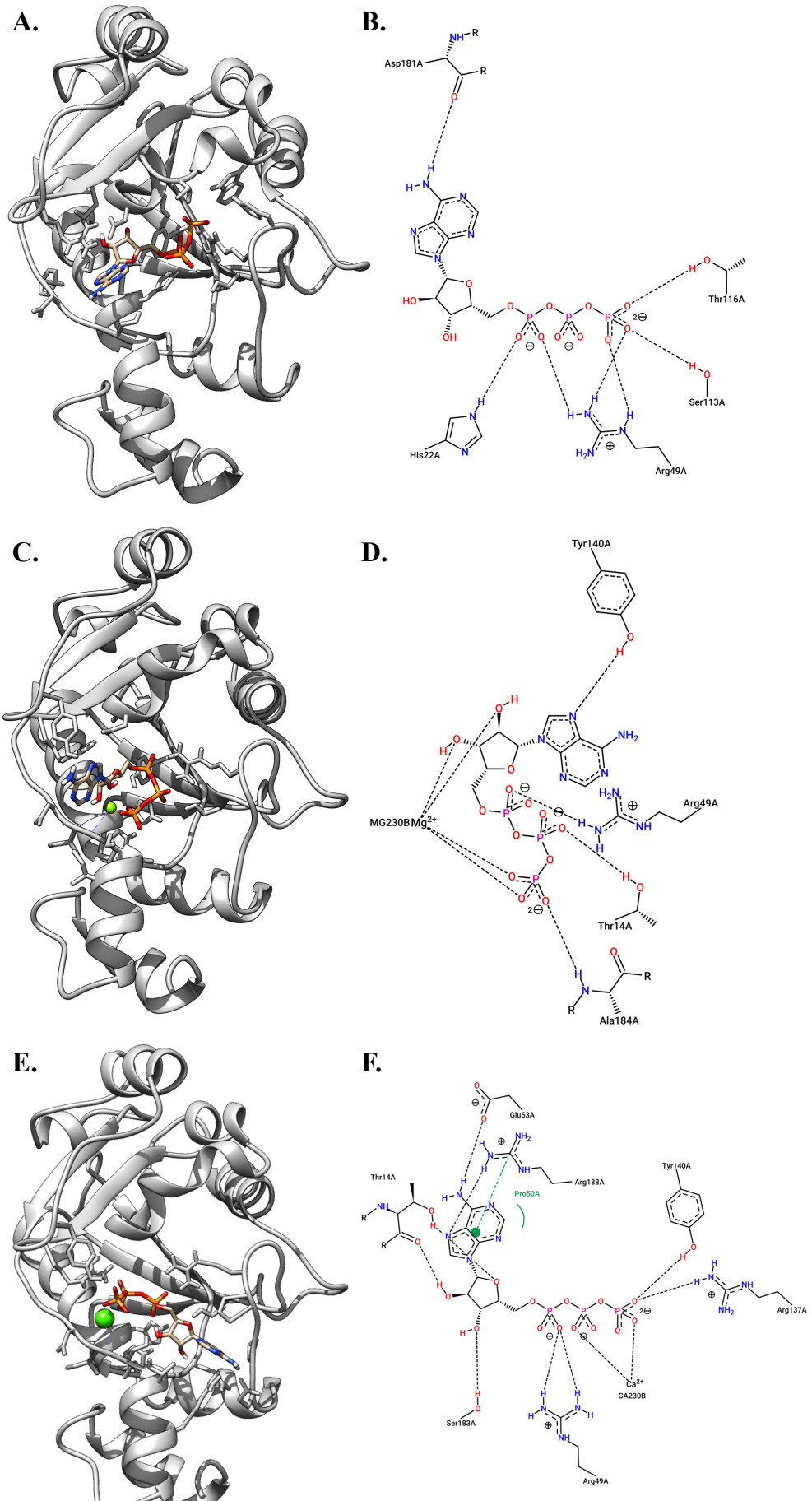
A.
B.
Asp181A
Thr116A
Ser113A
His22A
Arg49A
C.
D.
Tyr140A
MG230B
Mg2+
Arg49A
Thr14A
Ala184A
E.
F.
Glu53A
Arg188A
Pro50A
Thr14A
Tyr140A
Arg137A
Ca2+
CA230B
Ser183A
Arg49A

Figure 6.5 ATP-*Kp*NNAT interaction diagrams derived from docked complexes. The figure above reflects the 3D and 2D interaction diagrams of ATP complexed to *Kp*NNAT in the absence of any divalent metal ion (A and B), with an Mg^{2+} present (C and D), and with a Ca^{2+} present (E and F). A and B display the correct spatial arrangement of the ATP molecule, with direct interaction with His22 and a locationally similar interaction with Asp181, both residing within the conserved binding motifs. C and D display the relatively correct spatial arrangement of the ATP molecule, with locationally similar interactions with Thr14 and Ala184, which are located near the conserved binding motifs. E and F display the correct spatial arrangement of the ATP molecule, with direct interactions with Ser183 and Arg188 and locationally similar interactions with Thr14. This interaction displayed full contact with the SXXXXR binding motif.

Figure 6.5 displays the acceptable spatial arrangement of the ATP molecule within *Kp*NNAT across all conditions. Direct interactions with conserved binding motifs were present within the absence of a divalent metal ion and the presence of Ca^{2+}. Additional locationally similar interactions with residues close to the conserved binding regions within the presence of Mg^{2+}. It is important to note that a direct comparison between the theory and the predicted models is only partially reliable at this stage, as IFD is the generation of a static structure under the implicit solvent model. Therefore, this validation process aimed to monitor whether similar interactions were observed in the predicted models compared to existing crystal structures. The presence of these similar interactions provided a theoretical basis for supporting the accuracy of the predicted models.

Compiling all the information from the previously presented figures, the IFD-generated models of the ATP-*Kp*NNAT complexes displayed sufficient structural similarities with previously solved crystal structures to justify the validity of the models. Therefore, these structures were further used within more downstream MD simulations. Here, the models presented above were solvated within an orthorhombic solvent box generated with the TIP4P solvent model. The solvated system was further supplemented with 150 mM NaCl, 2 mM $MgCl_2$, and 2 mM $CaCl_2$, which was then subjected to 1 µsec MD simulations using Desmond. Fortunately, all systems equilibrated within the first 200 nsec of the simulations, as depicted in the simulation quality analysis summary below.

Table 6.4 Simulation quality analysis.

	No metal			Mg^{2+}			Ca^{2+}		
	Average	Standard deviation	Slope ($psec^{-1}$)	Average	Standard deviation	Slope ($psec^{-1}$)	Average	Standard deviation	Slope ($psec^{-1}$)
Total energy (kJ/mol)	-350446.71	780.23	0	-354109.54	738.48	0	-34792.00	784.81	0
Potential energy (kJ/mol)	-427047.70	652.05	0	-433372.46	616.81	0	-426229.63	657.89	0
Temperature (K)	298.62	1.64	0	298.66	1.51	0	298.62	1.62	0
Pressure (bar)	0.31	164.00	0	0.87	148.98	0	1.60	160.42	0
Volume (A)	296094.64	726.88	0	307015.61	698.84	0.001	303376.92	742.24	0

The table above shows the simulations' total energy, potential energy, temperature, pressure, and volume over a 1 μsec period. Here, the highest slope was 0.001, indicating system equilibration.

Table 6.4 indicates the highest slope of the presented parameters as 0.001, where the lower the slope, the better, aiming for values as close to zero as possible. Lower values indicate little changes with these parameters for the duration of the simulation, which implies that the system has achieved a balanced distribution of energy and properties across the different conditions. Based on the observation that the slopes for all parameters across all conditions were predominantly zero, it was concluded that the simulated systems had reached a state of full equilibrium. The consequent trajectories were analysed, and the evolution of the ATP molecule was mapped using structural alignments.

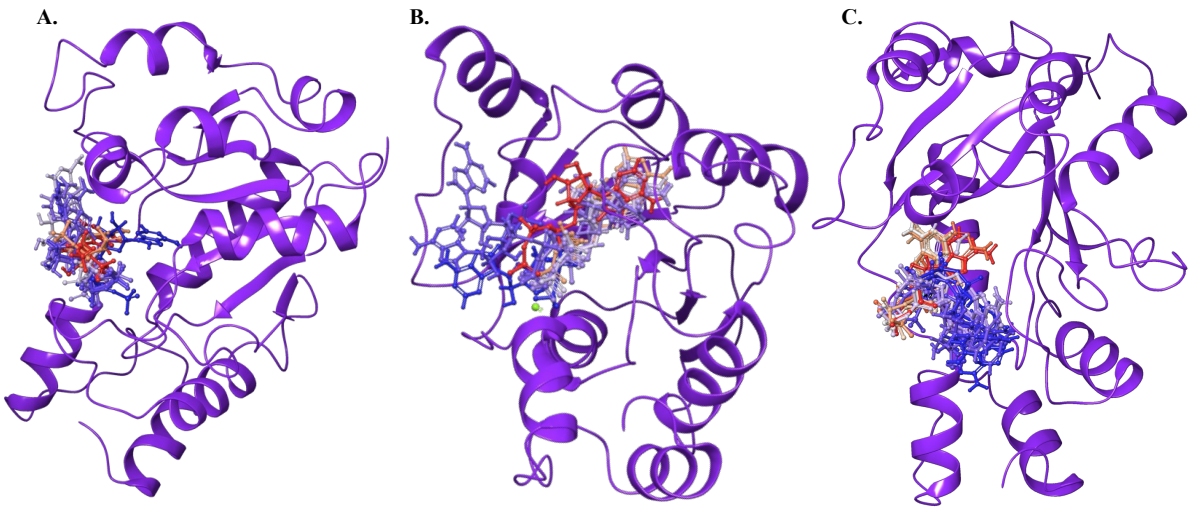

Figure 6.6 ATP evolution across 1 μsec MD simulations. The above reflects the multiple ATP poses present throughout the progression of the MD simulations, detailing the progression through colour, moving from purple to red as the simulation progresses. A) Depicts the absence of divalent metal ions showing the extended ATP conformations. B) Depicts the presence of Mg^{2+} (green), showing the

progressive motion of the adenine ring. C) Depicts the presence of Ca^{2+} (green), showing the relatively stable progression of the ATP molecule.

As presented in Figure 6.6, structural fluctuations of the ATP molecule were present within the presence of the Mg^{2+}. Here, the adenine ring continually moved to a more inward conformation facing the enzyme core. From this, the ATP bent conformation was not maintained throughout the simulation. However, the direct contact between the Mg^{2+} and phosphate tail was maintained. The observed conformational changes can be attributed to the strain imposed on the ATP by the highly bent conformation. This strain arises due to the molecule's tight bending, which stresses the bond between the α and β phosphates. Furthermore, in the absence of the NMN substrate, the central binding cleft within the enzyme core becomes accessible to the adenine ring of the ATP molecule. This accessibility allows for potential interactions between the adenine ring and the residues within the cleft, influencing the overall conformation and stability of the ATP molecule.

Similarly, in the presence of the Ca^{2+}, the adenine ring moved to a more internalised position within the enzyme's central binding cleft. This repositioning is plausible as the main binding cleft maintains stabilisation mechanics for a nucleotide, though typically NMN. The motion of the adenine ring in response to the absence of the NMN substrate can be attributed to the nucleotide-binding region within the enzyme. Theoretically, in the absence of NMN, this region might have facilitated the inclusion of the adenine ring, allowing it to occupy a position within the binding cleft. In the presence of Ca^{2+}, this might have occurred due to spatial convenience, whereas, in the presence of Mg^{2+}, this might have been to allow the relaxation of the tension related to the highly bent ATP conformation.

Comparably, the structural fluctuations were more limited in the absence of any divalent metal ion and the presence of Ca^{2+}. Here, the ATP molecules maintained a relatively extended conformation throughout the simulation progression. In this context, the extended conformation of the ATP molecules indicates that they were already in a favourable and energetically stable state within the binding site. Therefore, they did not undergo substantial structural fluctuations or rearrangements during the simulation, as they did not need to adopt a more relaxed conformation. Given the evolution of the ATP molecule within the ATP-binding site, more comparative studies were required to assess the progressive formations of alternate

protein contacts. For this, a simulation event analysis revealed the RMSD fluctuations of the Cα atoms and the RMSD fluctuations of the ATP for the protein and the ligand itself.

The figure below (Figure 6.7) displays the RMSD fluctuation of the protein structure at several levels throughout the simulations. Across all conditions and within all levels of assessment, the RMSD fluctuations stabilised to the end of the simulation period. This stabilisation was suggestive that the system had reached a relaxed state, and additional simulation time was not required. RMSD fluctuations of the ligand were observed in the presence of the divalent metal ions. However, these fluctuations were thought to be related to the adenine ring motion, set to occupy the vacant NMN binding region, as seen in Figure 6.6. These fluctuations were not of structural concern as the RMSD fluctuations of the ligand, referenced to itself, as depicted in red in Figure 6.7, had limited change. Little change here was suggestive that the structural fluctuations of the ligand concerning the enzyme were not compromising. This confirmed that the structural integrity of the ATP molecule was maintained throughout the simulation period. Across all conditions, especially at the start of the simulations, variability within the RMSD fluctuations was present at all levels. Considering the size and flexibility of the ATP molecule, it is natural to expect fluctuations in its RMSD values as it explores various conformations during the simulation.

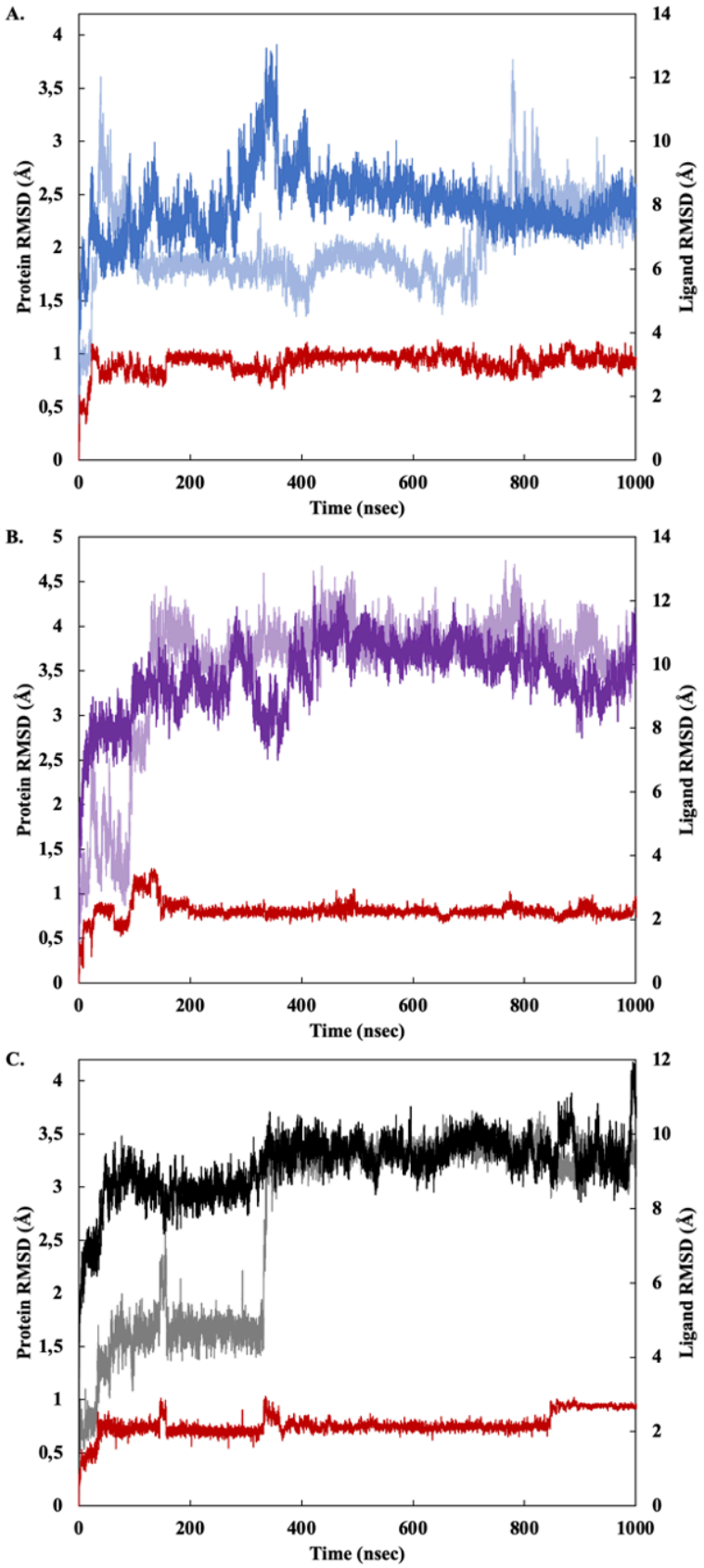

Figure 6.7 RMSD of the protein Cα and the ligand. The figure shows the RMSD fluctuations of the protein Cα (darker) and the ligand (lighter) with respect to the protein and itself (red). Three conditions are compared: A) Absence of divalent metal ion (blue), B) Presence of 2 mM $MgCl_2$ (purple), and C) Presence of 2 mM $CaCl_2$ (black). Across all conditions, RMSD fluctuations stabilise at the end of the

simulations. A) Limited structural fluctuation was observed. B) Large fluctuations in the early stages, potentially indicating motion of the adenine ring. C) Fluctuations in the middle stages were observed, potentially indicating a later shift of the adenine ring.

Across all conditions, the inclusion of the ATP corresponded to an increase in the Cα RMSD throughout the simulation period, confirming previous observations of structural changes upon ATP incorporation (Chapter 4). This is attributed to the increased reactivity within the active site upon its inclusion. Further, across all conditions, the ATP was retained within the active site of the enzyme, inferring the strong compatibility between the substrate and the enzyme's active site. Notably, the increased Cα is greater in value but also stable within the presence of a divalent metal ion compared to its absence. This observation confirms the increased structural flexibility under these conditions as stipulated in Chapters 4 and 5.

Understanding the respective units' structural motion was essential, given the variability of the RMSD fluctuations concerning the enzyme and the ATP molecules. Thereby, the simulation event analysis included RMSF measurements. The RMSF is akin to the RMSD; it measures a residue's movement through the simulation, defining its flexibility. Fortunately, the flexibility of *Kp*NNAT throughout the simulation was quite limited, with little fluctuation apart from a few residues near the C-terminal (Figure 6.7). The limited fluctuations suggested that incorporating the divalent metal ions or ATP does not introduce large structural changes apart from compensatory alterations to account for the new inclusions. This was anticipated as similar binding dynamics have been previously reported on both the secondary and tertiary levels of the structural hierarchy (Chapter 4).

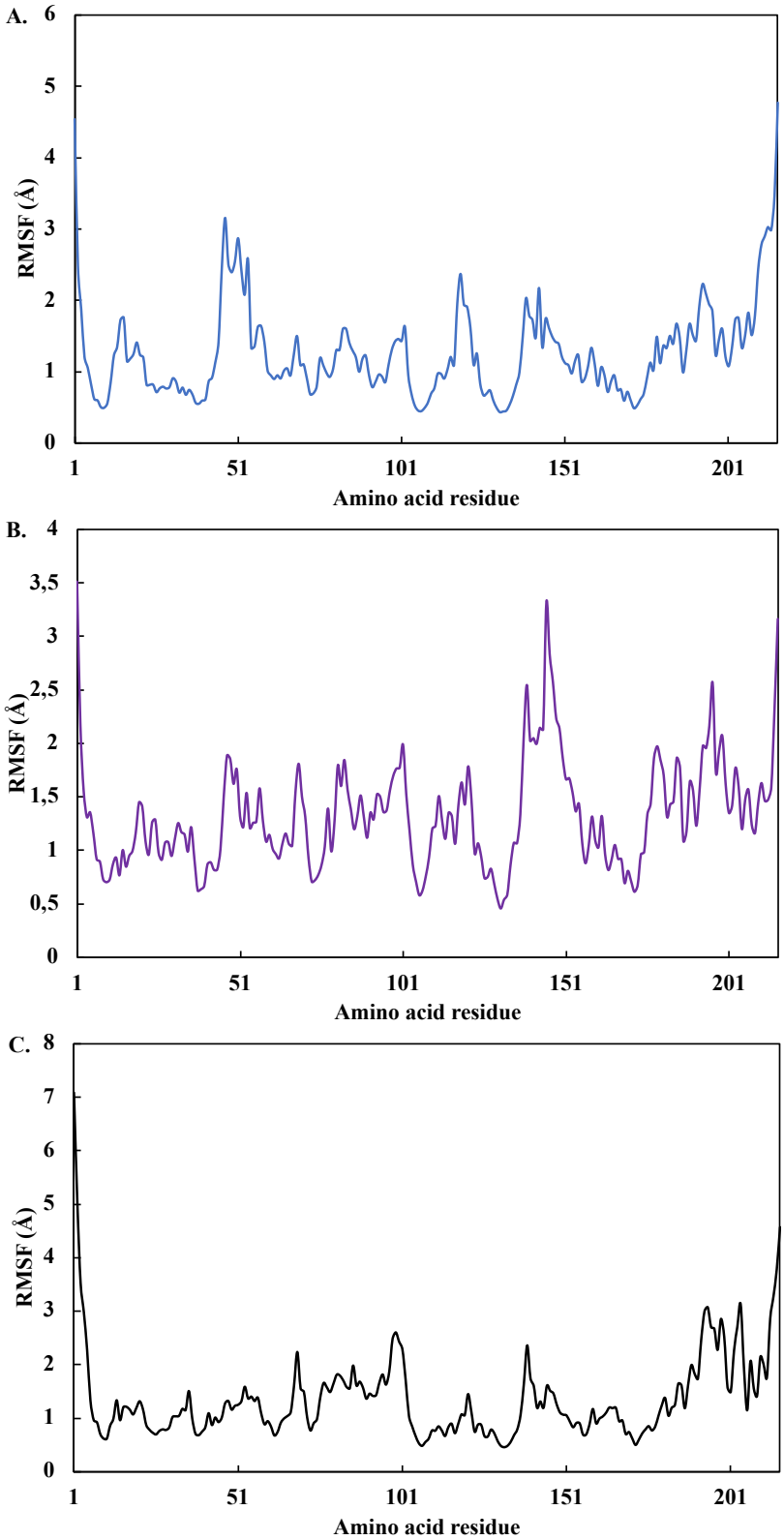

Figure 6.8 RMSF of *Kp*NNAT residues. The figure above depicts the RMSF of *Kp*NNAT throughout a 1 µsec MD simulation. The figure depicts varying conditions: the absence of any divalent metal ion (A or blue), the presence of 2 mM $MgCl_2$ (B or purple), and the presence of 2 mM $CaCl_2$ (C or black). Small RMSF was observed across all conditions, with a partial rise in residues close to the C-terminal.

This structural stability is slightly contrasted when examining the RMSF of the ATP molecule under these conditions. Whereby slight increases in the RMSF were observed in the adenine ring within the presence of both Ca^{2+} and Mg^{2+} (Figure 6.8). These increased fluctuations were anticipated, given the motion of the adenine ring under both conditions within the initial phases of the simulation (Figure 6.6). Figure 6.9 denotes the RMSF of the ligand, with a referencing structure to visualise the numerical atom assignment.

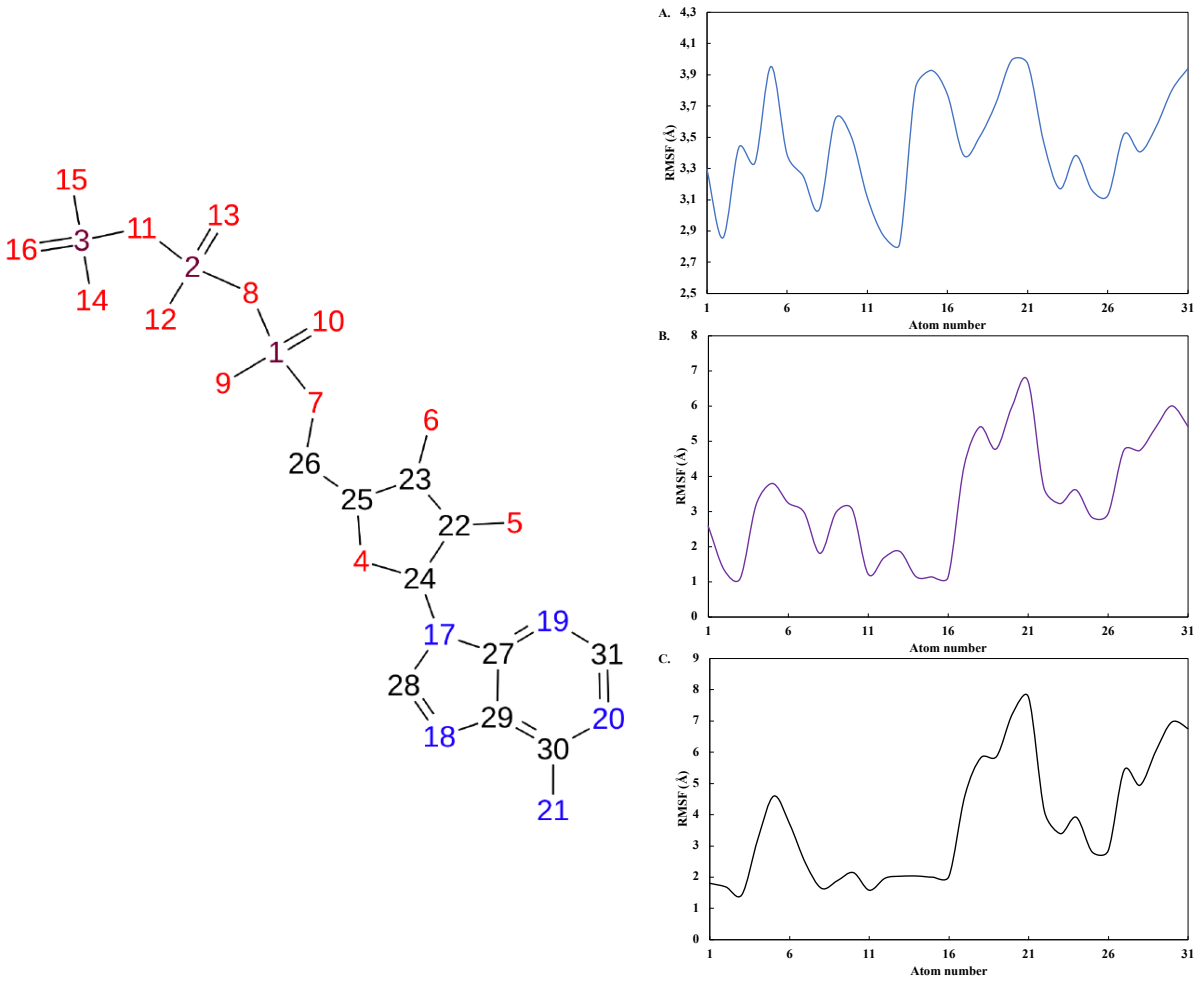

Figure 6.9 RMSF of ATP atoms. The figure above depicts the RMSF of the ATP atoms throughout a 1 µsec MD simulation. The figure depicts multiple conditions: the absence of any divalent metal ion (A or blue), the presence of 2 mM $MgCl_2$ (B or purple), and the presence of 2 mM $CaCl_2$ (C or black). To the left is a representation of the ATP molecule and its numerical atom assignment. Comparably, the adenine ring had flexibility within the presence of the divalent metal ions, whereas, in its absence, the ATP structure had little reported flexibility fluctuations.

Figure 6.9 illustrates large fluctuations of the ATP molecule within the presence of a divalent metal ion. The large fluctuations observed in both Figure 6.7 and Figure 6.8 suggest that the adenine ring migrates, possibly attributed to the ring flipping seen within the enzyme core. In its totality, the largest structural alterations or fluctuations in the *Kp*NNAT and ATP species

were purely present due to the lack of NMN. Due to the absence of NMN, a second nucleotide-binding domain remained unoccupied. This vacant domain facilitated a secondary binding or association event, stabilising the ATP molecule's adenine group. This observation demonstrates that the ATP molecule was retained within the enzyme core (even progressed to a more internal location) due to the site's theoretical binding potential, despite empirical evidence suggesting otherwise.

It is currently understood and empirically proven through stopped-flow analysis (Chapter 5) that a rapid association event and a corresponding disassociation event characterised the ATP binding event. Enabling one of two explanations i) the simulation time frame was not sufficient to visualise the disassociation event, or ii) there was a limitation within the MD software whereby given the numerous factors that enable the theoretical interaction between the adenine nucleotide and the NMN binding interaction, the MD software was unable to justify the molecules release. Fortunately, the figures above (Figures 6.5 – 6.8) confirmed observations within Chapters 4 and 5. They demonstrated that ATP could interact with *Kp*NNAT irrespective of the presence or absence of a divalent metal ion. Moreover, they further support the notion of increased flexibility and reactivity exhibited by both *Kp*NNAT and ATP in the presence of divalent metal ions, as discussed in Chapter 5.

Fortunately, adding the 1 μsec long MD simulations offered a direct perspective of the interaction between ATP and *Kp*NNAT. These simulations enabled the visualisation of the interactions through 2D and 3D interaction diagrams. These interaction diagrams use an averaged protein model depicting the most abundant interactions (based on a 10 % interaction contact cut-off), displaying their relative occurrence throughout the simulation time in percentages. The figure below displays these interactions (Figure 6.10). In the absence of a divalent metal ion, coordination between the conserved (H/T)XGH region, with His-19 coordinating a water molecule near the α phosphate was observed. Additionally, the interaction between Ser-183 and the α phosphate can be visualised, demonstrating the SXXXXR binding motif.

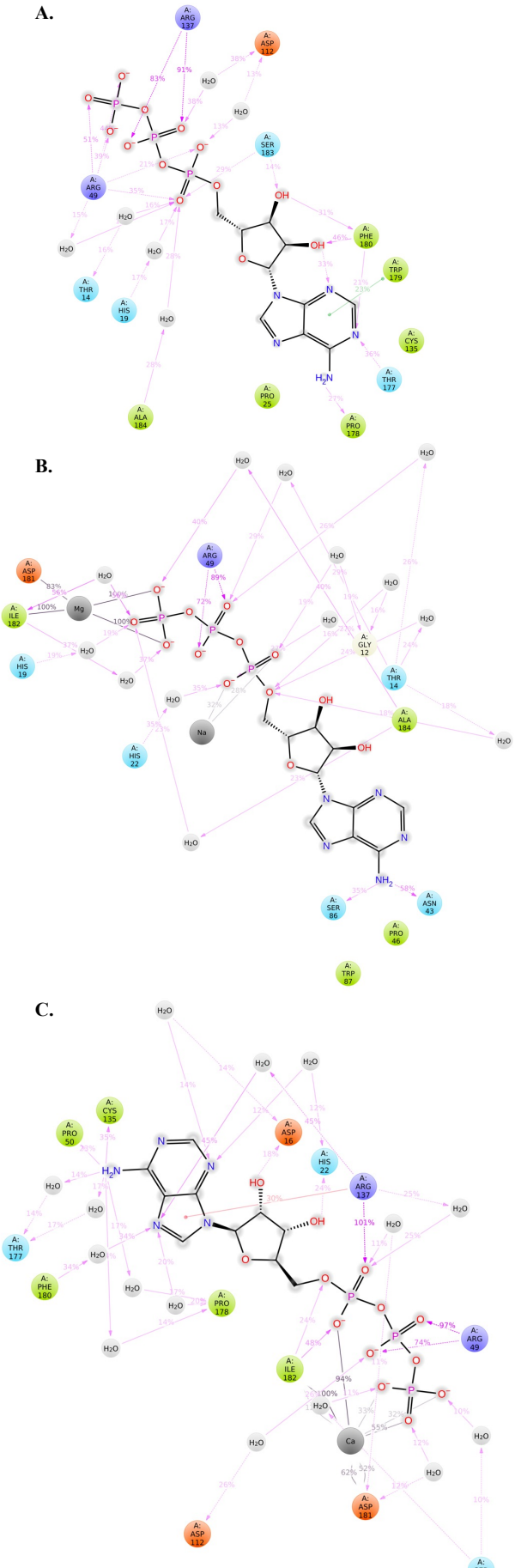
A.
B.
C.

Figure 6.10 2D interaction diagrams between *Kp*NNAT and ATP. A) Displays the interaction without a divalent metal ion, showing that most interactions comprise the N-terminal region with the SXXXXR binding motif. Displaying a higher number of interactions is seen through the higher percentages. Most prominently, Arg-137 and Arg-49 are the predominant contact points for the phosphate tail. B) Displays this interaction in the presence of Mg^{2+}. The interaction with the phosphate tail was predominately due to the Mg^{2+}, as these interactions were maintained for nearly 100 % of the simulation time. Regionally, both the C-terminal and N-terminal ends show reactivity with the substrates, with both Histidines from the (H/T)XGH region involved in the interaction with the phosphate tail. C) Displays this interaction in the presence of Ca^{2+}. Again, both the N-terminal and C-terminal ends are involved in the interaction with the substrates. However, these interactions are primarily with the adenosine nucleoside, with only Ser-183 from the SXXXXR interacting with the phosphate tail.

Orientationally, the presence of the divalent metal ion does not introduce large variation when comparing the presence and absence of Mg^{2+}, as the directional alignment of the ATP remains unchanged. This alignment was reversed in the presence of Ca^{2+}, with the adenine ring facing outwards. Comparably, both metal ions maintained interactions, with the most anticipated conserved residues being His-19, His-22, and Ser-183, which are all components of the (H/T)XGH and the SXXXXR binding motifs. Within the presence of Mg^{2+}, His-19 and His-22 coordinated with water molecules to interact with the β and α phosphates, respectively. With the regional involvement of the C-terminal end. Though the interactions did not necessarily match that proposed in the previous chapters, they still reflected a similar trend. The direct interaction with these conserved groups enabled ATP to interact (even without a divalent metal ion).

In the presence of Ca^{2+}, alternative interaction contacts were made. Here, the His-22 interacted with the sugar moiety, and Ser-183 interacted with the metal ion and coordinated a water interaction with the phosphate tail. However, these observations were not seen in the literature or previous chapters. It does confirm that ATP can bind in the presence of Ca^{2+}, and this seemingly has a similar effect against the phosphate tail, which could be why the *k1* (as seen in Chapter 5) constants were similar compared to Mg^{2+}. These alternative contacts observed in the ATP coordination might indicate the absence of activity when *Kp*NNAT interacts with Ca^{2+}, as noted in Chapter 5.

Though a direct visualisation, as presented above, offered much information, quantitating the interactions required greater specificity. Therefore, a residue-contact plot was generated under these conditions to offer a quantitative idea of the extent of the interactions illustrated in Figure 6.10. These plots can be visualised within Figure 6.11, denoting the interaction fraction whereby the value could be greater than 1 as a single interaction can occur multiple times.

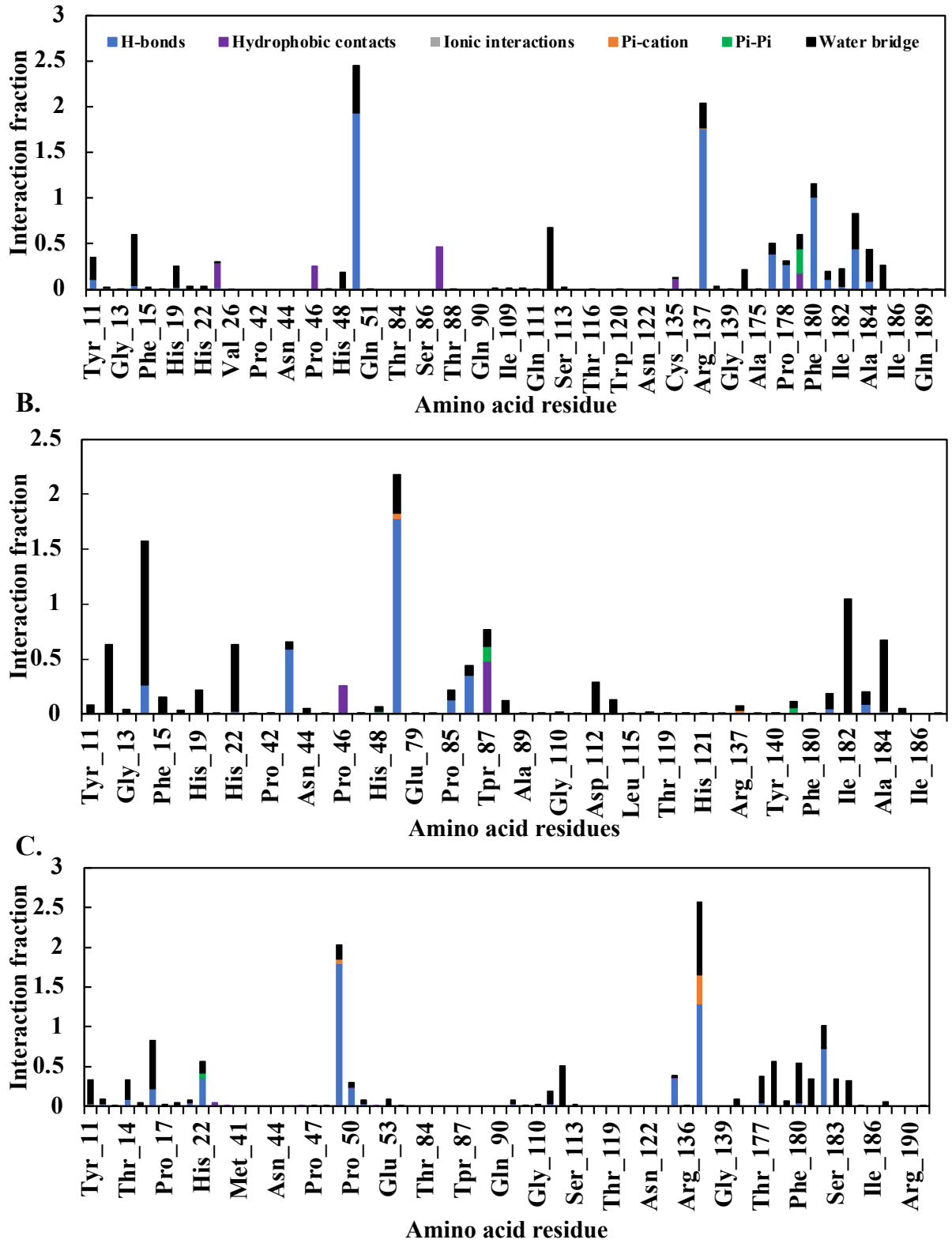

Figure 6.11 Residue-contact fractions of the *Kp*NNAT-ATP interaction. A) Displays the interaction without a divalent metal ion, with a legend as to the bonding component at the top, relevant throughout the entirety of the figure. There was a limited interaction fraction relating to the (H/T)XGH binding region but an increased fraction for the entirety of the C-terminal tail. B) Displays the interaction within the presence of Mg^{2+}, with a high contact fraction with His-19, His-22, His-48, and the C-terminal tail. C) Displays this interaction in the presence of Ca^{2+}, showing a regional interaction from the C-terminal end and His-22.

Overall, the presence of Ca^{2+} and the absence of divalent metal ions showed reduced interactions with the (H/T)XGH binding motif. Where in the absence of any divalent metal ions, this largely correlated to His-22, and in the presence of Ca^{2+}, this correlated to His-19. The regional interaction of the C-terminal end was anticipated. However, seeing that it occurred across all conditions, this may be the initial point of contact for ATP as it is the universal interaction point. Similarly, His-48 appeared to interact with ATP across all conditions.

6.5. Discussion

The introduction of *in silico* simulations has provided a wealth of information across various research fields, expanding our understanding by offering a nearly microscopic view of the atomic realm. These simulations enable the visualisation of systems that cannot be directly observed within *in vitro* studies, thereby evading direct testing. However, it is important to note that these simulations have limitations and can only provide theoretical predictions. Nonetheless, their validation through *in vitro* studies contributes to establishing a more accurate understanding of the underlying phenomena. Throughout the previous chapters, several conclusions were drawn on the structural dynamics and functional kinetics of *Kp*NNAT and *Ef*NNAT, providing clear, justifiable steps to apply simulations. Thereby, given the promise presented within the results relating to *Kp*NNAT, similar conditions were applied to cumulative 1 μsec long MD simulations to offer a visualisation of what has been reported within the previous chapters. Fortunately, most of the results for these simulations strongly agreed with what was seen within the experimental setting.

Within the simulations, it became clear that ATP can associate with *Kp*NNAT within the presence/ absence of the divalent metal ions, as its association was maintained throughout the simulations across all conditions. This statement strongly agrees with the previously presented conclusions (Chapters 4 and 5). Interestingly, as depicted in Figure 6.10, the absence of a divalent metal ion leads to a notable observation: the interaction with ATP is primarily facilitated by the C-terminal tail. This phenomenon was previously mentioned in Chapter 5; however, the reasoning behind it becomes clearer here. The C-terminal region harbours the SXXXXR binding motif, which exhibits a positive dipole that compensates for the highly negatively charged phosphate tail of ATP. This interaction is predominantly stabilising and does not dictate catalytic capability, as reflected in the literature (Han et al., 2006). At which

point, compromising the structure of this SXXXXR region, ATP binding affinity is reduced but not eradicated (D'Angelo et al., 2000; Magni et al., 2004; Sershon et al., 2009; Yoon et al., 2005; Zhang et al., 2003).

Chapter 4 discussed the heightened reactivity of *Kp*NNAT in the presence of ATP. The findings of Jeje *et al.* (2022) strongly supported this observation, indicating that ATP-induced structural modifications at the secondary and tertiary levels contribute to this increased reactivity. Similarly, Saylor *et al.* (1998) demonstrated that an ATP kinase domain, another ATPase, exhibited comparable structural fluctuations upon exposure to ATP. These findings suggest that the structural fluctuations observed in *Kp*NNAT in the presence of ATP are not uncommon. Notably, these structural changes were predominantly witnessed within the C-terminal domain (Figure 6.8), reflecting the increased reactivity of this domain. Based on the accumulated evidence from experimental practices and theoretical studies, ATP can bind to *Kp*NNAT even without a divalent metal ion. The C-terminal domain, which contains the SXXXXR binding motif, likely plays a crucial role in stabilising this interaction and is likely the initial contact point for this binding event.

Although the divalent metal ion does not influence the initial ATP binding event, the mechanism by which it enables activity within *Kp*NNAT remains unclear. In Chapter 5, it was established that while different metal ions may induce similar structural effects during ATP association, only specific metal ions can enable sufficient activity in these enzymes. This idea emphasises the significance of the structural conformation of ATP, indicating that specific amino acids are essential for establishing the required ATP conformation. It was implied that this might reflect the bent conformation of ATP, as the binding of this highly charged substrate is challenging and demands a highly strained conformation.

From the simulations above, solely the presence of Mg^{2+} sufficiently maintained this bent conformation compared to the other conditions. Additionally, the above simulations revealed that the propensity of the bent conformation further illustrated the degree of interaction from the (H/T)XGH binding motif at the N-terminal end, primarily as illustrated in Figure 6.11. Here, only in the presence of Mg^{2+} was the interaction with both histidines retained for at least 25 % of the simulation. It is important to note that the (H/T)XGH is an essential binding motif for the catalytic event to continue, as its alteration can completely eradicate any ATP interaction with the enzyme. Though both histidines will not necessarily continually interact,

it is still interesting that the presence of the Mg^{2+} increased the interaction fractions of both these histidines. Thereby, the cumulative data from the above results as well as Chapter 5, seem to suggest that the divalent metal ion is responsible for introducing and maintaining the strenuous conformational requirements of the ATP substrate and, in so doing, is capable of maintaining its interaction with the catalytically important (H/T)XGH binding motif.

The simulations displayed the binding propensity of *Kp*NNAT to ATP regardless of the conditions. The ATP substrate remained within the binding pocket for the whole length of the MD simulations. Without a divalent metal ion, the retention was more surface-based with limited, defined interactions, as seen in Figures 6.5, 6.9 and 6.10. The presence of either divalent metal ion drastically changed this retention, with the predominant contact point being between the phosphate tail and the metal centre. This strong retention resulted from the divalent metal ions primarily contributing to electrostatic interactions with the ATP. However, to define the divalent metal ions as the sole contributors to this strong retention is inaccurate. This inaccuracy stems from the thought that multiple factors influence the stabilising events that enable this strong retention. Unfortunately, here these might not be directly observable as the simulation time would have likely needed to be 100-fold longer to visualise any dissociation event.

From the above-presented trajectories, within the absence of NMN, the adenine moiety flipped over and occupied a deeper binding cleft, likely that of NMN (Figure 6.6). This phenomenon allowed for a more extended ATP conformation within the presence of the divalent metal ions. This ring flip was the predominant cause of the RMSF variations within the adenine moiety (Figure 6.9). There is limited evidence relating to this event, with the primary reference point being the product NAD^+. Here, NAD^+ does bind in a similar surface-based manner as the ring-flipped ATP, occupying a similar binding pocket; this is seen within the presence of both Mg^{2+} and Ca^{2+} (Huang et al., 2010; Olland et al., 2002; Sershon et al., 2009; Zhang et al., 2002). Considering the resemblance between ATP and NMN, it is plausible that the adenine ring could occupy a binding pocket similar to that of NMN. Thereby, this ring flip was considered a consequence of the absence of NMN, detailing a relief to the strenuous bent conformation by producing a more stable but less reactive extended ATP conformation.

Fortunately, the MD simulations ultimately validated the observations made in the preceding chapters and provided intriguing insights into the dynamic structural changes associated with

the ATP binding process. Collectively, the findings indicate that ATP can bind to *Kp*NNAT even without a divalent metal ion, suggesting that the divalent metal ion primarily plays a structural role rather than directly influencing catalytic activity. In this context, the local conserved sequences facilitate the initial ATP binding, while the divalent metal ion serves to orient the phosphate tail of the ATP molecule. As a result, a bent conformation of ATP is achieved in the presence of Mg^{2+}.

7. Chapter seven
Broad discussion and final comments

7.1. Introduction

More recently, research into the catalytic mechanisms of various ESKAPE based enzymes have drastically increased. This in part to the ESKAPE classification itself, providing focus for the research and development of novel anti-microbial therapeutic strategies. But for this to occur a fundamental understanding of the catalytic mechanism is required. This can be seen with the recent publications of Daya *et al*., (2022) and Jeje *et al*., (2022) who have started to define the structural and functional implications of various catalytic events relating to *Kp*NNAT. These recent publications further define the fundamental understanding of this enzyme's binding dynamics and functional kinetics, adding to the older publications. In this regard, the research as demonstrated within the previous chapters set out to build on these fundamentals by focusing more exclusively on the ATP binding event to both *Kp*NNAT and *Ef*NNAT. Briefly, numerous investigations highlight the ATP binding event in a variety of species, excluding *Kp*NNAT and *Ef*NNAT, detailing the fundamental, but in this system theoretical, principles behind ATP association within an NNAT enzyme. These models, however, do not define the dependence of this binding event to the presence of specific divalent metal ion co-factors that are pivotal for enzyme activity. These models define this binding event as follows: i) ATP associates within an upper hydrophobic cleft in association with a divalent metal ion (typically Mg^{2+}), ii) conserved residues, more specifically the catalytically important (H/T)XGH domain, help define the conformational arrangement of the ATP within this active site, and then finally iii) the highly charged phosphate tail of the ATP is stabilised presumably with the help of the divalent metal ion. This summary represents the fundamental understanding of how ATP interacts with an NNAT enzyme and has largely been confirmed within the systems presented within the previous chapters. The involvement of the divalent metal ion, however, was in slight contradiction with its originally proposed function, but due to the corroboration between the stopped-flow data (presented in Chapter 5) and the computational simulations (presented in Chapter 6), simply meant that its stabilising role is slightly more complicated than originally thought. With this in mind, several investigations were reported within the previous chapters, and each had a contribution to the final conclusions, thereby, this section will tie together the data as presented within the previous chapters, detailing their contributions to the final conclusions as well as their limitations and other considerations.

7.2. NNAT and ATP, the first point of contact

Throughout multiple experiments it was clear that ATP can bind to both *Kp*NNAT and *Ef*NNAT without a divalent metal ion present (as presented in Chapter 4-6). Illustrating the binding potential of the SXXXXR binding motif, again, this motif is located within the C-terminal end of the protein and drives the primary point of contact between the NNAT enzyme and the ATP substrate. This contact point can be specifically visualised through Figure 6.11 (Chapter 6), depicting the increased contact ratio of the C-terminal domain across all conditions with *Kp*NNAT. This is specific to *Kp*NNAT, unfortunately, as *Ef*NNAT did not yield sufficient experimental evidence for such verification. This illustrates that the C-terminal domain has the largest degree of contact with the ATP substrate. However, given that within physiological conditions, ATP is rarely considered a free-floating molecule and is largely considered to exist as a complex with a divalent metal ion, most commonly Mg^{2+}. Since the presence or absence of the divalent metal ion does not influence the association of ATP, and given ATP rarely exists outside of a typical ATP-Mg^{2+} complex, it is reasonable to assume that the ATP association event might be initially driven by the SXXXXR binding motif. Fortunately, the assumption is not without theoretical merit as the positive dipole imposed by this C-terminal region provides compensatory electrostatic binding interactions akin to what was originally anticipated for the divalent metal ions. Thereby, the SXXXXR binding domain along with the C-terminal region might present sufficient compensatory interactions to facilitate the initial ATP interaction with *Kp*NNAT. Which will be followed by the metal coordination of the ATP's triphosphate tail allowing the formation of an active complex allowing the ATP hydrolysis reaction to continue.

7.3. Structural involvement of the divalent metal ions within the ATP-NNAT complexes

As briefly discussed previously, the combination of computational simulations and experimental validations allowed for the estimation of the major events relating to the ATP association to predominantly *Kp*NNAT. In this regard, it has already been concluded that the SXXXXR binding motif at the C-terminal domain, is the most likely candidate for initial interaction even though this interaction might not be exclusively limited to the C-terminal region. This initial interaction was quickly followed by the coordination from the metal ion, to facilitate the correct ATP conformation, being the bent conformation as previously discussed. This highly bent conformation can, for simplicity, be viewed as the active conformation. The reasoning behind defining it as the active conformation, relates to the bonding network created in its presence. As illustrated throughout multiple points within chapter 6, the active

conformation, allows for the theoretically appropriate interactions, being with both the catalytically important (H/T)XGH binding motif as well as for the structurally important SXXXXR binding motif. These interactions increase proportionally in the presence of Mg^{2+}, which is thus far the only condition whereby *Kp*NNAT maintains its catalytic activity (as reported in chapter 5, figure 5.2). This conformation also corresponds to a greater reactivity of the ATP substrate, seeing greater and more drastic conformational fluctuations. Which strongly correlates to the increased k_d values in the presence of a divalent metal ion.

In chapter 5, this ideology was first illustrated, stating that the presence of the divalent metal ions allow for a greater sampling of strenuous conformations. Which implies that the divalent metal ions can allow the ATP molecule to adopt more strenuous conformations, which in the presence of Mg^{2+} resulted in increased contact with the catalytic domains. Though this conformational positioning is certainly beneficial for the enzymes' catalytic process, it is not inherently beneficial to the enzyme-substrate complex stability. This specifically was visualised in table 5.1 (chapter 5), which displayed the increased k_d of the ATP substrate from *Kp*NNAT in the presence of a divalent metal ion. Though, this might seem counterintuitive compared to the initial estimations as to the function of the divalent metal ion co-factors. This, however, is not entirely correct as in the presence of these co-factors, the binding to the catalytically important residues increase, and regardless of the ATP positioning, the metal centre remains. Suggesting its potential to interact with the developing intermediates and offer further stabilisations to the developing charges generated by the evolving intermediates.

In its totality, the divalent metal ions, more specifically Mg^{2+}, played less of a fundamental kinetic role than anticipated. With its predominant role focusing on the correct positioning of the triphosphate tail, akin to what is seen within multiple polymerases. Though, not specifically influential in kinetics of the event, it is still fundamental in the progression of the catalytic event, as without it the necessary catalytic contacts are not made.

7.4. Study contributions and future directions

The preceding chapters have provided a comprehensive analysis of the ATP association event in *Kp*NNAT and have shed light on the factors contributing to the inactivity of *Ef*NNAT. This parameterization of ATP association in *Kp*NNAT represents a significant contribution to the field, consolidating various sources and confirming that ATP binds to *Kp*NNAT through direct

interactions with the SXXXXR binding motif. Subsequently, coordination with Mg^{2+} induces a bent conformation, crucial for effective interaction with the conserved (H/T)XGH region and ATP hydrolysis. This mechanistic understanding holds promise for developing potential druggable targets in AMR research.

However, it is essential to note that this study primarily focuses on fundamental scientific exploration. By achieving a deeper understanding of the functional kinetics and structural dynamics of *Kp*NNAT, numerous avenues for further investigation arise. For example, it would be intriguing to investigate whether adenine ring migrations, observed in Chapter 6, still occur in the presence of NMN. Additionally, the kinetic data presented in Chapter 5 can serve as a starting point for characterizing other kinetic parameters, such as V_{max} and K_m, by employing ITC for kinetic assessment. Furthermore, a specific focus on the NMN substrate could elucidate its interactions and contributions to the catalytic event. Repeating the Mant-ATP association study from Chapter 5 in the presence of NMN may uncover potential cooperativity between these substrates. In summary, numerous avenues for exploration remain within *Kp*NNAT.

In contrast, the following steps for *Ef*NNAT appear relatively straightforward. As illustrated in Chapter 5, *Ef*NNAT exhibits diminished ATP association, likely leading to its inactivity. The $(his)_6$-tag is a potential culprit, as its presence may introduce increased flexibility in the nearby (H/T)XGH binding region, hampering effective ATP binding. This hypothesis is supported by the known influence of polyhistidine affinity tags on recombinant protein behaviour and the demonstrated impact of structural alterations in the (H/T)XGH region on ATP binding in NNAT enzymes. A vector redesign is recommended to assess whether the $(his)_6$-tag is indeed responsible. The inclusion of a thrombin cleavage site upstream of the affinity tag would enable its removal during purification. If the $(his)_6$-tag is found to interfere with the (H/T)XGH binding region, eliminating it should enhance the catalytic capability of the enzyme.

Overall, this study has significantly advanced our understanding of the ATP association event in KpNNAT and highlighted avenues for further exploration. In the case of EfNNAT, addressing the issue of ATP association and investigating the potential impact of the $(his)_6$-tag are crucial next steps to uncover the reasons behind its inactivity.

7.5. Experimental limitations and final comments

The investigations into the ATP binding event to *Kp*NNAT and *Ef*NNAT, did not proceed without certain unfortunate limitations. The most fundamental limitation regards the absence of viable experimental data to further validate computational simulations of *Ef*NNAT. With further limitations that pertain to both experimental and computational concerns. The former primarily concerns the negative impact of a Mant group on any kinetic event, and the latter concerns the lack of a crystal structure used within the computational section opening several concerns of accuracy and reliability. These limitations are important to consider as they influence the reliability of the data presented.

The recombinant *Ef*NNAT posed several challenges throughout the progression of this project, with the fundamental problem being its unfortunate inactivity which was explained through alternate substrate selectivity. This idea, however, has shifted with more recent data, as seen within Chapter 5, *Ef*NNAT was inactive with the canonical NAD^+ synthesis pathway, though further stopped-flow data illustrated a lack of ATP binding in its entirety. The chapters leading to this explained structural changes relating to fold-disruptions of *Ef*NNAT in the presence of ATP, seen on both a secondary and a tertiary level. This, however, did not provide any quantitation to the binding event. Taken together, these separate observations indicate that ATP interacts with recombinant *Ef*NNAT. Still, this interaction is not of sufficient quantity or strength to promote the further progression of the catalytic pathway. The reason behind this is unclear, with the prevailing theory dictating that the uncleavable $(his)_6$-tag at the N-terminal end introduces interference within the ATP-*Ef*NNAT complex. With the emphasis on the catalytic importance of the N-terminal end, as seen previously, perhaps this introduced interference by the $(his)_6$-tag, which could prevent stable binding, further disabling the progression of the catalytic event. Unfortunately, if this is the case, it would indicate a fundamental flaw within the original vector design and would require the reconstruction of this vector to test this theory more directly. Given this fundamental limitation, further considerations can be made within both the computational and experimental setups.

The most predominant limitation relating to the experimental data as presented revolves around the unavoidable implications of including a Mant fluorophore within the stopped-flow kinetic trials. Unfortunately, the Mant-fluorophore has a known impact on the kinetic progression of enzymes. This was most fundamentally illustrated by Ni *et al,* (2000) depicting a three-fold

increase with the k_d values with Mant-ATP as compared to ATP, testing ATP binding within protein kinase A. These observations could introduce concern of a negative influence on the data presented. However, the k_d values presented in Chapter 5 are in strong agreement with both in-house and published experimental data, mitigating the connotation of the Mant-group's influence. Further, a fundamental limitation relating to the computational investigations relate to the use of a series of predicted structures for the varying *Kp*NNAT-ion complexes. This was unfortunately the most accurate alternative to direct structure solving techniques. Even though these predicted structures were carefully vetted for any mismatch to what is currently understood to be correct. This still introduces bias and error, though unavoidable, it still negatively impacts the reliability of the data presented within Chapter 6, especially when considering that this introduction was made at the starting phases of the computational simulations. However, considering this, the presented models still strongly reflect what has been reported in literature and strongly corresponds to the experimental results as seen within the leading chapters.

Unfortunately, the research presented above is influenced by several limitations, which may have a negative influence on the reliability of the data reported. The most fundamental concern focuses on the lack of validating experimental results for *Ef*NNAT to validate downstream *in silico* models. Here, the inactivity of *Ef*NNAT seems to relate to an inability to bind a ATP, a potential consequence of erroneous vector design. Separate from this, the lack of a crystal structure for *Kp*NNAT negatively impacted both the progression and reliability of the generated *in silico* models. These were mitigated through rigorous validation steps but are still subject to introduced bias.

7.6. Conclusion

To define and apply any target for potential drug investigation requires a fundamental understanding of the biophysical properties relating to the target and whether these properties can be exploited. Here, both *Kp*NNAT and *Ef*NNAT were considered potential druggable targets and have more recently been the subjects of research to attempt to identify and confirm several of these biophysical properties. The research presented above is no exception and attempted to identify the role of the divalent metal ion in the canonical NAD^+ synthesis pathway, by establishing its role within the ATP binding event within both *Kp*NNAT and

*Ef*NNAT. Here, the theoretical model as presented earlier can be adapted to represent the current systems more appropriately.

Firstly, the initial interaction of the ATP substrate seems to be predominantly driven by the SXXXXR binding motif located at the C-terminal end. This interaction extends past this motif and encompasses a large composition of the C-terminal end. These residues convey a positive dipole that seems to enable the necessary compensatory interactions that enable the inclusion of the ATP substrate complexed to a divalent metal ion co-factor. Secondly, this initial interaction is immediately followed by the coordination from the divalent metal ion, typically Mg^{2+}. This coordination has two observable implications for the NNAT-ATP complex; i) this seems to enable to conformationally position the ATP substrate in a highly bent conformation that enables the appropriate positioning with the catalytically important (H/T)XGH motif, and ii) increases the reactivity of the ATP substrate enabling a greater sampling of conformational outcomes and subsequently negatively impacts the stability of the NNAT-ATP complex. Throughout this explanation, the flexibility of the ATP is apparent but is largely mitigated by the large proportion of compensatory interactions present.

With the presented summary of the major findings, it is important to acknowledge the short-comings and limitations of the presented research. Which can largely be summarised to a lack of available validating data, requiring further research to clarify specific unexplained events. Fortunately, the research presented above may provide a fundamental understanding as to the binding mechanics of the ATP substrate to the NNAT enzyme specifically annotating the fundamental structural impact conveyed by the necessary divalent metal ion co-factor.

References

Alemayehu, T., Hailemariam, M., 2020. Prevalence of vancomycin-resistant enterococcus in Africa in one health approach: a systematic review and meta-analysis. Sci. Rep. 10, 20542. https://doi.org/10.1038/s41598-020-77696-6

Arias, C.A., Murray, B.E., 2012. The rise of the Enterococcus: beyond vancomycin resistance. Nat. Rev. Microbiol. 10, 266–278. https://doi.org/10.1038/nrmicro2761

Arnold, F.H., 1991. Metal-affinity separations: a new dimension in protein processing. Biotechnol. Nat. Publ. Co. 9, 151–156. https://doi.org/10.1038/nbt0291-151

Baek, M., DiMaio, F., Anishchenko, I., Dauparas, J., Ovchinnikov, S., Lee, G.R., Wang, J., Cong, Q., Kinch, L.N., Schaeffer, R.D., Millán, C., Park, H., Adams, C., Glassman, C.R., DeGiovanni, A., Pereira, J.H., Rodrigues, A.V., van Dijk, A.A., Ebrecht, A.C., Opperman, D.J., Sagmeister, T., Buhlheller, C., Pavkov-Keller, T., Rathinaswamy, M.K., Dalwadi, U., Yip, C.K., Burke, J.E., Garcia, K.C., Grishin, N.V., Adams, P.D., Read, R.J., Baker, D., 2021. Accurate prediction of protein structures and interactions using a 3-track neural network. Science 373, 871–876. https://doi.org/10.1126/science.abj8754

Begley, T.P., Kinsland, C., Mehl, R.A., Osterman, A., Dorrestein, P., 2001. The biosynthesis of nicotinamide adenine dinucleotides in bacteria. Vitam. Horm. 61, 103–119. https://doi.org/10.1016/s0083-6729(01)61003-3

Bowers, K.J., Chow, E., Xu, H., Dror, R.O., Eastwood, M.P., Gregersen, B.A., Klepeis, J.L., Kolossvary, I., Moraes, M.A., Sacerdoti, F.D., Salmon, J.K., Shan, Y., Shaw, D.E., 2006. Scalable algorithms for molecular dynamics simulations on commodity clusters, in: Proceedings of the 2006 ACM/IEEE Conference on Supercomputing, SC '06. Association for Computing Machinery, New York, NY, USA, pp. 84-es. https://doi.org/10.1145/1188455.1188544

Corzo, J., 2006. Time, the forgotten dimension of ligand binding teaching. Biochem. Mol. Biol. Educ. 34, 413–416. https://doi.org/10.1002/bmb.2006.494034062678

Covarrubias, A.J., Perrone, R., Grozio, A., Verdin, E., 2021. NAD+ metabolism and its roles in cellular processes during ageing. Nat. Rev. Mol. Cell Biol. 22, 119–141. https://doi.org/10.1038/s41580-020-00313-x

Covy, J.P., Giasson, B.I., 2010. The G2019S pathogenic mutation disrupts sensitivity of leucine-rich repeat kinase 2 to manganese kinase inhibition. J. Neurochem. 115, 36–46. https://doi.org/10.1111/j.1471-4159.2010.06894.x

D'Angelo, I., Raffaelli, N., Dabusti, V., Lorenzi, T., Magni, G., Rizzi, M., 2000. Structure of nicotinamide mononucleotide adenylyltransferase: a key enzyme in NAD+ biosynthesis. Structure 8, 993–1004. https://doi.org/10.1016/S0969-2126(00)00190-8

Davin-Regli, A., Lavigne, J.-P., Pagès, J.-M., 2019. Enterobacter spp.: Update on Taxonomy, Clinical Aspects, and Emerging Antimicrobial Resistance. Clin. Microbiol. Rev. 32. https://doi.org/10.1128/CMR.00002-19

Daya, T., Jeje, O., Maake, R., Aloke, C., Khoza, T., Achilonu, I., 2022. Expression, Purification, and Biophysical Characterization of Klebsiella Pneumoniae Nicotinate Nucleotide Adenylyltransferase. Protein J. 41, 141–156. https://doi.org/10.1007/s10930-021-10037-2

De Angelis, G., Fiori, B., Menchinelli, G., D'Inzeo, T., Liotti, F.M., Morandotti, G.A., Sanguinetti, M., Posteraro, B., Spanu, T., 2018. Incidence and antimicrobial resistance trends in bloodstream infections caused by ESKAPE and Escherichia coli at a large teaching hospital in Rome, a 9-year analysis (2007-2015). Eur. J. Clin. Microbiol. Infect. Dis. Off. Publ. Eur. Soc. Clin. Microbiol. 37, 1627–1636. https://doi.org/10.1007/s10096-018-3292-9

De Oliveira, D.M.P., Forde, B.M., Kidd, T.J., Harris, P.N.A., Schembri, M.A., Beatson, S.A., Paterson, D.L., Walker, M.J., 2020. Antimicrobial Resistance in ESKAPE Pathogens. Clin. Microbiol. Rev. 33. https://doi.org/10.1128/CMR.00181-19

De Ruyck, J., Famerée, M., Wouters, J., Perpète, E.A., Preat, J., Jacquemin, D., 2007. Towards the understanding of the absorption spectra of NAD(P)H/NAD(P)+ as a common indicator of dehydrogenase enzymatic activity. Chem. Phys. Lett. 450, 119–122. https://doi.org/10.1016/j.cplett.2007.10.092

Emanuelli, M., Natalini, P., Raffaelli, N., Ruggieri, S., Vita, A., Magni, G., 1992. NAD biosynthesis in human placenta: purification and characterization of homogeneous NMN adenylyltransferase. Arch. Biochem. Biophys. 298, 29–34. https://doi.org/10.1016/0003-9861(92)90089-f

Emanuelli, M., Raffaelli, N., Amici, A., Fanelli, M., Ruggieri, S., Magni, G., 1996. Three-minute high-performance liquid chromatographic assay for NMN adenylyltransferase using a 20-mm-long reversed-phase column. J. Chromatogr. B Biomed. Appl. 676, 13–18. https://doi.org/10.1016/0378-4347(95)00408-4

Engelhard, M., Evans, P.A., 1995. Kinetics of interaction of partially folded proteins with a hydrophobic dye: evidence that molten globule character is maximal in early folding intermediates. Protein Sci. Publ. Protein Soc. 4, 1553–1562. https://doi.org/10.1002/pro.5560040813

Essel, V., Tshabalala, K., Ntshoe, G., Mphaphuli, E., Feller, G., Shonhiwa, A.M., McCarthy, K., Ismail, H., Strasheim, W., Lowe, M., Perovic, O., Hlonipho, M., Govender, N.P., 2020. A multisectoral investigation of a neonatal unit outbreak of Klebsiella pneumoniae bacteraemia at a regional hospital in Gauteng Province, South Africa. S. Afr. Med. J. 110, 783–790. https://doi.org/10.7196/SAMJ.2020.v110i8.14471

Foka, F.E.T., Kumar, A., Ateba, C.N., 2018. Emergence of vancomycin-resistant enterococci in South Africa: Implications for public health. South Afr. J. Sci. 114, 1–7. https://doi.org/10.17159/sajs.2018/4508

Frick, D.N., Banik, S., Rypma, R.S., 2007. Role of divalent metal cations in ATP hydrolysis catalyzed by the hepatitis C virus NS3 helicase: magnesium provides a bridge for ATP to fuel unwinding. J. Mol. Biol. 365, 1017–1032. https://doi.org/10.1016/j.jmb.2006.10.023

Friel, C.T., Bagshaw, C.R., Howard, J., 2011. Analysing the ATP turnover cycle of microtubule motors. Methods Mol. Biol. Clifton NJ 777, 177–192. https://doi.org/10.1007/978-1-61779-252-6_13

Friesner, R.A., Banks, J.L., Murphy, R.B., Halgren, T.A., Klicic, J.J., Mainz, D.T., Repasky, M.P., Knoll, E.H., Shelley, M., Perry, J.K., Shaw, D.E., Francis, P., Shenkin, P.S., 2004. Glide: a new approach for rapid, accurate docking and scoring. 1. Method and assessment of docking accuracy. J Med Chem 47, 1739–49. https://doi.org/10.1021/jm0306430

Gaberc-Porekar, V., Menart, V., 2001. Perspectives of immobilized-metal affinity chromatography. J. Biochem. Biophys. Methods 49, 335–360. https://doi.org/10.1016/s0165-022x(01)00207-x

Gasymov, O.K., Glasgow, B.J., 2007. ANS Fluorescence: Potential to Augment the Identification of the External Binding Sites of Proteins. Biochim. Biophys. Acta 1774, 403–411. https://doi.org/10.1016/j.bbapap.2007.01.002

Gay, G., Wagner, D.T., Keatinge-Clay, A.T., Gay, D.C., 2014. Rapid modification of the pET-28 expression vector for ligation independent cloning using homologous recombination in Saccharomyces cerevisiae. Plasmid 76, 66–71. https://doi.org/10.1016/j.plasmid.2014.09.005

Gniadkowski, M., 2008. Evolution of extended-spectrum beta-lactamases by mutation. Clin. Microbiol. Infect. Off. Publ. Eur. Soc. Clin. Microbiol. Infect. Dis. 14 Suppl 1, 11–32. https://doi.org/10.1111/j.1469-0691.2007.01854.x

Greenfield, N.J., 2006. Using circular dichroism spectra to estimate protein secondary structure. Nat Protoc 1, 2876–90. https://doi.org/10.1038/nprot.2006.202 10.1038/nprot.2006.202.

Hall, C.W., Mah, T.-F., 2017. Molecular mechanisms of biofilm-based antibiotic resistance and tolerance in pathogenic bacteria. FEMS Microbiol. Rev. 41, 276–301. https://doi.org/10.1093/femsre/fux010

Han, S., Forman, M.D., Loulakis, P., Rosner, M.H., Xie, Z., Wang, H., Danley, D.E., Yuan, W., Schafer, J., Xu, Z., 2006. Crystal Structure of Nicotinic Acid Mononucleotide Adenylyltransferase from Staphyloccocus aureus: Structural Basis for NaAD Interaction in Functional Dimer. J. Mol. Biol. 360, 814–825. https://doi.org/10.1016/j.jmb.2006.05.055

Hidron, A.I., Edwards, J.R., Patel, J., Horan, T.C., Sievert, D.M., Pollock, D.A., Fridkin, S.K., National Healthcare Safety Network Team, Participating National Healthcare Safety Network Facilities, 2008. NHSN annual update: antimicrobial-resistant pathogens associated with healthcare-associated infections: annual summary of data reported to the National Healthcare Safety Network at the Centers for Disease Control and Prevention, 2006-2007. Infect. Control Hosp. Epidemiol. 29, 996–1011. https://doi.org/10.1086/591861

Huang, N., Kolhatkar, R., Eyobo, Y., Sorci, L., Rodionova, I., Osterman, A.L., Mackerell, A.D., Zhang, H., 2010. Complexes of bacterial nicotinate mononucleotide adenylyltransferase with inhibitors: implication for structure-based drug design and improvement. J. Med. Chem. 53, 5229–5239. https://doi.org/10.1021/jm100377f

Hunter, J.D., 2012. Ventilator associated pneumonia. BMJ 344, e3325. https://doi.org/10.1136/bmj.e3325

Jeje, O., Maake, R., van Deventer, R., Esau, V., Iwuchukwu, E.A., Meyer, V., Khoza, T., Achilonu, I., 2022. Effect of Divalent Metal Ion on the Structure, Stability and Function of Klebsiella pneumoniae Nicotinate-Nucleotide Adenylyltransferase: Empirical and Computational Studies. Int. J. Mol. Sci. 23, 116. https://doi.org/10.3390/ijms23010116

Johnson, K.A., 1998. Advances in transient-state kinetics. Curr. Opin. Biotechnol. 9, 87–89. https://doi.org/10.1016/s0958-1669(98)80089-x

Khan, H.A., Baig, F.K., Mehboob, R., 2017. Nosocomial infections: Epidemiology, prevention, control and surveillance. Asian Pac. J. Trop. Biomed. 7, 478–482. https://doi.org/10.1016/j.apjtb.2017.01.019

Kim, D.E., Chivian, D., Baker, D., 2004. Protein structure prediction and analysis using the Robetta server. Nucleic Acids Res. 32, W526–W531. https://doi.org/10.1093/nar/gkh468

Kosower, E.M., Huppert, D., 1986. Excited State Electron and Proton Transfers. Annu. Rev. Phys. Chem. 37, 127–156. https://doi.org/10.1146/annurev.pc.37.100186.001015
Kosower, E.M., Kanety, H., 1983. Intramolecular donor-acceptor systems. 10. Multiple fluorescences from 8-(N-phenylamino)-1-naphthalenesulfonates. J. Am. Chem. Soc. 105, 6236–6243. https://doi.org/10.1021/ja00358a008
Lau, C., Niere, M., Ziegler, M., 2009. The NMN/NaMN adenylyltransferase (NMNAT) protein family. Front. Biosci. Landmark Ed. 14, 410–431. https://doi.org/10.2741/3252
Magiorakos, A.-P., Srinivasan, A., Carey, R.B., Carmeli, Y., Falagas, M.E., Giske, C.G., Harbarth, S., Hindler, J.F., Kahlmeter, G., Olsson-Liljequist, B., Paterson, D.L., Rice, L.B., Stelling, J., Struelens, M.J., Vatopoulos, A., Weber, J.T., Monnet, D.L., 2012. Multidrug-resistant, extensively drug-resistant and pandrug-resistant bacteria: an international expert proposal for interim standard definitions for acquired resistance. Clin. Microbiol. Infect. Off. Publ. Eur. Soc. Clin. Microbiol. Infect. Dis. 18, 268–281. https://doi.org/10.1111/j.1469-0691.2011.03570.x
Magni, G., Amici, A., Emanuelli, M., Orsomando, G., Raffaelli, N., Ruggieri, S., 2004. Structure and function of nicotinamide mononucleotide adenylyltransferase. Curr. Med. Chem. 11, 873–885. https://doi.org/10.2174/0929867043455666
Masi, M., Winterhalter, M., Pagès, J.-M., 2019. Outer Membrane Porins. Subcell. Biochem. 92, 79–123. https://doi.org/10.1007/978-3-030-18768-2_4
McArthur, A.G., Waglechner, N., Nizam, F., Yan, A., Azad, M.A., Baylay, A.J., Bhullar, K., Canova, M.J., De Pascale, G., Ejim, L., Kalan, L., King, A.M., Koteva, K., Morar, M., Mulvey, M.R., O'Brien, J.S., Pawlowski, A.C., Piddock, L.J.V., Spanogiannopoulos, P., Sutherland, A.D., Tang, I., Taylor, P.L., Thaker, M., Wang, W., Yan, M., Yu, T., Wright, G.D., 2013. The comprehensive antibiotic resistance database. Antimicrob. Agents Chemother. 57, 3348–3357. https://doi.org/10.1128/AAC.00419-13
McLean, L., 2015. 49 - Drug development, in: Hochberg, M.C., Silman, A.J., Smolen, J.S., Weinblatt, M.E., Weisman, M.H. (Eds.), Rheumatology (Sixth Edition). Mosby, Philadelphia, pp. 395–400. https://doi.org/10.1016/B978-0-323-09138-1.00049-8
Miles, A.J., Ramalli, S.G., Wallace, B.A., 2022. DichroWeb, a website for calculating protein secondary structure from circular dichroism spectroscopic data. Protein Sci. Publ. Protein Soc. 31, 37–46. https://doi.org/10.1002/pro.4153
Natalini, P., Ruggieri, S., Raffaelli, N., Magni, G., 1986. Nicotinamide mononucleotide adenylyltransferase. Molecular and enzymatic properties of the homogeneous enzyme from baker's yeast. Biochemistry 25, 3725–3729. https://doi.org/10.1021/bi00360a037
Ni, Q., Shaffer, J., Adams, J.A., 2000. Insights into nucleotide binding in protein kinase A using fluorescent adenosine derivatives. Protein Sci. Publ. Protein Soc. 9, 1818–1827.
Nirwati, H., Sinanjung, K., Fahrunissa, F., Wijaya, F., Napitupulu, S., Hati, V.P., Hakim, M.S., Meliala, A., Aman, A.T., Nuryastuti, T., 2019. Biofilm formation and antibiotic resistance of Klebsiella pneumoniae isolated from clinical samples in a tertiary care hospital, Klaten, Indonesia. BMC Proc. 13. https://doi.org/10.1186/s12919-019-0176-7
Olland, A.M., Underwood, K.W., Czerwinski, R.M., Lo, M.-C., Aulabaugh, A., Bard, J., Stahl, M.L., Somers, W.S., Sullivan, F.X., Chopra, R., 2002. Identification, characterization, and crystal structure of Bacillus subtilis nicotinic acid mononucleotide adenylyltransferase. J. Biol. Chem. 277, 3698–3707. https://doi.org/10.1074/jbc.M109670200
Owens, C.D., Stoessel, K., 2008. Surgical site infections: epidemiology, microbiology and prevention. J. Hosp. Infect. 70 Suppl 2, 3–10. https://doi.org/10.1016/S0195-6701(08)60017-1
Patel, J.T., Belsham, H.R., Rathbone, A.J., Friel, C.T., 2014. Use of stopped-flow fluorescence and labeled nucleotides to analyze the ATP turnover cycle of kinesins. J. Vis. Exp. JoVE e52142. https://doi.org/10.3791/52142
Petit, M.-A., Ehrlich, S.D., 2000. The NAD-dependent ligase encoded by yerG is an essential gene of Bacillus subtilis. Nucleic Acids Res. 28, 4642–4648.
Podschun, R., Ullmann, U., 1998. Klebsiella spp. as nosocomial pathogens: epidemiology, taxonomy, typing methods, and pathogenicity factors. Clin. Microbiol. Rev. 11, 589–603. https://doi.org/10.1128/CMR.11.4.589
Porath, J., Carlsson, J., Olsson, I., Belfrage, G., 1975. Metal chelate affinity chromatography, a new approach to protein fractionation. Nature 258, 598–599. https://doi.org/10.1038/258598a0
Qin, X., Galloway-Peña, J.R., Sillanpaa, J., Roh, J.H., Nallapareddy, S.R., Chowdhury, S., Bourgogne, A., Choudhury, T., Muzny, D.M., Buhay, C.J., Ding, Y., Dugan-Rocha, S., Liu, W., Kovar, C., Sodergren, E., Highlander, S., Petrosino, J.F., Worley, K.C., Gibbs, R.A., Weinstock, G.M., Murray, B.E., 2012. Complete genome sequence of Enterococcus faecium strain TX16 and comparative genomic analysis of Enterococcus faecium genomes. BMC Microbiol. 12, 135. https://doi.org/10.1186/1471-2180-12-135

Saridakis, V., Christendat, D., Kimber, M.S., Dharamsi, A., Edwards, A.M., Pai, E.F., 2001. Insights into ligand binding and catalysis of a central step in NAD+ synthesis: structures of Methanobacterium thermoautotrophicum NMN adenylyltransferase complexes. J. Biol. Chem. 276, 7225–7232. https://doi.org/10.1074/jbc.M008810200
Saridakis, V., Pai, E.F., 2003. Mutational, structural, and kinetic studies of the ATP-binding site of Methanobacterium thermoautotrophicum nicotinamide mononucleotide adenylyltransferase. J. Biol. Chem. 278, 34356–34363. https://doi.org/10.1074/jbc.M205369200
Saylor, P., Wang, C., Hirai, T.J., Adams, J.A., 1998. A Second Magnesium Ion Is Critical for ATP Binding in the Kinase Domain of the Oncoprotein v-Fps. Biochemistry 37, 12624–12630. https://doi.org/10.1021/bi9812672
Schembri, M.A., Hjerrild, L., Gjermansen, M., Klemm, P., 2003. Differential expression of the Escherichia coli autoaggregation factor antigen 43. J. Bacteriol. 185, 2236–2242. https://doi.org/10.1128/jb.185.7.2236-2242.2003
Secor, P.R., Michaels, L.A., Ratjen, A., Jennings, L.K., Singh, P.K., 2018. Entropically driven aggregation of bacteria by host polymers promotes antibiotic tolerance in Pseudomonas aeruginosa. Proc. Natl. Acad. Sci. U. S. A. 115, 10780–10785. https://doi.org/10.1073/pnas.1806005115
Secor, P.R., Sweere, J.M., Michaels, L.A., Malkovskiy, A.V., Lazzareschi, D., Katznelson, E., Rajadas, J., Birnbaum, M.E., Arrigoni, A., Braun, K.R., Evanko, S.P., Stevens, D.A., Kaminsky, W., Singh, P.K., Parks, W.C., Bollyky, P.L., 2015. Filamentous Bacteriophage Promote Biofilm Assembly and Function. Cell Host Microbe 18, 549–559. https://doi.org/10.1016/j.chom.2015.10.013
Semisotnov, G.V., Rodionova, N.A., Razgulyaev, O.I., Uversky, V.N., Gripas', A.F., Gilmanshin, R.I., 1991. Study of the "molten globule" intermediate state in protein folding by a hydrophobic fluorescent probe. Biopolymers 31, 119–128. https://doi.org/10.1002/bip.360310111
Sershon, V.C., Santarsiero, B.D., Mesecar, A., 2009. Kinetic and X-Ray Structural Evidence for Negative Cooperativity in Substrate Binding to Nicotinate Mononucleotide Adenylyltransferase (NMAT) from Bacillus anthracis. J. Mol. Biol. 385, 867–888. https://doi.org/10.1016/j.jmb.2008.10.037
Shaw, K.J., Rather, P.N., Hare, R.S., Miller, G.H., 1993. Molecular genetics of aminoglycoside resistance genes and familial relationships of the aminoglycoside-modifying enzymes. Microbiol. Rev. 57, 138–163.
Slavík, J., 1982. Anilinonaphthalene sulfonate as a probe of membrane composition and function. Biochim. Biophys. Acta 694, 1–25. https://doi.org/10.1016/0304-4157(82)90012-0
Sommer, M.O.A., Munck, C., Toft-Kehler, R.V., Andersson, D.I., 2017. Prediction of antibiotic resistance: time for a new preclinical paradigm? Nat. Rev. Microbiol. 15, 689–696. https://doi.org/10.1038/nrmicro.2017.75
Sorci, L., Cimadamore, F., Scotti, S., Petrelli, R., Cappellacci, L., Franchetti, P., Orsomando, G., Magni, G., 2007. Initial-rate kinetics of human NMN-adenylyltransferases: substrate and metal ion specificity, inhibition by products and multisubstrate analogues, and isozyme contributions to NAD+ biosynthesis. Biochemistry 46, 4912–4922. https://doi.org/10.1021/bi6023379
Studier, F.W., Moffatt, B.A., 1986. Use of bacteriophage T7 RNA polymerase to direct selective high-level expression of cloned genes. J. Mol. Biol. 189, 113–130. https://doi.org/10.1016/0022-2836(86)90385-2
Tabor, S., 2001. Expression using the T7 RNA polymerase/promoter system. Curr. Protoc. Mol. Biol. Chapter 16, Unit16.2. https://doi.org/10.1002/0471142727.mb1602s11
Twyman, R.M., Stoger, E., Schillberg, S., Christou, P., Fischer, R., 2003. Molecular farming in plants: host systems and expression technology. Trends Biotechnol. 21, 570–578. https://doi.org/10.1016/j.tibtech.2003.10.002
Waterhouse, A., Bertoni, M., Bienert, S., Studer, G., Tauriello, G., Gumienny, R., Heer, F.T., de Beer, T.A.P., Rempfer, C., Bordoli, L., Lepore, R., Schwede, T., 2018. SWISS-MODEL: homology modelling of protein structures and complexes. Nucleic Acids Res. 46, W296–W303. https://doi.org/10.1093/nar/gky427
Whitmore, L., Wallace, B.A., 2008. Protein secondary structure analyses from circular dichroism spectroscopy: methods and reference databases. Biopolymers 89, 392–400. https://doi.org/10.1002/bip.20853
Whitmore, L., Wallace, B.A., 2004. DICHROWEB, an online server for protein secondary structure analyses from circular dichroism spectroscopic data. Nucleic Acids Res. 32, W668-673. https://doi.org/10.1093/nar/gkh371
Williams, N.H., 2000. Magnesium Ion Catalyzed ATP Hydrolysis. J. Am. Chem. Soc. 122, 12023–12024. https://doi.org/10.1021/ja0013374
Woody, R.W., 1995. [4] Circular dichroism, in: Methods in Enzymology, Biochemical Spectroscopy. Academic Press, pp. 34–71. https://doi.org/10.1016/0076-6879(95)46006-3
Yamanaka, R., Tabata, S., Shindo, Y., Hotta, K., Suzuki, K., Soga, T., Oka, K., 2016. Mitochondrial Mg2+ homeostasis decides cellular energy metabolism and vulnerability to stress. Sci. Rep. 6, 30027. https://doi.org/10.1038/srep30027

Yoon, H.-J., Kim, H.L., Mikami, B., Suh, S.W., 2005. Crystal structure of nicotinic acid mononucleotide adenylyltransferase from Pseudomonas aeruginosa in its Apo and substrate-complexed forms reveals a fully open conformation. J. Mol. Biol. 351, 258–265. https://doi.org/10.1016/j.jmb.2005.06.001

Yoshino, J., Imai, S.-I., 2013. Accurate measurement of nicotinamide adenine dinucleotide (NAD^+) with high-performance liquid chromatography. Methods Mol. Biol. Clifton NJ 1077, 203–215. https://doi.org/10.1007/978-1-62703-637-5_14

Zapun, A., Contreras-Martel, C., Vernet, T., 2008. Penicillin-binding proteins and beta-lactam resistance. FEMS Microbiol. Rev. 32, 361–385. https://doi.org/10.1111/j.1574-6976.2007.00095.x

Zar, H.J., MacGinty, R., Workman, L., Burd, T., Smith, G., Myer, L., Häggström, J., Nicol, M.P., 2022. Klebsiella pneumoniae Lower Respiratory Tract Infection in a South African Birth Cohort: a Longitudinal Study. Int. J. Infect. Dis. 121, 31–38. https://doi.org/10.1016/j.ijid.2022.04.043

Zhai, R.G., Rizzi, M., Garavaglia, S., 2009. Nicotinamide/nicotinic acid mononucleotide adenylyltransferase, new insights into an ancient enzyme. Cell. Mol. Life Sci. CMLS 66, 2805–2818. https://doi.org/10.1007/s00018-009-0047-x

Zhang, H., Zhou, T., Kurnasov, O., Cheek, S., Grishin, N.V., Osterman, A., 2002. Crystal structures of E. coli nicotinate mononucleotide adenylyltransferase and its complex with deamido-NAD. Struct. Lond. Engl. 1993 10, 69–79. https://doi.org/10.1016/s0969-2126(01)00693-1

Zhang, X., Kurnasov, O.V., Karthikeyan, S., Grishin, N.V., Osterman, A.L., Zhang, H., 2003. Structural characterization of a human cytosolic NMN/NaMN adenylyltransferase and implication in human NAD biosynthesis. J. Biol. Chem. 278, 13503–13511. https://doi.org/10.1074/jbc.M300073200

Ziegler, M., 2000. New functions of a long-known molecule. Emerging roles of NAD in cellular signaling. Eur. J. Biochem. 267, 1550–1564. https://doi.org/10.1046/j.1432-1327.2000.01187.x

Ziegler, M., Oei, S.L., 2001. A cellular survival switch: poly(ADP-ribosyl)ation stimulates DNA repair and silences transcription. BioEssays News Rev. Mol. Cell. Dev. Biol. 23, 543–548. https://doi.org/10.1002/bies.1074